Capillary-driven Interactions at Solid and Liquid Interfaces: Adhesion, Bridging, and Removal

Ke Sun

Capillary-driven Interactions at Solid and Liquid Interfaces: Adhesion, Bridging, and Removal

Ke Sun

A thesis presented for the degree of Doctor of Philosophy

Department of Physics
Durham University
United Kingdom, August, 2025

Declaration

The work in this thesis is based on research carried out at the Department of Physics, Durham University, United Kingdom. No part of this thesis has been submitted elsewhere for any other degree or qualification and it is all my own work unless referenced to the contrary in the text.

- Chapter 4 is a joint work with Sarah J. Goodband, in which Sarah performed the experiments and I carried out the simulations.
- Figure 6.2 is a joint work with Marlene Hill; we conducted the experiments together.

Abstract

Capillarity governs how fluids interact with interfaces, linking fundamental physics with engineering applications. Although the thermodynamics based on surface tension and Laplace pressure are well established, how these interactions evolve across scales and physical environments remains incompletely understood. In this thesis, I investigate three core aspects of interfacial capillarity: particle adhesion, liquid bridging, and capillary-driven droplet removal, aiming to develop a unified framework that connects microscopic interactions to macroscopic function through integrated experiments and quasi-static modelling.

Starting from the nanoscale, particle adhesion at liquid interfaces is quantified using atomic force microscopy and modelling. The results show that classical thermodynamics remains valid, with adhesion governed by geometry and wettability, while line tension becomes significant below a characteristic length threshold. This insight supports the design of functional nanoparticles that either resist or promote interfacial adsorption. At millimetre scales, I examine capillary bridges across hydrophilic, hydrophobic, and liquid-infused surfaces. Distinct contact line dynamics are revealed, from pinning and hysteresis on solid surfaces to near-frictionless motion on liquid-infused surfaces, yet all systems can be consistently described by interfacial tension and Laplace pressure. On liquid-infused surfaces, enhanced mobility enables lubricant transfer and amplifies gravity-induced geometric asymmetry, providing design strategies for controlled capillary–substrate interactions.

Building on these insights, I introduce a capillary-lifting mechanism for efficient droplet removal. By harnessing high interfacial tension as the driving force for detachment, this approach eliminates the need for surfactants and reduces water consumption. Predictive detachment criteria based on apparent and receding contact angles are validated through agreement between experiments, simulations, and theory. The method is further demonstrated using real-world contaminants and low-additive formulations, highlighting its potential for sustainable cleaning.

Together, this thesis establishes a predictive and experimentally validated framework for capillary behaviour from nanometre to millimetre scales, advancing our understanding of how interfacial geometry and chemistry govern capillary forces and liquid morphology. More importantly, this work demonstrates how subtle yet powerful interfacial capillarity can be harnessed to control solid–liquid interactions, direct droplet motion, and achieve efficient liquid removal, opening new opportunities in liquid manipulation, functional materials, and sustainable surface technologies.

Acknowledgements

My sincere thanks go to my supervisors, Prof. Halim Kusumaatmaja and Prof. Kislon Voïtchovsky, for their generous support, guidance, and for being inspirational role models beyond research.

I would like to thank Dr. Yonas Gizaw for his valuable industrial insight. I am also grateful to the experimental and simulation research groups, in particular Dr. Sarah Goodband and Dr. Jack Panter for their training, and Alex Brown, Dr. Alvin Shek, and Dr. Abhinav Naga for their help and thoughtful suggestions.

This Ph.D. is funded by the EPSRC Centre for Doctoral Training in Soft Matter for Formulation and Industrial Innovation. I appreciate all the support and training opportunities that broadened my perspective in soft matter and beyond.

Finally, I thank my family for their unwavering support and unconditional love.

Research outputs

Chapter 3 is formed mainly by the following work:

- Sun, K., Gizaw, Y., Kusumaatmaja, H. & Voïtchovsky, K., Nanoparticle adhesion at Liquid Interfaces, *Soft Matter* **21**, 585–595 (2025).

Chapter 4 is formed mainly by the following joint work with Sarah Goodband:

- Goodband, S. J.[*], Sun, K.[*], Voïtchovsky, K., & Kusumaatmaja, H., Stretching and Compressing Capillary Bridges on Hydrophilic, Hydrophobic, and Liquid-infused Surfaces, under review.
  [*]Joint first authors.

Chapter 5 is formed mainly by the following work:

- Sun, K., Panter, J. R., Shek, A. C. M., Gizaw, Y., Voïtchovsky, K., & Kusumaatmaja, H., Droplet Removal by Capillary Lifting, under review.

Contents

Chapter 1

Introduction

1.1 Capillarity in nature and engineering

Capillarity is a subtle and ubiquitous phenomenon that shapes our everyday world. We see it when water climbs up a narrow tube, when plants draw water from their roots to their leaves, and when children build sandcastles on the beach. Capillarity occurs when a liquid meets another fluid or a solid surface, creating an interface between the two phases. At this interface, the imbalance of molecular forces gives rise to strong effects, producing curved menisci, pressure differences, and adhesion. These capillary interactions can drive fluid motion, stabilise interface shapes, and connect solids, particles, and droplets. Although studied for centuries, capillary phenomena remain a cornerstone of both physics and engineering, playing an important role in functional materials, colloid science, wetting, microfluidics, and broader soft matter research.

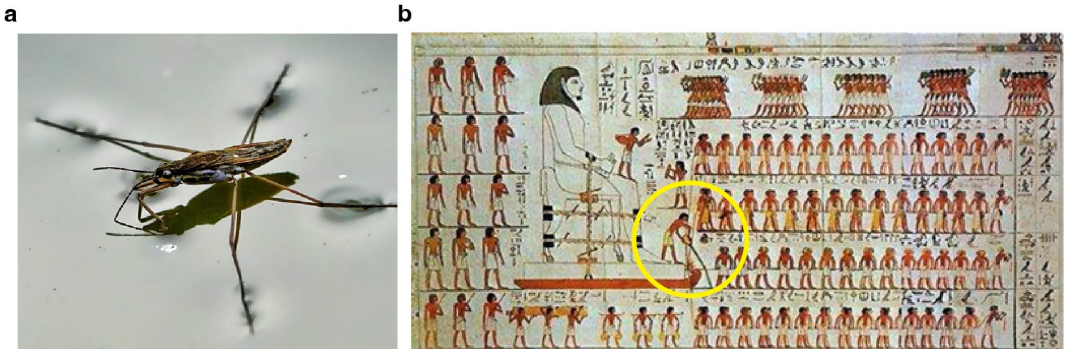

Figure 1.1: **(a)** Photograph of a water strider by Sabine [1], sourced from Pixabay and used under the Pixabay Content License. **(b)** Egyptian wall painting from 1880 B.C. on the tomb of Djehutihotep. The added yellow circle highlights the figure standing at the front of the sled and pouring water onto the sand. [2, 3]

Capillarity influences a wide range of natural and engineered systems, bridging nature and human innovation since ancient times. In nature, water walking insects such as water striders use meniscus deformation beneath their legs to generate suf-

ficient upward force needed to stay afloat (Fig. 1.1a). [4] Capillary condensation in porous materials controls how liquids are stored within microscopic pores and interstitial spaces. [5, 6] In engineering, ancient Egyptians are thought to have exploited capillary bridging to transport heavy stones: adding small amounts of water to desert sand creates liquid bridges between grains, enhancing cohesion and reducing the sand's shear modulus (Fig. 1.1b). This simple technique lowered the force required to drag sledges carrying massive stone blocks. [2] These examples illustrate the universality of capillary interactions, which operate across many length scales, from microscopic bridging to macroscopic flows, and across disciplines ranging from biology to physics and engineering.

Inspired by such phenomena, modern technologies increasingly harness capillary forces for practical use. Examples include the directed self-assembly of colloidal particles [7], capillary-assisted fabrication and surface patterning [8, 9], wettability control for enhanced oil recovery [10], microfluidic transport systems [11], and high precision inkjet printing [12]. Across these applications, the underlying physics remains the same, with surface tension and interfacial curvature combining to generate forces that mediate adhesion, bridging, and detachment.

The main challenge in controlling capillary phenomena lies in understanding how wettability, curvature, viscosity, and dynamic conditions interact to produce specific outcomes. These include inducing controlled motion, guiding morphological transitions, and programming self-assembly pathways. This thesis explores these questions by examining how capillary bridge geometry and its evolution can be manipulated through material and environmental parameters to achieve predictable, programmable responses across multiple scales.

1.2 Research motivation

Interfacial phenomena determine how liquids adhere, spread, and detach from surfaces, influencing processes ranging from coating and printing to oil recovery and drug delivery. Despite centuries of study, our ability to predict and utilise capillary effects across scales and at complex interfaces remains limited. This thesis seeks to

advance the understanding of capillary interactions at solid and liquid interfaces, bridging fundamental physics with practical applications. The present section outlines the broader motivation and societal relevance of this work, while the detailed scientific background and literature review are presented in Section 1.4.

Capillary forces lie at the heart of adhesion, cohesion, and liquid transport. When a particle or droplet meets a fluid interface, it creates a strong attachment that can stabilise emulsions or guide the assembly of materials. Classical models describe these effects well at the micro- to millimetre-scale, but their validity at the nanoscale remains uncertain. With the rapid development of nanomaterials and nanoengineering, understanding these interactions is essential for designing functional materials, controlling particle stability in emulsions, and improving the performance of nanoscale drug carriers and diagnostic particles operating at complex biological interfaces. A systematic understanding of the parameters governing nanoscale capillary adhesion could ultimately enable the design of nanoparticles with controllable attachment and release behaviours.

Beyond individual particles, capillary bridges between surfaces are central to many applications, from wet granular materials and coating processes to printing, lubrication, and biomedical devices. Liquid transport plays a vital role in these systems and depends sensitively on geometry, wettability, and the surrounding environment. A major challenge in this field is to reduce friction and thereby minimise energy consumption. Recent advances in surface engineering, particularly superhydrophobic materials such as liquid-infused surfaces (see Section 2.2 for details), have opened new ways to manipulate interfacial motion, enabling nearly frictionless droplet movement and self-cleaning features. However, the presence of a lubricant layer or surface microstructure adds complexity to how capillary bridges form, deform, and rupture. Understanding these effects is not only fundamental to the physics of capillary cohesion but also essential for designing functional surfaces that control liquid transport, adhesion, and responsiveness in advanced technologies.

Finally, this thesis is driven by the broader goal of addressing real-world challenges through the use of capillary effects. One emerging direction explored here is the use of capillarity to lift off contaminants and enable efficient surface cleaning.

Surface cleaning is critical in manufacturing and maintenance and relies heavily on water, energy, and surfactants, creating growing resource and environmental pressures. Global water scarcity costs the economy over 300 billion USD each year. Whereas in manufacturing sectors such as electronics and food, cleaning operations consume more than 5 billion tonnes of water annually, along with roughly 9 million tonnes of surfactants that end up in aquatic environments as toxic and poorly biodegradable waste. [13–16] These challenges highlight the urgent need for sustainable cleaning technologies that drastically reduce water and chemical use. In this context, this thesis demonstrates how capillary interactions can be harnessed to achieve resource-efficient and surfactant-free cleaning through controlled interfacial lifting.

Taken together, this research builds a comprehensive understanding of capillarity across scales and interfaces. By combining nanoscale particle adhesion, macroscopic bridge mechanics, and capillary-driven droplet removal, it establishes experimental and modelling frameworks that connect fundamental interfacial physics with sustainable technological applications. In doing so, this thesis contributes to the broader goals of developing highly efficient and sustainable materials and technologies, in alignment with the United Nations Sustainable Development Goals [17].

1.3 Physics of surfaces and interfaces

1.3.1 Surface and interfacial tension

An interface is the boundary between two phases that are in contact, such as solid–liquid, liquid–gas, or liquid–liquid systems. On the molecular scale, interfaces are inherently complex, as their properties depend on the specific interactions between molecules and on Brownian motion. At the macroscopic level, however, an interface is often treated as an ideal surface of zero thickness, whose behaviour can be characterised by its wetting properties.

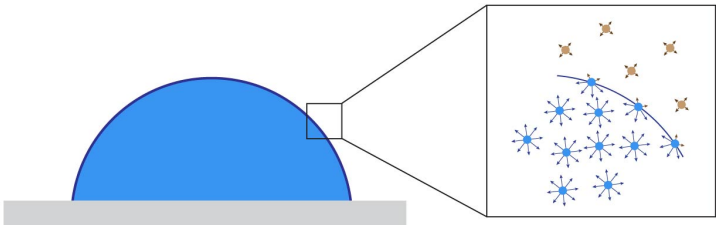

Figure 1.2: Macroscopic view of a liquid droplet deposited on a solid substrate, with an inset showing the microscopic molecular interactions at the liquid–air interface. Blue spheres represent liquid molecules and yellow spheres represent gas molecules. Arrows indicate intermolecular interactions, highlighting that the liquid molecules at the interface experience asymmetric interactions between the bulk liquid and the gas phase.

Microscopic origin

To illustrate the origin of surface tension, consider a liquid–air interface as shown in Fig. 1.2. Molecules in the bulk of a liquid interact symmetrically with neighbours in all directions. For organic liquids, these cohesive interactions are mainly van der Waals forces, while in polar liquids they also include hydrogen bonding. At the interface, molecules experience an anisotropic environment: half of their neighbours are liquid molecules, while the other half are gas-phase molecules. This imbalance creates a local asymmetry, giving rise to an excess free energy at the interface. In molecular terms, surface tension can be interpreted as the work required to bring a molecule from the bulk to the interface, thereby breaking cohesive interactions. A simple scaling estimate can be written as:

$$\gamma \sim \frac{U/2}{\varsigma^2}, \tag{1.1}$$

where U is the total cohesive energy per molecule, $U/2$ is an approximate excess energy for an interfacial molecule, and ς^2 represents the molecular cross-sectional area. Typical values of surface tension are approximately 70 $\mathrm{mN\,m^{-1}}$ for water and 20–40 $\mathrm{mN\,m^{-1}}$ for organic liquids, reflecting the fact that liquids with weaker cohesive forces or larger molecular cross sections generally exhibit lower surface tension.

This description applies equally to interfaces involving solids. At a solid–liquid boundary, liquid molecules are attracted to the solid surface through van der Waals

interactions. In such cases, the term surface tension is often used when one phase is solid, while interfacial tension more generally refers to the boundary between two fluids.

Thermodynamic definition

So far we have considered the molecular origin of surface tension. At the macroscopic level, surface tension can also be defined thermodynamically as the excess free energy associated with an interface, with dimensions of energy per unit area (J m^{-2}) or equivalently force per unit length (N m^{-1}). For a system at constant temperature and pressure, the relevant potential is the Gibbs free energy, G. The surface tension γ is defined as the reversible work required to create a unit area of new interface, or equivalently, as the excess Gibbs free energy per unit area: [18]

$$\gamma = \left(\frac{\partial G}{\partial A}\right)_{T,\,p,\,n_i} \tag{1.2}$$

where A is the interfacial area and the subscripts (T, p, n_i) indicate the derivative is taken at constant temperature, pressure, and amounts of each chemical species i in the system. The surface energy associated with an interface of area A is therefore:

$$E = \gamma A \tag{1.3}$$

Since $\gamma > 0$, the surface energy contributes positively to the total free energy of the system. Consequently, interfaces tend to minimise their area at equilibrium, constrained by fixed volume, boundary conditions, or prescribed contact angles. This energy minimisation principle governs the equilibrium shapes of droplets, bubbles, menisci, and capillary bridges. This principle also provides the theoretical basis for surface energy calculations carried out using the software Surface Evolver [19] (see details in Section 2.5), the primary simulation method used in this thesis.

1.3.2 Wetting and contact angle

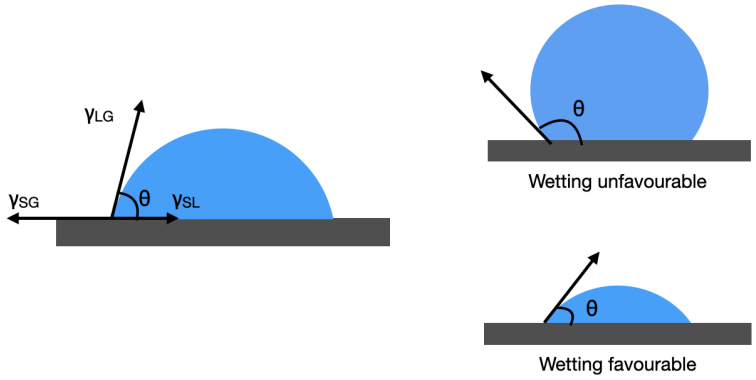

Figure 1.3: Static contact angle θ and surface wettability. γ_{SG}, γ_{LG}, γ_{SL} are the interfacial tensions of solid-gas, liquid-gas and solid-liquid, respectively.

The contact angle is defined geometrically as the angle formed at the junction of three phases, typically a liquid, a surrounding fluid such as air or another immiscible liquid, and a solid surface, as shown in Fig. 1.3. For simplicity, the surrounding phase is referred to as the gas phase throughout this section. Contact angle provides a direct measure of how well a liquid wets a surface. When the contact angle is less than 90°, wetting is favourable and the solid is termed hydrophilic (if the liquid is water) or oleophilic (if the liquid is oil). When the contact angle exceeds 90°, wetting is unfavourable and the surface is described as hydrophobic or oleophobic.

The theoretical description of the contact angle arises from the thermodynamic equilibrium of the three interfacial tensions. For an ideal surface that is perfectly smooth, flat, and chemically homogeneous, the balance of these tensions is expressed by Young's equation: [20]

$$\cos\theta = \frac{\gamma_{sg} - \gamma_{sl}}{\gamma_{lg}}, \tag{1.4}$$

where θ is the contact angle and γ_{sg}, γ_{sl}, and γ_{lg} are the solid–gas, solid–liquid, and liquid–gas surface tension, respectively.

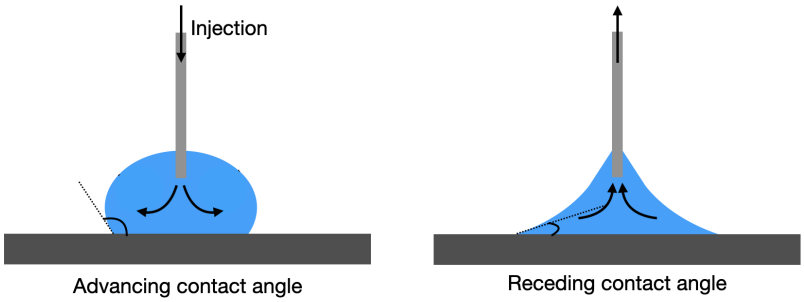

Figure 1.4: Advancing and receding contact angles.

In practice, however, surfaces are rarely ideal. Surface roughness, chemical heterogeneity, or surface contamination can cause the measured static contact angle of a sessile droplet (Fig. 1.3) to vary depending on how the droplet was formed. To account for this, advancing and receding contact angles are more often employed experimentally. These are measured when the three-phase contact line moves relative to the solid surface, as illustrated in Fig. 1.4. The advancing contact angle corresponds to the maximum angle observed as the droplet volume increases and the contact line advances, while the receding contact angle is the minimum angle observed as the volume decreases and the contact line recedes. The absolute difference between the advancing and receding angles is defined as the contact angle hysteresis. It quantifies the resistance of the contact line to motion during droplet movement or volume change, reflecting surface heterogeneity and pinning effects. Measuring these dynamic angles helps the system overcome local metastable energy states, making the results more reproducible. The contact angles measured under static or quasi-static conditions are well described by Young's equation. At higher contact line velocities, however, viscous and hydrodynamic effects become significant, and the contact angle depends on the speed of motion. In this regime, the behaviour is instead described by the Voinov relation, which links the apparent contact angle to the capillary number of the moving fluid. [21]

Here we list some representative contact angles for water and oil on common and functionalised surfaces. On hydrophilic glass, water droplets typically exhibit contact angles of 20°–40°, depending on surface preparation. [22, 23] The contact angle hysteresis is usually 10°–20°. [24] On hydrophobic surfaces such as silane-treated

glass, the water contact angle increases to 70°–150°, with hysteresis typically around 20°. [25] On superhydrophobic surfaces, contact angles can exceed 150°, although hysteresis varies widely from less than 3° on lubricant-impregnated structures to more than 30° on microstructured substrates. [26, 27] Oil droplets, by contrast, spread readily on glass surfaces in air, with the measured instantaneous contact angle decreasing over time. [28] These examples illustrate how surface chemistry and roughness strongly influence both static contact angles and dynamic hysteresis. In Chapter 4 of this thesis, we studied liquid-infused surfaces (LIS, introduced in detail in Section 2.2), which are designed to minimise hysteresis to below 3°, enabling frictionless motion and highly reproducible wetting behaviour. [27]

1.3.3 Laplace pressure

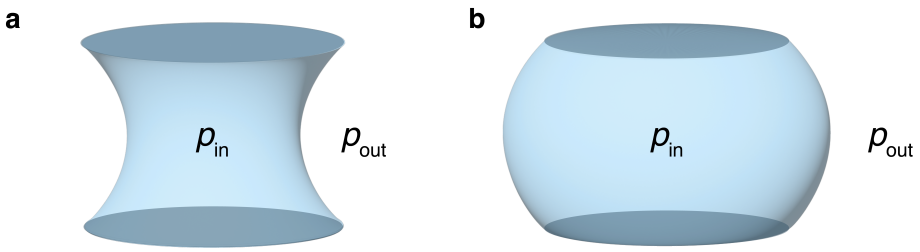

Figure 1.5: Schematic illustrations of **(a)** a concave capillary bridge and **(b)** a convex capillary bridge, showing the internal pressure p_{in} and the external pressure p_{out}.

Surface tension acts at liquid surfaces and interfaces to minimise the interfacial area, often causing the interface to curve. This curvature produces a pressure difference across the boundary between two phases, known as the Laplace pressure. Laplace pressure is fundamental to understanding the behaviour and mechanical stability of droplets, bubbles, foams, emulsions, and capillary bridges, as it determines their equilibrium shape and deformation. The relationship between interfacial curvature and pressure difference is described by the Young–Laplace equation: [20]

$$\Delta p = \gamma \left(\frac{1}{R_1} + \frac{1}{R_2} \right) \tag{1.5}$$

where γ is the surface tension, and R_1 and R_2 are the principal radii of curvature at any point on the surface. The mean curvature is defined as $\kappa = 1/R_1 + 1/R_2$. The

radius of curvature is considered positive when its centre lies within the liquid phase and negative otherwise. Here we use $\Delta p = p_{in} - p_{out}$ which is used in later force calculations in Eqs. 1.11 and 1.12, as well as in Chapter 4. Under this convention, a concave meniscus has $\Delta p < 0$, corresponding to $p_{in} < p_{out}$, whereas a convex interface has $\Delta p > 0$, corresponding to $p_{in} > p_{out}$, as shown in Fig. 1.5.

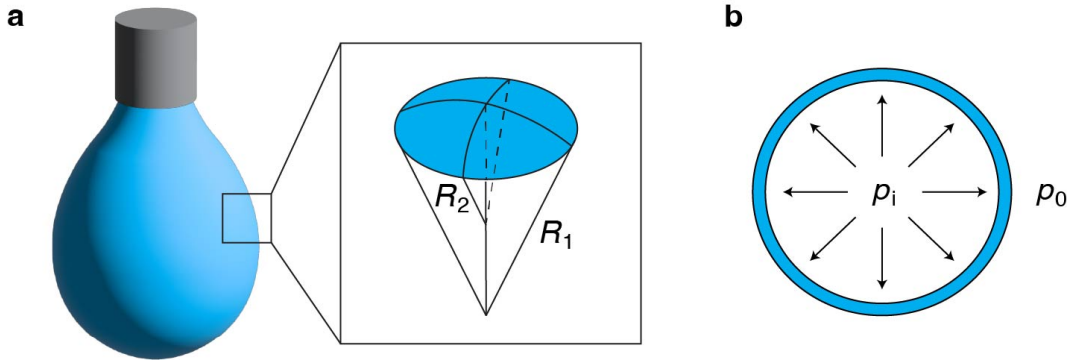

Figure 1.6: **(a)** Pendant drop suspended from a needle, showing axisymmetric curvature modified by gravity, with principal radii of curvature R_1 and R_2 indicated in the inset. **(b)** Soap bubble illustrating the pressure difference between the internal pressure p_i and the external pressure p_0.

A classic example of the Young–Laplace equation in practice is the pendant drop technique used to measure surface tension (Fig. 1.6a). In this method, a liquid droplet is dispensed from a needle and suspended under gravity. The droplet shape results from a balance between surface tension, which tends to minimise surface area (favouring a spherical shape), and gravity, which elongates the droplet downward. This competition gives rise to the characteristic pear profile of a pendant drop. The pressure within the droplet varies with height according to $p(z) = p_0 - \Delta\rho g z$, where $\Delta\rho$ is the density difference between the liquid and surrounding fluid, g is the gravitational acceleration, and z is the vertical coordinate. Because the Laplace pressure must balance this hydrostatic variation at every point along the interface, the local curvature κ changes continuously along the drop profile. By fitting the experimentally measured droplet contour to the Young–Laplace equation and including gravity, the surface tension γ can be determined.

Another familiar example is a bubble, where the excess internal pressure counteracts the inward pull of interfacial tension and prevents collapse. For a spherical gas bubble in a liquid, where $R_1 = R_2 = R$, the pressure difference is $p_i - p_0 = 2\gamma/R$.

For a soap bubble consisting of a thin liquid film separating two gas–liquid interfaces, both interfaces contribute to the total pressure difference, giving $p_i - p_0 = 4\gamma/R$ when the film thickness is negligible (Fig. 1.6b). These examples show how Laplace pressure governs the shape, stability, and mechanical balance of interfaces. It is a central concept in interfacial science and provides the physical foundation for capillary phenomena discussed later in this thesis.

1.3.4 Dimensionless numbers

Fluid interfaces often involve competition between physical forces such as surface tension, gravity, viscosity, and inertia. The relative importance of these forces can be characterised by several dimensionless numbers, which provide a quantitative basis for classifying flow regimes and interfacial behaviour. In this work, three key dimensionless numbers are used to define the parameter space in both experiments and simulations.

Capillary number

The capillary number (Ca) quantifies the ratio of viscous forces to surface tension forces acting across a fluid interface: [29]

$$\mathrm{Ca} = \frac{\mu\, V}{\gamma} \tag{1.6}$$

where μ is the dynamic viscosity of the liquid, V is a characteristic fluid velocity (*e.g.*, the speed of interface displacement), and γ is the interfacial tension. At low Ca, surface tension dominates and the interface remains close to its equilibrium shape. At high Ca, viscous stress can substantially deform the interface. In this thesis, the focus lies on the quasi-static regime, where interface motion is slow enough that viscous dissipation is negligible compared to changes in capillary energy. The experimental conditions correspond to $Ca < 10^{-7}$, well below the threshold (typically $Ca \approx 10^{-5}$ [30, 31]) at which dynamic effects become significant. Thus, the interface evolves through a series of equilibrium configurations governed by energy minimisation, and surface tension dominates over viscous forces.

Bond number

The Bond number (Bo), also known as the Eötvös number, compares gravitational forces to surface tension: [29]

$$\mathrm{Bo} = \frac{\Delta\rho\, g\, L^2}{\gamma} \tag{1.7}$$

where $\Delta\rho$ is the density difference between the two phases, g is the gravitational acceleration, L is a characteristic length scale (e.g., droplet radius or bridge height), and γ is the interfacial tension. When $Bo \ll 1$, surface tension dominates and gravity can be neglected, such as for microscopic spherical droplets or small capillary bridges. When $Bo \gtrsim 1$, deformation becomes significant, as seen in large sessile or pendant drops. To evaluate when gravity must be included in simulations, we also use the capillary length λ, which defines the characteristic scale at which gravitational and surface tension forces balance:

$$\lambda = \sqrt{\frac{\gamma}{\Delta\rho\, g}} \tag{1.8}$$

The Bond number can be related by $Bo = \left(\frac{L}{\lambda}\right)^2$. Taking water in air at room temperature as an example, the capillary length λ is approximately 2.7 mm. Thus, droplets or capillary structures smaller than this length are governed primarily by surface tension, while larger ones are influenced by gravity. The capillary length λ serves as a convenient reference for distinguishing between surface tension-dominated and gravity-impacted regimes.

Reynolds number

The Reynolds number (Re) characterises the ratio of inertial to viscous forces in fluid flow: [32]

$$\mathrm{Re} = \frac{\rho\, V\, L}{\mu} \tag{1.9}$$

where ρ is the fluid density, V is a characteristic velocity, L is a characteristic length, and μ is the dynamic viscosity. At $Re \ll 1$, viscous forces dominate and the flow is smooth and laminar, also known as Stokes flow. This is typical of small-scale systems, highly viscous fluids, or slow motions. At higher Reynolds numbers,

typically $Re \gtrsim 2000$ [33, 34], inertia becomes important and turbulence develops. In this thesis, the Reynolds number of our experimental systems is consistently very low ($Re \ll 1$), confirming that inertial effects are negligible. Together with the very low Ca, this places the system firmly in the quasi-static, capillary-dominated regime. The Bond number then serves as the primary variable determining when gravity must be considered in the mechanical balance of the interface. It should be noted that this thesis focuses on quasi-static capillary manipulation, whereas dynamic mechanisms lie outside the main research scope and are discussed only as broader background context.

Table 1.1: Representative parameters and resulting dimensionless numbers for the systems studied in this thesis: Chapter 3 (nanoparticle adhesion, Chapter 4 (capillary bridges), and Chapter 5 (capillary-driven droplet lifting).

Parameter	**Chapter 3**	**Chapter 4**	**Chapter 5**
L (m)	5.0×10^{-9}	1.2×10^{-3}	2.2×10^{-3}
V (m s^{-1})	1.0×10^{-7}	8.0×10^{-6}	5.3×10^{-7}
μ (Pa s)	9.4×10^{-3}	4.5×10^{-2}	1.0×10^{-3}
γ (N m^{-1})	2.0×10^{-2}	6.7×10^{-2}	4.2×10^{-2}
$\Delta\rho$ (kg m^{-3})	9.3×10^{2}	1.2×10^{3}	2.5×10^{2}
ρ (kg m^{-3})	9.3×10^{2}	1.2×10^{3}	1.0×10^{3}
Bo	1.1×10^{-11}	2.5×10^{-1}	2.7×10^{-1}
Ca	4.7×10^{-8}	5.4×10^{-6}	1.3×10^{-8}
Re	4.9×10^{-11}	2.5×10^{-4}	1.1×10^{-3}

Table 1.1 presents typical experimental systems studied in this thesis, together with representative physical properties and the resulting dimensionless numbers. The low values of Ca and Re indicate that viscous and inertial effects are negligible under the conditions considered, thereby justifying quasi-static modelling. The Bond number is negligible for Chapter 3 but not far from unity for Chapters 4 and 5, indicating that gravity in these millimetre-scale systems must be explicitly accounted for.

1.4 Capillary interactions at interfaces

Interfacial capillarity encompasses a wide range of physical phenomena, from the adhesion of particles and droplets at interfaces to the motion of droplets in mi-

crofluidic channels and the formation of liquid bridge networks in colloidal systems. These interactions govern processes as diverse as emulsion stability, granular cohesion, surface drying, and biological adhesion. Hereafter, we briefly review a few representative examples of capillary forces at interfaces where the geometry and force derivations are relevant to this thesis. These include particle adhesion at liquid interfaces and capillary bridging between flat or curved surfaces. For a more comprehensive overview of capillarity, the reader is referred to classic books and reviews such as de Gennes *et al.* [29], Butt and Kappl [35], and Kralchevsky and Nagayama [36].

1.4.1 Capillary geometry and force

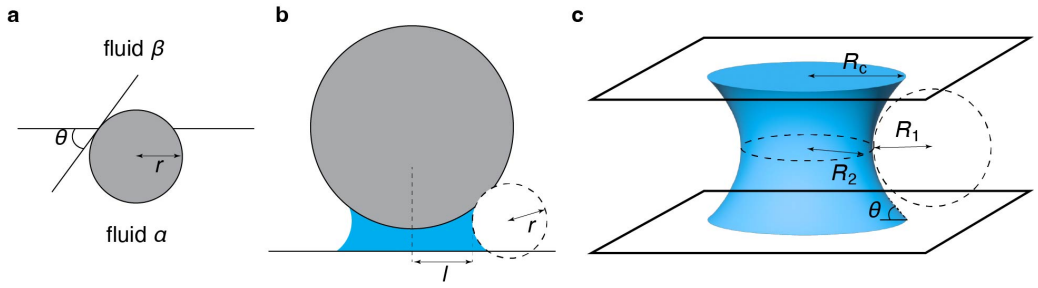

Figure 1.7: **(a)** A spherical particle adhering to a fluid–fluid interface with contact angle θ and radius r. **(b)** Schematic of a capillary meniscus between a sphere and a plane. **(c)** Capillary bridge formed between two parallel planes. The radii of curvature are labelled l and r in (b), and R_1 and R_2 in (c). R_c is the contact radius of the capillary bridge on the surface and θ is the contact angle.

Capillary interactions can occur both at solid–liquid interfaces and between solid surfaces connected by a liquid bridge. A familiar example of the first case is the adhesion of particles at fluid interfaces. Consider a spherical particle at a flat interface between two immiscible fluids. From a thermodynamic point of view, the particle attaches to the interface because this configuration minimises the total interfacial free energy of the system. When the particle moves from one bulk phase to the interface, part of the fluid–fluid interface is replaced by two solid–fluid interfaces, typically lowering the overall interfacial energy. The corresponding change in free

energy, known as the adhesion energy, is given by: [37]

$$\Delta E = -\pi r^2 \gamma_{\alpha\beta}(1 \pm \cos\theta)^2 \tag{1.10}$$

where $\gamma_{\alpha\beta}$ is the interfacial tension between fluids α and β, r is the particle radius, and θ is the equilibrium contact angle measured through fluid α. The positive or negative sign in Eq. 1.10 corresponds to detachment into phase β or α, respectively. This expression assumes that gravity and line tension are negligible. Typical values highlight the strength of this interaction. For a micron-sized particle at a water–oil interface, the adhesion energy can reach $\sim 10^6 k_\mathrm{B}T$ or higher. [38] Such large energies far exceed thermal fluctuations, explaining why particles are quasi-static irreversibly trapped at interfaces. This principle underlies the stability of Pickering emulsions, in which solid particles adsorb at oil–water interfaces to prevent coalescence, stabilising emulsions without surfactants.

Capillary bridges also form when a liquid connects two solid surfaces. An example is the building of sandcastles, where seawater forms liquid menisci between sand grains, generating strong adhesion and cohesion within the sand structure. Such liquid menisci often form through capillary condensation, in which vapour condenses between wettable surfaces. For instance, water vapour spontaneously condenses between a hydrophilic Atomic force microscopy (AFM) tip and a substrate such as glass or mica, creating a capillary bridge that resists tip retraction (details on AFM can be found in Section 2.1. [39] Alternatively, a capillary bridge can form when a liquid droplet is confined between two surfaces or interfaces. The resulting force originates from the combined effects of surface tension and Laplace pressure within the curved meniscus. The exact force expression depends on the interface geometry and the orientation of the confining surfaces. For a capillary bridge between a solid sphere and a plane: [6, 40, 41]

$$F_c = 2\pi l\gamma - \pi l^2 \Delta p \tag{1.11}$$

where l is the azimuthal radius at the narrowest part of the meniscus (the neck), and r is the meridional radius perpendicular to it. In a typical concave capillary bridge

(Fig. 1.7b), the interface has negative mean curvature under the sign convention adopted here, thus $\Delta p = p_{\text{in}} - p_{\text{out}} < 0$ relative to the surrounding fluid. In Eq. 1.11, the first term, $2\pi l\gamma$, represents the contribution of surface tension acting along the circular contact line, while the second term, $-\pi l^2 \Delta p$, accounts for the Laplace pressure acting over the meniscus cross section. Both terms contribute to an overall attractive capillary force that pulls the surfaces together. This expression follows the classical gorge method that simplifies the geometry by focusing on the neck of the capillary and assumes a small filling angle with a toroidal meniscus shape. [6, 40, 41] More detailed treatments for finite filling angles can be found in [35].

In this thesis, a more general case of interest is the bridge formed between two parallel plates (Fig. 1.7c). When gravity is negligible and both surfaces have identical contact angles, the capillary force is given by [42–44]:

$$F_c = 2\pi R_c \gamma \sin\theta - \pi {R_c}^2 \Delta P \tag{1.12}$$

where R_c is the contact radius (the radius of the three-phase contact line on the solid surface), γ is the surface tension, θ is the contact angle, and ΔP is the Laplace pressure defined by Eq. 1.5. This form explicitly includes the contact angle, which controls wetting and bridge stability. The contact radius and Laplace pressure depend on the plate separation, liquid volume, and contact angle, determined by minimising the total surface energy. Both formulations highlight that capillary forces arise from the interplay between surface tension and Laplace pressure. In experiments, what is often measured is the resultant adhesion force, which may also include contributions from gravity and line tension. Further discussion and comparison with simulations are provided in Result Chapters 3 and 4.

1.4.2 Capillary adhesion at interfaces

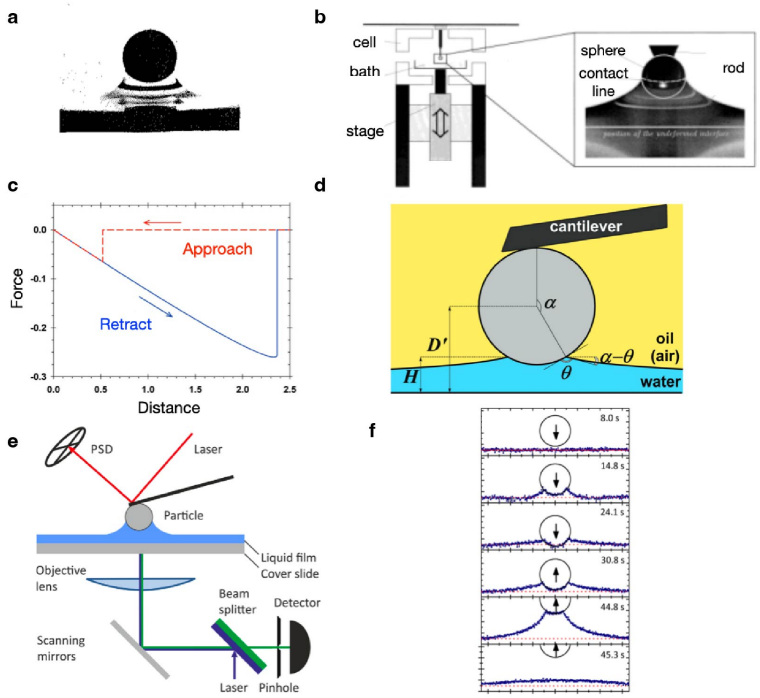

Figure 1.8: **(a)** From Huh and Mason: Teflon sphere (diameter = 12.70 mm) pulled through a silicone oil–water interface. [45] **(b)** From Pitois and Chateau: meniscus formed around a 500 μm sphere during force–distance measurement. [46] **(c–d)** From Anachkov *et al.*: (c) schematic of an approach–retraction force–distance experiment; (d) AFM cantilever with a colloidal sphere deforming a fluid interface. [47] **(e–f)** From Schellenberger *et al.*: (e) AFM–confocal setup; (f) confocal meniscus images. [48]

Adhesion lies at the heart of capillary interactions. It appears in two typical contexts: as the attractive force that binds two solids together through a liquid bridge (discussed later in bridging), or as the force that holds a solid particle at a liquid interface. In the latter case, the "bridge" is not between two solid surfaces, but between a solid and a deformable liquid interface. Thermodynamically, particles adhere to interfaces to minimise the total free energy of the system, and the strength of this adhesion is often characterised by the force or energy required to detach a particle.

The first quantitative study of this phenomenon was by Huh and Mason, who developed the classic sphere tensiometer. They pulled a millimetre-sized Teflon sphere through a silicone oil–water interface and measured the force using a mechanical balance (Fig. 1.8a). [45] This work provided early insight into the formation and

rupture of the meniscus and the corresponding force–distance behaviour, though precision was limited by gravity and experimental design. Since then, subsequent millimetre-scale studies followed, such as studies investigating capillary bridges between sphere–plate [49], and between two spheres [50]. A major step forward came with Pitois and Chateau who designed a more controlled apparatus to study small spheres down to 500 µm (Fig. 1.8b). They achieved quantitative agreement between measured and theoretical forces, emphasising how surface wettability controls adhesion strength. [46]

As research moved to smaller scales, attention shifted to microparticles relevant to emulsions [51] and foams [52]. At these scales, high precision and stable control of both the particle and the interface are required. Atomic force microscopy (AFM) has become the standard tool for measuring capillary forces thanks to its nanonewton precision and ability to manipulate individual particles. [48, 53, 54] Anachkov *et al.* used a colloidal AFM probe (with 6–7 µm diameter) to pull particles from various interfaces (Fig. 1.8c–d). [47] Schellenberger *et al.* advanced this further by coupling AFM with confocal microscopy to visualise the meniscus during detachment (Fig. 1.8e–f). [48]

However, these studies largely focus on micron-sized spherical particles. In modern nanomaterials and bioengineering, particles are often nanoscale and anisotropic. At these scales, new questions emerge. Does the classical thermodynamic picture, where the capillary force is described as the sum of surface tension and Laplace pressure, still apply? Do effects such as line tension at the contact line become significant? How can we quantify wettability and geometry when nanoscale roughness and heterogeneity dominate? These questions motivate the nanoparticle adhesion work presented in Chapter 3. In that chapter, we systematically quantify nanoparticle adhesion at liquid interfaces, explicitly accounting for geometry and surface chemistry, while examining the effects of nanoscale surface heterogeneity and line tension. This work establishes a framework adaptable to real-world nanoadhesion design, whether the goal is to promote or inhibit adhesion.

1.4.3 Capillary bridging

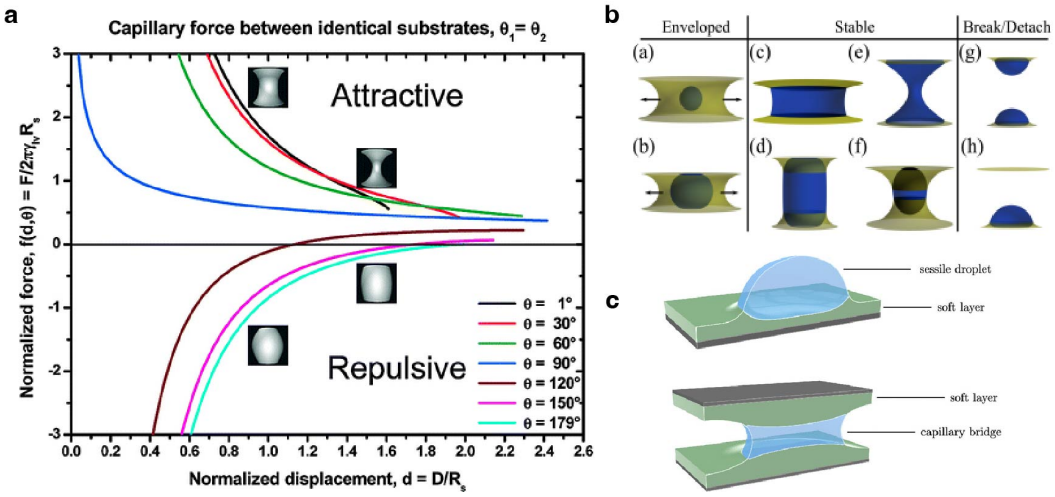

Figure 1.9: **(a)** From de Souza *et al.*: capillary force-displacement curves for varying contact angles. [55] **(b)** From Shek *et al.*: energy minimisation regimes of capillary bridges between liquid-infused surfaces. [56] **(c)** From Zheng and Chan: droplets and capillary bridges on soft substrates. [57]

If particle adhesion involves contact with a single interface, capillary bridging involves two interfaces connected by the same meniscus. This configuration plays an essential role in systems such as wet granular cohesion, coating formulations, and liquid transport. While the underlying force still arises from surface tension and Laplace pressure, the magnitude and direction depend strongly on geometry and surface wettability.

Classical geometries include sphere–sphere, cone–plate, and plate–plate systems, all governed by the same physical principles. [35, 49, 58–60] In this thesis, I place the emphasis on sphere–plate and plate–plate configurations (Figs. 1.7b-c). The sphere–plate bridge has been investigated since the 1950s, when McFarlane and Tabor measured the capillary adhesion between a glass sphere and a plate under controlled humidity, demonstrating how size, roughness, and liquid properties influence capillary force. [61] The plate–plate bridge offers a simpler geometry for analysing force–distance behaviour and bridge morphology. Carter examined liquid bridges between parallel plates of different wettabilities [62], and later studies extended to quantify dynamic deformation and rupture. [63, 64] The bridge shape and force depend primarily on the contact angle and its hysteresis. Therefore, De Souza

et al. showed how contact angle hysteresis alters measured forces (Fig. 1.9a) [55, 65], and Nagy used capillary bridges to extract advancing and receding contact angles on surfaces from hydrophilic to superhydrophobic. [66] Other work, such as that of Rodrigues *et al.*, demonstrated that chemical patterning can bias bridge motion and capillary forces. [67]

The theoretical foundation for bridge stability originates from Plateau, who studied liquid columns held between circular rings and established the geometric limits of capillary stability. [68–70] He showed that a cylindrical bridge remains stable only up to an aspect ratio of approximately $L/R = 2\pi$; beyond this limit, the column breaks into droplets to minimise surface energy. Plateau's quasi-static experiments defined equilibrium bridge shapes as surfaces of constant mean curvature, forming the basis of all modern capillarity theory. Later, Rayleigh extended the analysis to dynamic conditions, describing how small perturbations evolve in time and lead to breakup, which is the classical Plateau–Rayleigh instability. [71, 72] Subsequent analytical work by Fisher [6], Erle *et al.* [73], and Orr *et al.* [74] further refined the capillary force expressions, providing the quantitative framework still used today.

More recently, interest has moved to soft and liquid-like surfaces, where the boundaries themselves can deform or flow. These are particularly relevant in biological and functional materials. Shek *et al.* showed that in capillary bridges formed between liquid-infused surfaces, the oil ridges at the three-phase contact line resist bridge motion (Fig. 1.9b) [56], while Zheng and Chan demonstrated how soft substrates modify apparent contact angles and affect bridge movement (Fig. 1.9c) [57]. Building on this, Chapter 4 combines experiments and simulations of capillary bridge stretching and compression on hydrophilic, hydrophobic, and liquid-infused surfaces to quantify bridge geometry and capillary forces. Particular emphasis is placed on the roles of substrate wettability, solid or liquid character, and gravitational deformation, thereby assessing how classical capillary theory extends across these distinct surface systems.

1.4.4 Capillary-driven removal

Capillary-driven removal is a newly introduced approach to overcoming droplet adhesion by capillary forces. Instead of bridging and sticking droplets, capillary forces are used here to dewet, lift, and detach droplets from surfaces. This concept links fundamental capillarity to practical applications and serves as the final focus of this thesis.

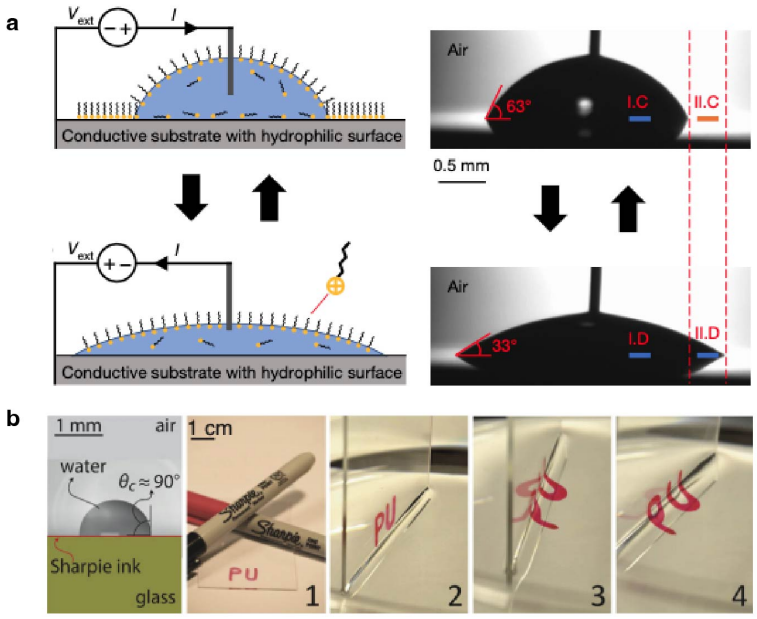

Figure 1.10: **(a)** From Li *et al.*: ionic surfactant-mediated electrodewetting mechanism, with a sessile droplet deposited on a conductive, hydrophilic substrate and an electric field drives the ionic surfactants. [75] **(b)** From Khodaparast *et al.*: a hydrophobic film was peeled off and transferred to an air-water interface as the substrate is slowly dipped into a water bath. [76]

Dewetting describes a liquid retracting its contact with a surface, which is the opposite of spreading. In a binary liquid–gas system, it can occur through several mechanisms: droplet impact, where droplets bounce off the surface after collision as kinetic energy is released [77]; electrowetting, where the contact angle of a liquid is controlled by applying a voltage (Fig. 1.10a) [78]; evaporation, often accompanied by Marangoni flows that produce patterns such as the coffee-ring effect [79]; and spinodal instability, where a thin liquid film becomes unstable and breaks up into droplets [80].

While the examples above describe liquid dewetting and removal, capillary forces

can also act to detach solid films. Pioneering work by Khodaparast *et al.* showed that a hydrophobic polymer film can be peeled off a substrate as it is slowly immersed into water, where the advancing air–water interface exerts a capillary force strong enough to lift the film (Fig. 1.10b) [76]. This example demonstrates that interfacial tension can be harnessed for efficient detachment.

Building on these binary liquid–air systems, dewetting in ternary configurations, where a droplet interacts with another immiscible liquid, remains much less explored. Understanding how droplets detach in such systems is advantageous for applications such as oil recovery, coatings, and surface cleaning. Inspired by capillary bridges, we propose harnessing capillary forces to lift droplets in these environments. When two liquids meet, a meniscus bridge can form between the substrate and the rising interface, lifting the droplet by the intrinsic interfacial tension. Because water has a high surface tension, no surfactant is required.

This concept opens new opportunities for droplet manipulation, from microfluidics to surface cleaning. By controlling geometry, wettability, and phase configuration, capillary-driven removal offers a way to reverse adhesion and achieve dewetting while minimising energy and resource use. Chapter 5 introduces a capillary lifting mechanism for droplet removal in ternary systems, identifies the governing interfacial force balance and geometry, and establishes a predictive regime map defining the conditions for efficient droplet detachment, with validation across both model and real-world systems.

1.5 Thesis aims and structure

This thesis explores capillary interactions at solid and liquid interfaces through three main parts: particle adhesion, capillary bridging, and capillary-driven droplet removal. Together, these studies describe how capillary forces act across different scales and surface conditions, connected by the shared physics of surface tension and Laplace pressure. The principal research questions and contributions of this thesis are summarised below.

- We ask how nanoscale particles adhere to liquid interfaces; we combine AFM experiments and modelling; we assess the validity of classical capillary theory at the nanoscale (Chapter 3).

- We ask how wettability and gravity affect capillary bridge geometry and force on solid and functional surfaces; we conduct experiments and theoretical analysis on hydrophilic, hydrophobic, and liquid-infused surfaces; we contribute a comparative understanding of bridge mechanics across these surface classes (Chapter 4).

- We ask how droplets can be removed efficiently by interfacial lifting; we develop a capillary lifting strategy in ternary systems; we contribute a physics-based route for efficient droplet detachment with minimal resource consumption (Chapter 5).

- Overall, we ask how capillary interactions can be understood and leveraged across scales; we integrate these studies experimentally and computationally; we contribute unified design principles for capillary-driven adhesion, bridging, and removal.

The detailed structure of the thesis is as follows.

Chapter 2 (Methodology) introduces the experimental and modelling approaches used throughout the work. It covers the design of liquid-infused surfaces, the Surface Evolver simulations, the custom-built device for studying droplet dewetting, and the use of Atomic force microscopy (AFM) to measure capillary forces. The focus of this thesis is on quasi-static conditions, where the interfaces are moved slowly enough that their shapes are governed mainly by energy minimisation.

Chapter 3 examines how nanoscale particles adhere to liquid interfaces. Using both modelling and AFM experiments, it explores how particle geometry, surface chemistry, and line tension influence the strength of attachment and the energy required for detachment.

Chapter 4 investigates capillary bridges formed between two parallel surfaces that are hydrophilic, hydrophobic, or liquid-infused. The work focuses on the millimetre

scale, where the effect of gravity becomes comparable to surface tension. The results provide a useful benchmark for understanding how bridge shape, stability, and force balance change with surface properties.

Chapter 5 brings these ideas together, showing how capillary forces can be used for droplet removal. By forming and lifting liquid bridges within a three-phase system, droplets can be detached efficiently without chemical additives. This part connects the fundamental physics of capillarity to practical applications such as cleaning and advanced oil recovery.

Together, these studies present a picture of how capillary forces operate from the nanoscale to the macroscopic scale at solid and liquid interfaces. They demonstrate how tuning surface chemistry and geometry can control adhesion, bridging, and removal, opening new avenues of manipulating liquid interfaces in natural and engineered systems.

References

[1]Sabine, *Water striders nature evertebrat - free photo on pixabay*, (2018) `https://pixabay.com/photos/water-striders-nature-evertebrat-3322665/` (visited on 10/15/2025).

[2]A. Fall, B. Weber, M. Pakpour, N. Lenoir, N. Shahidzadeh, J. Fiscina, C. Wagner, and D. Bonn, "Sliding friction on wet and dry sand", Physical Review Letters **112**, 175502 (2014).

[3]P. E. Newberry, *El bersheh: the tomb of tehuti-hetep* (Egypt Exploration Fund, 1895), 160 pp.

[4]D. L. Hu, B. Chan, and J. W. M. Bush, "The hydrodynamics of water strider locomotion", Nature **424**, 663–666 (2003).

[5]T. Horikawa, D. D. Do, and D. Nicholson, "Capillary condensation of adsorbates in porous materials", Advances in Colloid and Interface Science **169**, 40–58 (2011).

[6]R. A. Fisher, "On the capillary forces in an ideal soil; correction of formulae given by w. b. haines", The Journal of Agricultural Science **16**, 492–505 (1926).

[7]G. Soligno, M. Dijkstra, and R. van Roij, "Self-assembly of cubes into 2d hexagonal and honeycomb lattices by hexapolar capillary interactions", Physical Review Letters **116**, 258001 (2016).

[8]S. Ni, J. Leemann, I. Buttinoni, L. Isa, and H. Wolf, "Programmable colloidal molecules from sequential capillarity-assisted particle assembly", Science Advances **2**, e1501779 (2016).

[9]Z. Zhao, W. Wang, G. Xiang, L. Jiang, and X. Jiang, "Capillary-assisted confinement assembly for advanced sensor fabrication: from superwetting interfaces to capillary bridge patterning", ACS Nano **19**, 3019–3036 (2025).

[10]Y. Wang, H. Xu, W. Yu, B. Bai, X. Song, and J. Zhang, "Surfactant induced reservoir wettability alteration: recent theoretical and experimental advances in enhanced oil recovery", Petroleum Science **8**, 463–476 (2011).

[11]A. Olanrewaju, M. Beaugrand, M. Yafia, and D. Juncker, "Capillary microfluidics in microchannels: from microfluidic networks to capillaric circuits", Lab on a Chip **18**, 2323–2347 (2018).

[12]W. J. Hyun, E. B. Secor, F. Z. Bidoky, S. B. Walker, J. A. Lewis, M. C. Hersam, L. F. Francis, and C. D. Frisbie, "Self-aligned capillarity-assisted printing of top-gate thin-film transistors on plastic", Flexible and Printed Electronics **3**, 035004 (2018).

[13]U. Nations, *Partnerships and cooperation for water, industry and energy*, UN World Water Development Report 2023, `https://www.unesco.org/reports/wwdr/2023/en/industry-and-energy` (visited on 09/04/2025).

[14]M. R. Panda and Y. Kim, "Gridded global dataset of industrial water use predicted using the random forest", Scientific Data **11**, 1331 (2024).

[15]U. E. P. Agency, *Water use and water waste at industrial facilities*, Lean & Water Toolkit: Chapter 2, (Feb. 6, 2017) `https://www.epa.gov/sustainability/lean-water-toolkit-chapter-2` (visited on 09/04/2025).

[16]P. Johnson, A. Trybala, V. Starov, and V. J. Pinfield, "Effect of synthetic surfactants on the environment and the potential for substitution by biosurfactants", Advances in Colloid and Interface Science **288**, 102340 (2021).

[17]U. Nations, *THE 17 GOALS — sustainable development*, (2015) `https://sdgs.un.org/goals` (visited on 09/03/2025).

[18]H.-J. Butt, K. Graf, and M. Kappl, "Thermodynamics of interfaces", in *Physics and chemistry of interfaces* (John Wiley & Sons, Ltd, 2003), pp. 26–41.

[19]K. A. Brakke, "The surface evolver", Experimental Mathematics **1**, 141–165 (1992).

[20]T. Young, "An essay on the cohesion of fluids", **95**, 65–87 (1805).

[21]O. V. Voinov, "Hydrodynamics of wetting", Fluid Dynamics **11**, 714–721 (1976).

[22]T. Vukovic, J. Røstad, U. Farooq, O. Torsæter, and A. van der Net, "Systematic study of wettability alteration of glass surfaces by dichlorooctamethyltetrasiloxane silanization: a guide for contact angle modification", ACS Omega **8**, 36662–36676 (2023).

[23]S. Iglauer, A. Salamah, M. Sarmadivaleh, K. Liu, and C. Phan, "Contamination of silica surfaces: impact on water–CO2–quartz and glass contact angle measurements", International Journal of Greenhouse Gas Control **22**, 325–328 (2014).

[24]D. Rymuszka, K. Terpilowski, and L. Hołysz, "Influence of volume drop on surface free energy of glass", Annales Universitatis Mariae Curie-Sklodowska sectio AA – Chemia **68**, 1–2 (2014).

[25]M. Wei, R. S. Bowman, J. L. Wilson, and N. R. Morrow, "Wetting properties and stability of silane-treated glass exposed to water, air, and oil", Journal of Colloid and Interface Science **157**, 154–159 (1993).

[26]F. Schellenberger, "How water advances on superhydrophobic surfaces", Physical Review Letters **116**, `10.1103/PhysRevLett.116.096101` (2016).

[27]T.-S. Wong, S. H. Kang, S. K. Y. Tang, E. J. Smythe, B. D. Hatton, A. Grinthal, and J. Aizenberg, "Bioinspired self-repairing slippery surfaces with pressure-stable omniphobicity", Nature **477**, 443–447 (2011).

[28]E. Nowak, P. Robbins, G. Combes, E. H. Stitt, and A. W. Pacek, "Measurements of contact angle between fine, non-porous particles with varying hydrophobicity and water and non-polar liquids of different viscosities", Powder Technology **250**, 21–32 (2013).

[29]P.-G. De Gennes, F. Brochard-Wyart, and D. Quéré, *Capillarity and wetting phenomena* (Springer, New York, NY, 2004).

[30]R. Lenormand, E. Touboul, and C. Zarcone, "Numerical models and experiments on immiscible displacements in porous media", Journal of Fluid Mechanics **189**, 165–187 (1988).

[31]B. E. Rapp, "Chapter 21 - capillarity", in *Microfluidics: modelling, mechanics and mathematics*, edited by B. E. Rapp, Micro and Nano Technologies (Elsevier, Oxford, Jan. 1, 2017), pp. 445–451.

[32]O. Reynolds, "XXIX. an experimental investigation of the circumstances which determine whether the motion of water shall be direct or sinuous, and of the law of resistance in parallel channels", Philosophical Transactions of the Royal Society of London **174**, 935–982 (1883).

[33]V. Mukund and B. Hof, "The critical point of the transition to turbulence in pipe flow", Journal of Fluid Mechanics **839**, 76–94 (2018).

[34]K. V. Sharp and R. J. Adrian, "Transition from laminar to turbulent flow in liquid filled microtubes", Experiments in Fluids **36**, 741–747 (2004).

[35]H.-J. Butt and M. Kappl, "Normal capillary forces", Advances in Colloid and Interface Science **146**, 48–60 (2009).

[36]P. A. Kralchevsky and K. Nagayama, "Chapter 11 - capillary bridges and capillary-bridge forces", in *Studies in interface science*, Vol. 10, edited by P. A. Kralchevsky and K. Nagayama, Particles at Fluids Interfaces and Membranes (Elsevier, Jan. 1, 2001), pp. 469–502.

[37]B. P. Binks, "Particles as surfactants—similarities and differences", Current Opinion in Colloid & Interface Science **7**, 21–41 (2002).

[38]A.-L. Fameau, E. Guzmán, H. A. Ritacco, and A. Saint-Jalmes, "Interfacial properties of protein particles at fluid/fluid interfaces and relationship with the stability of foams and emulsions", Frontiers in Soft Matter **3**, 10.3389/frsfm.2023.1016061 (2023).

[39]X. D. Xiao and L. M. Qian, "Investigation of humidity-dependent capillary force", Langmuir **16**, 8153–8158 (2000).

[40]K. Hotta, K. Takeda, and K. Iinoya, "The capillary binding force of a liquid bridge", Powder Technology **10**, 231–242 (1974).

[41]W. C. Clark, J. M. Haynes, and G. Mason, "Liquid bridges between a sphere and a plane", Chemical Engineering Science **23**, 810–812 (1968).

[42]H. Kusumaatmaja and R. Lipowsky, "Equilibrium morphologies and effective spring constants of capillary bridges", Langmuir **26**, 18734–18741 (2010).

[43]P. V. Petkov and B. Radoev, "Investigation of single and binary of "sandwich" type convex liquid capillary bridges, stretched between two flat surfaces (experimental approach)", Colloids and Interfaces **3**, 68 (2019).

[44]E. J. De Souza, M. Brinkmann, C. Mohrdieck, and E. Arzt, "Enhancement of capillary forces by multiple liquid bridges", Langmuir **24**, 8813–8820 (2008).

[45]C. Huh and S. G. Mason, "Sphere tensiometry: an evaluation and critique", Canadian Journal of Chemistry **54**, 969–978 (1976).

[46]O. Pitois and X. Chateau, "Small particle at a fluid interface: effect of contact angle hysteresis on force and work of detachment", Langmuir **18**, 9751–9756 (2002).

[47]S. E. Anachkov, I. Lesov, M. Zanini, P. A. Kralchevsky, N. D. Denkov, and L. Isa, "Particle detachment from fluid interfaces: theory vs. experiments", Soft Matter **12**, 7632–7643 (2016).

[48]F. Schellenberger, P. Papadopoulos, M. Kappl, S. A. L. Weber, D. Vollmer, and H.-J. Butt, "Detaching microparticles from a liquid surface", Physical Review Letters **121**, 048002 (2018).

[49]E. Bayramli and T. G. M. van de Ven, "An experimental study of liquid bridges between spheres in a gravitational field", Journal of Colloid and Interface Science **116**, 503–510 (1987).

[50]O. Pitois, P. Moucheront, and X. Chateau, "Liquid bridge between two moving spheres: an experimental study of viscosity effects", Journal of Colloid and Interface Science **231**, 26–31 (2000).

[51]M. Zanini, C. Marschelke, S. E. Anachkov, E. Marini, A. Synytska, and L. Isa, "Universal emulsion stabilization from the arrested adsorption of rough particles at liquid-liquid interfaces", Nature Communications **8**, 15701 (2017).

[52]F. Gorlier, Y. Khidas, and O. Pitois, "Elasticity of particle-loaded liquid foams", Soft Matter **13**, 4533–4540 (2017).

[53]J. Ally, E. Vittorias, A. Amirfazli, M. Kappl, E. Bonaccurso, C. E. McNamee, and H.-J. Butt, "Interaction of a microsphere with a solid-supported liquid film", Langmuir **26**, 11797–11803 (2010).

[54]S. Friedrich and B. Cappella, "Study of micro- and nanoscale wetting properties of lubricants using AFM force–distance curves", Tribology Letters **68**, 36 (2020).

[55]E. J. De Souza, L. Gao, T. J. McCarthy, E. Arzt, and A. J. Crosby, "Effect of contact angle hysteresis on the measurement of capillary forces", Langmuir **24**, 1391–1396 (2008).

[56]A. C. M. Shek, C. Semprebon, J. R. Panter, and H. Kusumaatmaja, "Capillary bridges on liquid-infused surfaces", Langmuir **37**, 908–917 (2021).

[57]B. X. Zheng and T. S. Chan, "Soft wetting ridge rotation in sessile droplets and capillary bridges", Langmuir **41**, 4146–4153 (2025).

[58]S. Goodband, H. Kusumaatmaja, and K. Voïtchovsky, "Development of a setup to characterize capillary liquid bridges between liquid infused surfaces", AIP Advances **12**, 015120 (2022).

[59]M. Miot, G. Veylon, A. Wautier, P. Philippe, F. Nicot, and F. Jamin, "Numerical analysis of capillary bridges and coalescence in a triplet of spheres", Granular Matter **23**, 1–18 (2021).

[60]E. A. Boucher and H. J. Kent, "Capillary phenomena. part 5.—equilibrium and stability of solid cones in fluid/fluid interfaces", Journal of the Chemical Society, Faraday Transactions 1: Physical Chemistry in Condensed Phases **73**, 1882–1890 (1977).

[61]J. S. McFarlane and D. Tabor, "Adhesion of solids and the effect of surface films", Proceedings of the Royal Society of London. Series A. Mathematical and Physical Sciences **202**, 224–243 (1950).

[62]W. C. Carter, "The forces and behavior of fluids constrained by solids", Acta Metallurgica **36**, 2283–2292 (1988).

[63]P. V. Petkov and B. P. Radoev, "Statics and dynamics of capillary bridges", Colloids and Surfaces A: Physicochemical and Engineering Aspects, 27th European Colloid and Interface Society conference (27th ECIS 2013) **460**, 18–27 (2014).

[64]Z. Adak and M. H. Ghazanfari, "A new insight into the stability of static and dynamic liquid bridges in smooth-walled horizontal fractures", Journal of Molecular Liquids **398**, 124188 (2024).

[65]E. J. De Souza, M. Brinkmann, C. Mohrdieck, A. Crosby, and E. Arzt, "Capillary forces between chemically different substrates", Langmuir **24**, 10161–10168 (2008).

[66]N. Nagy, "Capillary bridges on hydrophobic surfaces: analytical contact angle determination", Langmuir **38**, 6201–6208 (2022).

[67]M. S. Rodrigues, R. C. V. Coelho, and P. I. C. Teixeira, "Dynamics of liquid bridges between patterned surfaces", Physica D: Nonlinear Phenomena **469**, 134322 (2024).

[68]J. A. F. Plateau, *Experimental and theoretical researches on the figures of equilibrium of a liquid mass withdrawn from the action of gravity, etc.* (Smithsonian Institution, Washington, 1863), 23 pp.

[69]J. A. F. Plateau, *Statique expérimentale et théorique des liquides soumis aux seules forces moléculaires* (Paris, Gauthier-Villars, 1873), 518 pp.

[70]J. Plateau, "VII. experimental and theoretical researches into the figures of equilibrium of a liquid mass without weight.—seventh series", The London, Edinburgh, and Dublin Philosophical Magazine and Journal of Science **33**, 39–47 (1867).

[71]L. Rayleigh, "On the capillary phenomena of jets", Proceedings of the Royal Society of London **29**, 71–97 (1879).

[72]L. Rayleigh, "On the stability, or instability, of certain fluid motions", Proceedings of the London Mathematical Society **s1-11**, 57–72 (1879).

[73]M. A. Erle, D. C. Dyson, and N. R. Morrow, "Liquid bridges between cylinders, in a torus, and between spheres", AIChE Journal **17**, 115–121 (1971).

[74]F. M. Orr, L. E. Scriven, and A. P. Rivas, "Pendular rings between solids: meniscus properties and capillary force", Journal of Fluid Mechanics **67**, 723–742 (1975).

[75]J. Li, N. S. Ha, T. L. Liu, R. M. van Dam, and C.-J. 'CJ' Kim, "Ionic-surfactant-mediated electro-dewetting for digital microfluidics", Nature **572**, 507–510 (2019).

[76]S. Khodaparast, F. Boulogne, C. Poulard, and H. A. Stone, "Water-based peeling of thin hydrophobic films", Physical Review Letters **119**, 154502 (2017).

[77]D. Richard and D. Quéré, "Bouncing water drops", Europhysics Letters **50**, 769 (2000).

[78]F. Mugele and J.-C. Baret, "Electrowetting: from basics to applications", Journal of Physics: Condensed Matter **17**, R705 (2005).

[79]R. D. Deegan, O. Bakajin, T. F. Dupont, G. Huber, S. R. Nagel, and T. A. Witten, "Capillary flow as the cause of ring stains from dried liquid drops", Nature **389**, 827–829 (1997).

[80]G. Reiter, "Dewetting of thin polymer films", Physical Review Letters **68**, 75–78 (1992).

Chapter 2

Methodology

Throughout this thesis, we combine experimental measurements with computational modelling to investigate capillary interactions. This integrated approach enables exploration of a broader parameter space while maintaining experimental validation. Depending on the type of interaction studied, namely adhesion, bridging, or removal, different experimental setups are developed to match the relevant length scales and interfacial conditions. For the simulations, we primarily employed Surface Evolver [1], a quasi-static energy minimisation software. Detailed methodologies are presented in the respective results chapters, while this chapter provides an overview of the techniques and materials used, their broader relevance in the soft matter field, and the general framework of their application in this thesis.

2.1 Atomic force microscopy (AFM)

Atomic force microscopy (AFM) is employed in this thesis primarily for the capillary adhesion study described in Chapter 3. In this context, AFM enables direct measurement of the force required to detach a nanoparticle from a liquid interface, providing quantitative insight into the capillary adhesion profile at the nanoscale. The technique offers piconewton-level sensitivity while also allowing precise control of the interaction between the particle and the liquid interface. Another application of AFM in this thesis is topographic imaging, as described in Section 3.3.3. It is employed to characterise the roughness of a platinum film by acquiring high-resolution surface topography. The resulting roughness ratio is used to apply the Wenzel correction to the measured wettability. These two applications highlight two typical capabilities of AFM, mechanical force measurements and high-resolution mapping of surface structure. Both aspects are essential for the capillarity studies presented in this thesis.

2.1.1 Principle of operation

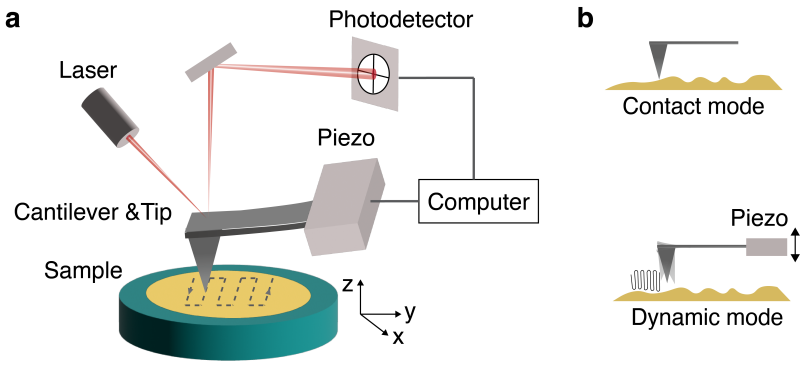

Figure 2.1: Atomic Force Microscopy (AFM) principle **(a)** and working modes **(b)**.

AFM was first introduced in 1986 by Binnig *et al.* [2] as an extension of the scanning tunnelling microscope, with the key advantage of enabling the imaging of non-conductive samples. The fundamental principle of AFM is that a nanoscale sharp tip is mounted on a flexible cantilever, which behaves as a spring following Hooke's law. The cantilever is driven by a piezoelectric scanner, enabling the attached tip to raster scan across the sample surface. As the tip interacts with surface features, the cantilever bends in response to the tip-sample interaction forces. The resulting deflection is monitored by a laser beam reflected onto a position-sensitive photodetector, as shown in Fig. 2.1a. The detected signal is processed in a feedback loop that continuously adjusts the vertical position of the cantilever to maintain a near-constant interaction force between the tip and the sample surface.

The two most common AFM operation modes are contact mode and dynamic mode, as sketched in Figure 2.1b. In contact mode, the cantilever is pressed against the surface so that the tip experiences a repulsive force. The interaction force is controlled by maintaining a constant cantilever deflection throughout the scan. In dynamic mode, the cantilever is driven into oscillation near its fundamental resonance frequency by the piezoelectric scanner. As the cantilever approaches the sample, the tip lightly interacts with the surface, which causes damping of the oscillation amplitude. Rather than regulating static deflection as in contact mode, dynamic mode maintains a constant change in oscillation amplitude. The feedback loop continuously adjusts the vertical position of the cantilever to preserve this condition. Since the tip interacts only slightly with the surface, dynamic mode greatly

reduces tip–sample contact and thereby minimises damage to both the tip and the sample.

2.1.2 Force–distance measurements

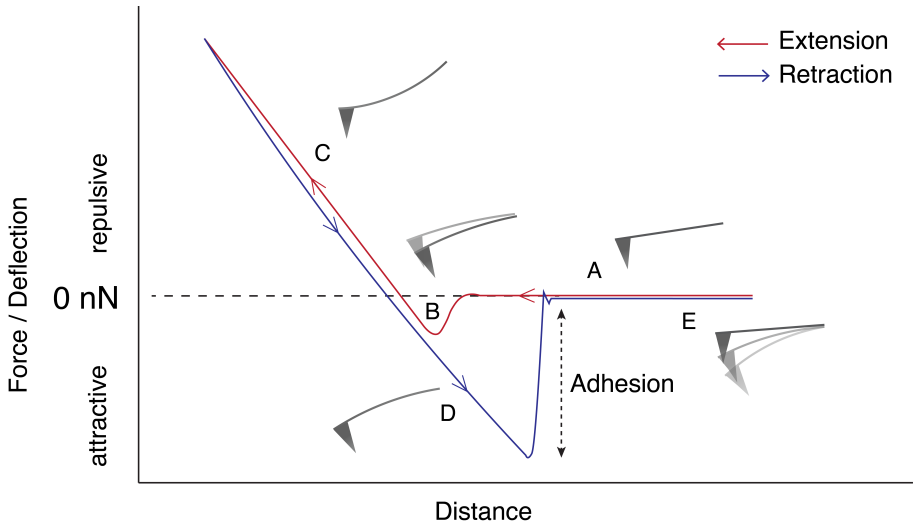

Figure 2.2: Schematic AFM force curve with approach marked in red and retraction marked in blue.

In this thesis, I focus on one of the key capabilities of AFM: force–distance curve measurements, which provide local information on material properties such as hardness and elasticity [3]. In these measurements, the cantilever is driven towards the sample and then retracted, while the relative displacement of the piezoelectric scanner and the cantilever deflection are monitored. Using the deflection sensitivity and the cantilever spring constant, these values are converted into a force–separation relationship, producing a force curve such as that shown in Fig. 2.2. Segments A–C (red line) correspond to the extension phase, while segments D–E (blue line) represent the retraction phase. During extension, the cantilever approaches the sample surface (A) and suddenly snaps into contact due to attractive tip-surface interactions (B). As the tip continues to indent the sample, the cantilever experiences a strong repulsive force and bends (C). Once the maximum load force is reached, the retraction phase begins as the piezoelectric scanner withdraws the cantilever from the surface. For an adhesive tip, attractive interactions continue to pull the tip towards the surface during withdrawal, producing a pull-off event (D). Finally, the

cantilever detaches completely and returns to its unperturbed state (E). The above process presents a typical force curve under contact mode where constant force is maintained across the scan, which is often employed for cantilever spring constant calibration.

2.1.3 Dynamic mode AFM for force–distance measurements

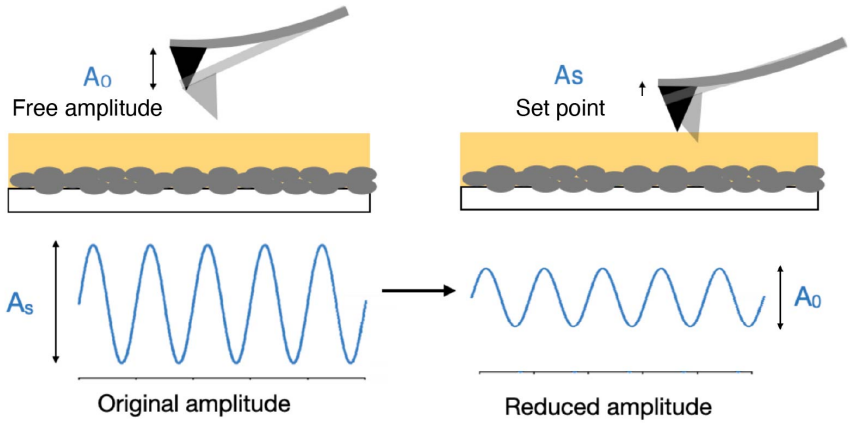

Figure 2.3: Sketch of using dynamic amplitude modulation AFM for adhesion force measurement on LIS.

While contact mode offers a simple and direct approach for acquiring both force–distance curves and topographic images, it is not suitable for probing soft surfaces or fluid interfaces. On soft materials, direct contact readily introduces excessive normal forces that cause deformation. At fluid interfaces, controlled tip indentation into the liquid phase is required, which cannot be achieved reliably using conventional contact mode. These limitations are particularly relevant to this thesis, where measuring the capillary adhesion of a nanoscale AFM tip at liquid interfaces requires high-precision control of solid–fluid interactions. The need for careful control is further emphasised by the fragility of AFM probes and the complexity of the studied samples. For example, in liquid-infused surfaces (LIS) containing Glaco^{TM} nanoparticles beneath the lubricating liquid (see details in Section 2.2.2), it is crucial to prevent the tip from penetrating into the underlying nanoparticle layer. Direct contact with the silicone-based nanoparticles could lead to abrasion, tip fracture, or irreversible adhesion, any of which could result in experimental failure or irre-

producible measurements. These considerations make the choice of AFM feedback mode for force measurements a critical aspect of the methodology.

To tackle this issue, we employed a dynamic operation mode known as amplitude modulation (AM-AFM). In this mode, the cantilever is driven sinusoidally at its resonance frequency by the piezoelectric scanner. This resonance is first identified by sweeping the drive frequency across a broad range and locating the fundamental peak in the response spectrum. The cantilever is then excited at resonance, behaving as a simple harmonic oscillator. As illustrated in Fig. 2.3, when the tip approaches the sample, its free oscillation amplitude A_0 decreases due to tip–sample interactions. Retraction is initiated once the amplitude is reduced to a setpoint value A_s, which defines the turning point of the force–distance curve. The ratio A_s/A_0 represents the retained oscillation amplitude, while $1 - A_s/A_0$ defines the amplitude reduction ratio. This dynamic mode provides nanometre-scale control over tip–liquid interface interactions and is therefore essential for probing the adhesion force profiles presented in Chapter 3.

2.2 Liquid-infused surfaces (LIS)

Liquid-infused surfaces (LIS) play two roles in this thesis. First, they serve as model liquid–air interfaces, providing a micron-thick, flat lubricant layer for the study of nanoscale capillary adhesion. Second, they are employed in the capillary bridging study, where the force response and geometrical evolution of capillary structures are examined under compression–extension cycles. This extends the scope of analysis beyond conventional capillary bridges formed between solid surfaces. Collectively, these studies show the frictionless and mobile fluidic nature of LIS and demonstrate how such characteristics can be employed to advance the fundamental understanding of capillarity at complex interfaces.

2.2.1 Principles of LIS

Liquid-infused surfaces (LIS) are bio-inspired, self-cleaning surfaces composed of a viscous lubricating liquid held in place by a textured or porous substrate [6, 7]

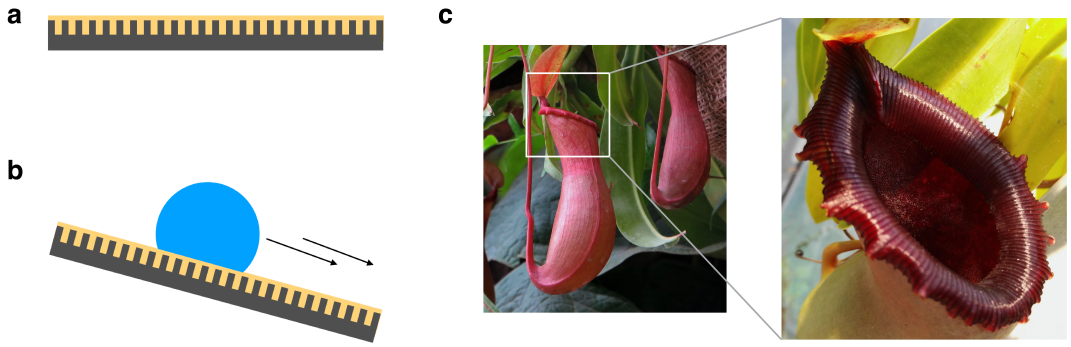

Figure 2.4: **(a)** Sketch of a typical liquid-infused surface (LIS). **(b)** A droplet rolling down an LIS. **(c)** Photographs of *Nepenthes* pitcher plants; inset: macroscopic groove on the peristome. Images by Koszecz Sándor [4] and DEZALB [5], sourced from Pixabay and used under the Pixabay Content License.

(Fig. 2.4a–b). The concept is inspired by the *Nepenthes* pitcher plant, whose peristome microstructures trap a thin water film. This hydrophilic layer is highly slippery for hydrophobic insect feet, causing insects to lose traction, slip, and eventually fall into the pitcher where they are digested [8, 9](Fig. 2.4c). Since their introduction in 2011, LIS have attracted increasing attention due to their ability to reduce adhesion and promote self-cleaning. These features enable a broad spectrum of functionalities, including anti-icing, drag reduction, and anti-fouling, making LIS promising candidates for diverse industrial applications [10–12]. For instance, droplets on LIS exhibit minimal contact-line pinning ($\leq 2.5°$) and friction, allowing them to slide off at very slight inclines ($\leq 5°$ for droplet volume $\geq 2\,\mu$L) [6]. LIS also prevent more than 95% of biofilm attachments over a week, corresponding to a 35 times reduction compared with the best performing solid substrates [11, 13]. Furthermore, the freezing time of droplets on LIS can be delayed by more than an order of magnitude relative to glass surfaces [14].

Despite the outstanding self-cleaning performance of LIS, many fundamental questions remain unclear. For example, while the anti-fouling efficacy suggests that particles and organisms adhere only weakly, there is a lack of quantitative measurements of adhesion forces on LIS. A critical question is whether a particle such as a microorganism or debris that attaches to a liquid-infused coating requires significant energy or force to be detached. The answer is central to understanding the limits of LIS performance, since it determines the threshold at which fluid flow or cleaning

procedures become effective in removing contaminants.

Another open question arises when LIS are used in confined geometries, such as a liquid droplet trapped between two LIS. In conventional systems, a capillary bridge can generate strong adhesive and capillary forces between solid substrates. However, it remains unclear how such bridges behave when one or both surfaces are LIS, and how the presence of the infused lubricant modifies their geometry and force response. In particular, if LIS are employed in narrow processing channels or microfluidic devices, it is not known whether a transferred droplet would detach more readily due to the slippery nature of the surfaces, or whether it might instead exhibit new modes of stability and failure associated with the formation of lubricant ridges at its contact with the LIS. These knowledge gaps highlight the need for a deeper quantitative understanding of the physics governing LIS interfaces. Therefore, this thesis investigates particle capillary adhesion in Chapter 3, followed by an examination of capillary bridge behaviour in Chapter 4.

2.2.2 Fabrication of LIS in this thesis

The fabrication of LIS in this thesis is adapted from Goodband *et al.* [15] and Orme *et al.* [16], with full details provided in Section 3.3.1. In brief, a rough, porous surface is prepared by spraying successive layers of silicone nanoparticles onto a clean glass slide. Silicone oil is selected as the lubricant, representing a model lubricant oil commonly used in manufacturing. The oil is spin-coated onto the prepared substrates to form a smooth and stable lubricant layer of micrometre thickness. This fabrication methodology is chosen for its simplicity compared with other approaches that require lithography, as well as for its durability. Tests have shown that the surface can retain a lubricant layer approximately $3\,\mu$m thick for up to 16 days after fabrication. [15]

2.3 Fluidic device for droplet dewetting

We developed a custom fluidic device to study droplet removal through capillary lifting (Chapter 5), enabling precise fluid injection and optimised visualisation. Two

versions of the device are fabricated in-house, aiming to achieve a more symmetric injected flow. Such symmetry is essential, as the droplets and interfaces are small and highly sensitive, meaning that even minor external disturbances can deform them and obscure the specific role of capillary lifting. Because the study of droplet removal by capillary forces requires an integrated approach that combines experiments and simulations, it is also necessary to ensure that the device dimensions and geometrical features are closely matched to the corresponding simulation framework.

2.3.1 Device designs

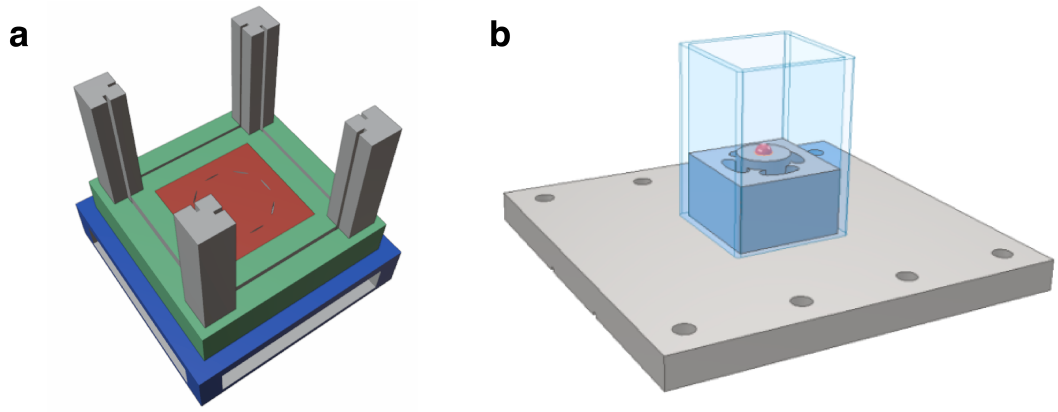

Figure 2.5: **(a)** First design of the dewetting device. The working liquid is injected from the bottom into a cylindrical reservoir, from which it flows through the drainage channels (holes on the red cap) and comes into contact with a droplet (not shown) positioned at the centre. Grooves on the pillars (grey) and on the base (green) are used to secure transparent walls (not shown). **(b)** Second design of device, fabricated in aluminium with a capped cubic glass tube serving as windows. The working liquid is injected from below and accumulates in a cubic reservoir before rising to the upper stage through four surrounding grooves. A droplet (orange) is deposited on the stage, which is elevated above the top of the reservoir.

The initial idea for the first design is to construct a working-fluid injection system from beneath, allowing the liquid to accumulate in a drain-like reservoir. As shown in Fig. 2.5a, this reservoir is sealed with a cap containing a circular array of holes, with the target droplet for removal deposited at the centre of the cap. To allow visualisation, four pillars are incorporated to hold transparent windows attached to the base. The device is fabricated by 3D printing with a hydrophilic polymer filament, producing a structure of approximately 10 cm in size. After fabrication, several issues with this design become evident. First, the resolution of the 3D

printer is 1 mm, which made the prototype insufficiently watertight. The fact that the device is made of polymer also created cleaning difficulties: droplet residue can be trapped between the printing fibres, while common cleaning solvents such as acetone or isopropanol caused swelling and damage to the device. Second, as the working fluid is delivered through holes on the cap to interact directly with the droplet positioned at the same level, perfectly uniform flow is required. Although the holes are arranged symmetrically around the droplet, this uniformity could not be achieved due to surface roughness introduced by the printing pattern. The working fluid therefore flows unevenly along the patterned surface and contacts the droplet in a non-uniform manner. Finally, the overall dimensions of the device are too large for a single-droplet system, making it difficult to capture both the droplet and the working fluid–air interface in focus simultaneously during visualisation.

Learning from this first attempt, the design is revised to improve sealing, reduce overall dimensions, optimise liquid–droplet interactions, and enhance visualisation. The second design, employed in Chapter 5, is a 25 mm cubic aluminium device as shown in Fig. 2.5b. Aluminium is chosen for its surface hydrophilicity, mechanical robustness, and chemical resistance, allowing the working fluid to wet the device uniformly and enabling reliable cleaning protocols. As in the original design, the working fluid accumulates in a reservoir, but the drainage system is simplified to four larger grooves, ensuring more consistent flow. The droplet is deposited on a central stage elevated above the grooves, so that the rising fluid first reaches the stage edge before making uniform contact with the droplet. This configuration also improves optical focus, as the droplet, the solid interface, and the liquid–air interface lie approximately within the same focal plane and can therefore be imaged simultaneously. For the transparent windows, sections of cubic glass tubing (4 cm long) are cut and capped onto the device using rubber adhesive. The combination of aluminium and glass facilitates cleaning, as both materials are resistant to solvents such as acetone and isopropanol, and can also be treated with plasma oxidation. With this improved design, droplet removal experiments are carried out as described in Chapter 5.

2.3.2 Substrate materials

The improved device is employed to investigate capillary lifting of droplets from a range of commercially available surfaces. The choice of substrates is guided by the aim of evaluating capillary lifting as a practical cleaning method for real-world contaminants while using minimal resources. The selected materials include polytetrafluoroethylene (PTFE), commonly used in coatings and medical devices; poly(methyl methacrylate) (PMMA), widely applied in optical panels and dental devices; glass, serving both as a hydrophilic reference surface and as a widely used industrial material; polycarbonate (PC), frequently employed in automotive components and construction; and stainless steel, a standard material in process engineering. These materials are ubiquitous in real-world cleaning scenarios and cover a broad range of surface energies. It should be noted that the substrates are tested in their commercial form, meaning that surface treatments and polishing (if present) influence their roughness and surface chemistry. As a result, local pinning points and hysteresis can occasionally be observed as the contact line advances or recedes. To mitigate this effect, each measurement is repeated on multiple samples within each substrate category, and reproducible trends are obtained. The overall behaviour can therefore be reliably compared with theoretical predictions. Achieving an idealised system would require single-crystalline, atomically smooth surfaces to minimise pinning and heterogeneity, but such conditions are beyond the scope of this study, which focuses instead on accessible, practically relevant materials.

2.4 Capillary bridge experimental stage

The capillary bridge study presented in Chapter 4 is a joint work with Sarah Goodband, where we investigate the geometry and force response of liquid bridges formed between two solid plates during compression and stretching. The experiments are enabled by a custom-built setup designed and constructed by Goodband (details in [17]). A brief description of the setup is provided here to give context for the results discussed later in this thesis.

As shown in Fig. 2.6, a liquid droplet is placed between two solid substrates,

referred to as the top and bottom plates. The top plate is mounted on a highly sensitive force sensor capable of measuring forces with nanonewton resolution. The bottom plate is fixed to a motorised stage that translates vertically to impose controlled compression and extension of the droplet bridge. The evolution of the bridge is recorded using a dual-camera imaging system. A digital camera equipped with a high-resolution lens captures the geometry of the bridge from the front view, while a second camera provides complementary side-view observations. This arrangement enables simultaneous quantification of the bridge morphology and the associated capillary forces throughout the compression–extension cycle.

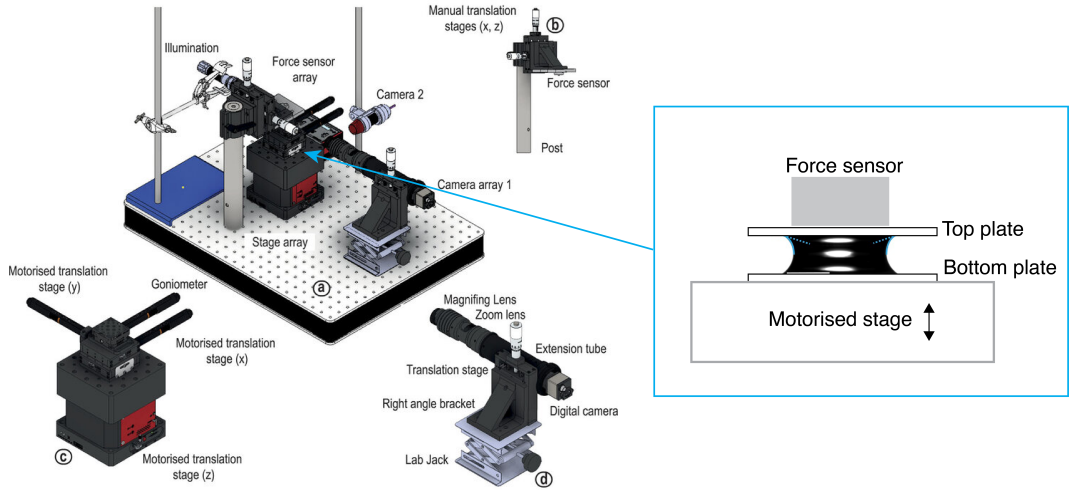

Figure 2.6: Experimental setup for study on capillary bridge between two solid substrates during compression-extension cycles, allowing force measurements and imaging. Figure adapted from [17].

2.5 Surface Evolver

Throughout this thesis, the experiments are conducted at sufficiently slow velocities to maintain near-equilibrium conditions, enabling the system dynamics to be approximated as quasi-static. This experimental approach is complemented by computational modelling using Surface Evolver [1]. This method is well suited for capturing equilibrium geometries, as it minimises the total system energy while accounting for contributions from surface tension, Laplace pressure, gravitational forces, prescribed contact angles, volume constraints, elastic energies, and other user-defined terms.

At the same time, it imposes important limitations on the scope of the simulations presented here. Specifically, dynamic processes such as energy dissipation, viscous flow, and viscoelastic stresses cannot be readily incorporated within this quasi-static approximation.

2.5.1 Principle of Surface Evolver

Surface Evolver [1] is an interactive program designed for the study of surfaces and interfaces through numerical energy minimisation. In a typical workflow, the user specifies an initial configuration consisting of vertices, edges, facets and bodies, together with constraints and an energy functional that govern the subsequent evolution. The surfaces are discretised into triangulated meshes, which can be adaptively refined to improve resolution and accuracy. Mesh uniformity is maintained through procedures that redistribute vertices, equalise edge lengths, and smooth regions of high curvature, thereby avoiding excessively distorted elements and ensuring well-defined contact lines.

The program employs a gradient-descent algorithm to relax the system towards a minimum-energy state. The total energy may include contributions from surface tension, gravitational potential, elasticity, pressure, and additional user-defined terms. Surface Evolver can accommodate a wide range of constraints, such as fixed volumes, imposed pressures, gravitational energy, and integral conditions applied along boundaries or surfaces. This flexibility makes the software practically well suited for simulating complex surface morphologies and capillary phenomena under controlled physical constraints.

Initialisation

To set up a system in Surface Evolver from scratch, we begin by defining basic geometric elements that constitute the surfaces and interfaces. First, we specify vertices, each assigned an ID number and positioned within the simulation domain using Cartesian coordinates (x,y,z). Next, we define edges as directed connections between vertex pairs, with orientation specified from the initial vertex to the terminal vertex. Connected edges are then assembled into facets, whose normal directions are

determined by applying the right-hand rule to the sequence of input edges. Finally, we define bodies as three-dimensional regions enclosed by oriented facets. To ensure correct topological assignment, the facets of each body must be oriented such that their normal vectors point inward toward the body's interior. As an illustrative example, I show the initialisation of a liquid bridge between two parallel solid plates in Fig. 2.7. The droplet is initially configured as a cubic body with prescribed volume, establishing distinct interfaces between the droplet-gas, droplet-plate, and plate-gas interfaces.

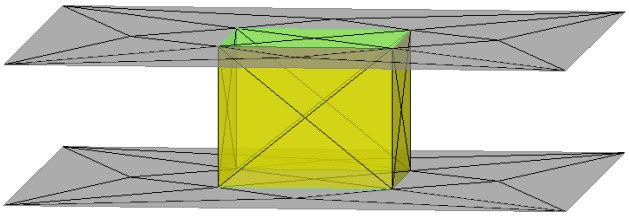

Figure 2.7: Initialisation of a droplet capillary bridge between two plates in Surface Evolver, with the droplet–gas, droplet–plate, and plate–gas interfaces shown in yellow, green, and grey, respectively.

Constraints

During system setup, we impose specific constraints that reflect the physical requirements of the problem. These constraints range from simple geometric restrictions, such as fixing vertex positions, to complex mathematically defined conditions for structured solid geometries. In the system illustrated in Fig. 2.7, vertices and edges defining the plates are fixed to represent their rigid and immobile nature. Contact vertices where the droplet meets the plates are restricted to lie within the z-planes of the plate surfaces, ensuring that physical contact is maintained throughout the evolution process. Constraints are particularly crucial in this thesis, as they also enable controlled motion of specific system components. For instance, the nanoparticle withdrawal described in Chapter 3 and the plate separation changes in Chapter 4 are implemented through parametric modifications within constraint functions. This approach allows the system to advance through incremental steps, with each converged equilibrium configuration serving as the initial condition for the subsequent step, ensuring stable and physically consistent evolution.

The droplet body can be defined using either volume constraints or pressure constraints. In this thesis, volume constraints are primarily employed, as they reflect the fixed liquid volume in the experimental conditions. The resulting Laplace pressure counterbalances surface tension forces that would otherwise drive surface shrinkage. Surface Evolver calculates this internal pressure automatically as part of the equilibrium solution, providing both the interface geometry and the associated pressure field. These computational outputs are subsequently utilised for theoretical force derivations, as demonstrated in Chapter 4.

Mesh refinement and adjustment

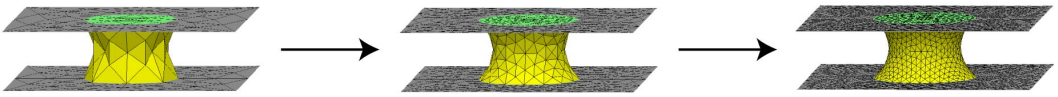

Figure 2.8: A droplet capillary bridge between two plates, evolving through iterative steps with mesh refinement and adjustment applied alongside.

In Surface Evolver, all surfaces and interfaces are discretised as simplicial complexes, specifically, unions of triangular elements. During the iterative search for minimum energy configurations, these triangular elements can become geometrically distorted: they may lose uniform orientation, develop irregular spatial distributions, or become oversized relative to regions of high curvature. Consequently, mesh refinement procedures are performed concurrently with the energy minimisation process. As shown in Fig. 2.8, simulations typically begin with coarse mesh initialisation, allowing rapid relaxation from simplified starting geometries toward appropriate liquid interface configurations. Refinement is subsequently introduced through systematic triangle subdivision of the original triangulation, thereby increasing spatial resolution. Simultaneously, mesh adjustments are employed to maintain uniform element distribution and orientation quality. Typical methods used are: **Vertex averaging**, which repositions vertices as the area-weighted average of adjacent facet centroids; **Equiangulation**, which improves element quality by optimising quadrilateral diagonal orientations to achieve more equiangular triangles; **Weeding**, which eliminates small triangles below prescribed size thresholds; and **Edge subdivision**, which splits edges that exceed specified length criteria. This combination of refinement

and adjustment ensures that interfaces remain symmetric and uniform throughout multiple iterations while accurately capturing system geometric details with high resolution.

Energy terms

Surface Evolver operates by minimising the total energy according to prescribed formulae corresponding to the investigated system. The main energy components used in this thesis are listed below.

Surface tension energy. Evolver calculates surface tension energy as the product of interface area and corresponding interfacial tension values:

$$E_s = \sum_i \gamma_i A_i \tag{2.1}$$

where γ_i is the surface tension of the facet i, A_i is the corresponding surface area, and the summation extends over all facets in the system. In practical implementation such as Fig. 2.7, the plate–gas and droplet–gas interfacial tensions γ_{sg} and γ_{dg} are set as 1. The droplet–solid interfacial tension γ_{ds} is then obtained from Young's equation: $\gamma_{ds} = 1 - 1 \times \cos\theta$, where θ is the contact angle. For complex multi-interface systems, additional experimentally measured interfacial tensions are incorporated with normalisation relative to a reference interfacial tension value. This normalisation approach maintains input parameters near 1, which is preferred in Surface Evolver's numerical stability. Since volume constraints are typically applied, Surface Evolver employs Lagrange multipliers to enforce these constraints. Physically, these multipliers correspond to Laplace pressure differences across curved interfaces. Therefore, the energetic contribution of Laplace pressure is inherently incorporated through the combined implementation of surface tension and volume constraint terms.

Gravitational energy. Gravitational potential energy is particularly important in Chapter 4 and Chapter 5, where capillary length scales are comparable to droplet dimensions, necessitating consideration of gravitational effects alongside

surface tension forces:

$$E_g = g \sum_k \int_{V_k} \rho_k z dV_k \tag{2.2}$$

where g is the gravitational acceleration constant, z is the vertical coordinate, ρ_k is the density of fluid k, and V_k is its volume. In the simulations, the gravitational constant was set to reproduce the Bond number measured experimentally, as detailed in Section 2.6.

Named quantity energies. Surface Evolver provides built-in functional methods for calculating additional energy contributions. In this thesis, an example is the introduction of line tension in Chapter 3 through edge integral implementation with prescribed line tension parameters obtained from literature values. Specifically, I use the method edge scalar integral, which evaluates the integral of a scalar function over the length of the assigned three-phase contact lines:

$$E_l = \int \tau dl \tag{2.3}$$

where τ is the line tension and l is the contact line length. Named methods like this enable straightforward introduction and computation of additional energetic contributions, while Surface Evolver also supports fully user-defined energy functions beyond the built-in options.

2.5.2 Applications in interfacial studies

Since its development, Surface Evolver has been widely employed in studies of foams, liquid interfaces, adhesion, and wetting phenomena. It provides a flexible and efficient framework for modelling surface energy systems, combining built-in methods with the ability to customise calculations for specific physical requirements. Notable applications include the reconstruction of pressure and energy distributions in foams [18], analysis of capillary bridges between fibres [19], and modelling of liquid ganglia in three-dimensional porous media [20]. These examples highlight the quasi-static character of the systems that can be addressed, in which multiple interfaces evolve toward equilibrium through energy minimisation. An additional advantage of the software is the straightforward implementation of different levels of constraints,

which can be prescribed directly through built-in methods. Figure 2.9 illustrates several representative cases: a liquid droplet on a solid rod, a cluster of six bubbles with four arranged in a ring around two central bubbles, and the withdrawal of a cylindrical rod from a liquid–air interface.

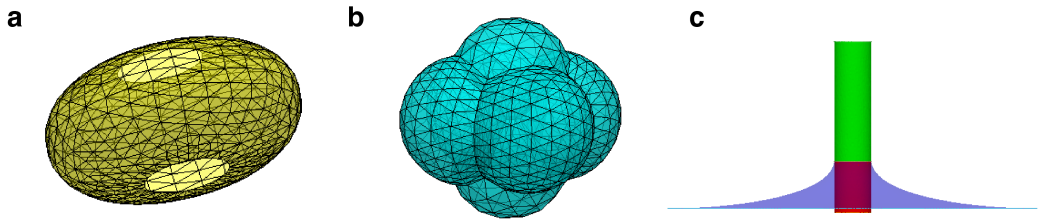

Figure 2.9: Surface Evolver applications examples: **(a)** A liquid droplet surrounding a rod (rod not shown) [21] **(b)** A cluster of six bubbles, with four arranged around the sides and two located in the centre [21]. **(c)** A cylindrical rod detaching from a liquid–air interface. Panel (c) is shown without mesh edges for clarity, since the high-resolution modelling results in an excessively dense triangulation.

2.5.3 Applications in this thesis

In this thesis, Surface Evolver is employed for three distinct applications, each presented in the results chapters.

Capillary adhesion: Surface Evolver is used to study the adhesion force profile of a nanoparticle being pulled from a liquid interface, examining systems with varying geometries and surface chemistry (see Chapter 3). A sample script can be found in the supplementary information of [22].

Capillary bridging: The software is applied to investigate the geometry and force response of liquid bridges in both binary and ternary fluid systems, with particular focus on capillary bridges formed between solid substrates and between liquid-infused surfaces (see Chapter 4). A sample script can be accessed in the Durham Research Repository at doi:10.15128/r26m311p40q.

Capillary-driven removal: Simulations are performed to model dewetting systems in which a droplet is lifted by an immiscible liquid. The analysis focuses on interfacial phenomena and the evolution of droplet morphology during the lifting process (see Chapter 5). A sample script can be accessed in the Durham Research Repository at doi:10.15128/r3f1881k890.

In all studies, the movement of solid or liquid components is implemented incrementally in small discrete steps to maintain the quasi-static approximation and ensure smooth evolution of the interfaces. Specifically, the step size is chosen relative to the characteristic scale of each system. In Chapter 3, the displacement increment is $\sim 1\%$ of the tip height. In Chapter 4, the height increment is $\sim 1\%$ of the total separation range between the maximum and minimum plate positions. For capillary-driven removal (Chapter 5), volume-controlled increments are used, with a typical step size of $\Delta V \approx 10$, reduced to $\Delta V \approx 1$ near detachment and rupture points to ensure accurate resolution of these transitions. Tests with smaller step sizes confirm that the computed forces and interface geometries remain unchanged within numerical resolution, indicating that the results are independent of the chosen increments and that quasi-static conditions are satisfied.

After each step, convergence is assessed using an energy-based criterion, with iterations terminated when the percentage change in total energy between successive steps falls below 0.0005%. Computed forces remain stable at this threshold. Tests with looser tolerances show that deviations become noticeable above approximately 0.003%, supporting the choice of convergence criterion.

The simulations are performed using a continuation approach, where each converged configuration serves as the initial condition for the subsequent step. This procedure is intended to follow physically relevant metastable branches, rather than to identify global energy minima. To assess robustness, additional tests were performed using alternative initial configurations, mesh refinements, and the `jiggle` operation in Surface Evolver to perturb the interface. These variations produced consistent force responses and interfacial geometries, with no significant differences observed within the parameter ranges considered.

With this convergence criterion in place, these models provide a fundamental framework for predicting capillary behaviours in experimentally challenging scenarios. Furthermore, the computed energy and pressure data from the simulations are used to support theoretical derivations and to validate experimental observations.

2.6 Integration of simulations and experiments

A critical aspect of the methodology is the integration of experimental and computational approaches, which is essential for obtaining the complete set of results presented in this thesis. First, the simulations are designed so that the relative dimensions of the model closely match those of the experimental setup. Characteristic size ratios of droplets and fluid domains are kept as consistent as possible across the two systems. This strategy ensures direct comparability while preventing disproportionately large interfaces from dominating the results. Second, during experiments, the velocity of imposed changes is kept sufficiently low to maintain quasi-static conditions. Control tests performed across a range of velocities confirm that in the lower regime, the results converge, demonstrating that dynamic effects are negligible. This validation allows meaningful comparison with Surface Evolver simulations, which inherently assume quasi-static energy minimisation. Finally, care is taken to reproduce the experimental boundaries within the simulations. For example, in the capillary adhesion study, the simulated liquid interfaces are defined to be sufficiently extended so that, at a distance from the particle, the interface is flat and horizontal, replicating the experimental environment. In practice, the interface edge is fixed at the domain boundaries to represent a flat far-field interface. The domain size is defined by the ratio of the initial particle–interface contact radius to the interface half-width, which is set to ~ 35. Sensitivity tests confirm that results remain unchanged for ratios $\gtrsim 25$, while noticeable deviations occur at ~ 10 due to boundary effects. For the capillary bridging study, boundary conditions are imposed through prescribed contact angles at solid or liquid interfaces, with plate dimensions chosen sufficiently large to avoid finite-size effects. For capillary-driven removal, the simulation domain matches the experimental geometry, where confinement ensures a flat liquid–air interface away from the droplet. These choices, together with consistency with experimental observations and measurements, ensure that boundary truncation does not influence the computed interfacial behaviour. These considerations are critical for constructing simulation models that reliably capture experimental behaviour, thereby establishing a robust framework in which experiments and computations complement and validate one another.

With this preparation in place, experimental measurements of surface tension, contact angles, density, and volume are incorporated into the simulation scripts. Where necessary, surface tension parameters are adjusted by up to 10% to avoid simulation artifacts such as interface crossover, while remaining within the bounds of experimental uncertainty. Gravitational effects are evaluated by considering the capillary length. In the capillary bridging and removal studies, the capillary length is comparable to the experimental droplet dimensions, thus gravity must be included. This is accomplished by calculating the experimental Bond number, which quantifies the relative importance of gravitational and surface tension forces, and using an appropriate gravitational constant in the simulations to match it. Specifically, this is performed by selecting a characteristic length L_{ref}, reference interfacial tension γ_{ref}, and density difference $\Delta\rho_{\mathrm{ref}}$ based on the system. For capillary bridging (Chapter 4), L_{ref} is taken as the average between the maximum and minimum plate separation, γ_{ref} as the droplet–gas interfacial tension, and $\Delta\rho_{\mathrm{ref}}$ as the density difference between the droplet and the surrounding gas phase. For capillary-driven removal (Chapter 5), $L_{\mathrm{ref}} = V^{1/3}$ (characteristic droplet size), γ_{ref} is taken as the droplet–liquid interfacial tension, and $\Delta\rho_{\mathrm{ref}}$ as the density difference between the droplet and the working liquid. Surface tensions and densities are normalised accordingly, and the dimensionless gravitational constant g_{sim} used in the simulations is determined by matching the experimental Bond number (Eq. 1.7), as reported in Table 1.1.

After obtaining the simulated results, the computed configurations are overlaid with experimental images to enable direct comparison of interfacial geometry and curvature. The simulation outputs for energy and pressure are further used to calculate forces and system energies, capturing the combined contributions of surface tension, Laplace pressure, etc. For nanoparticle adhesion (Chapter 3), the force is obtained from the derivative of the total energy with respect to displacement, evaluated from successive equilibrated configurations, with consistency verified against convergence and step-size sensitivity tests. For capillary bridging (Chapter 4), the force is evaluated from the pressure difference across the interface and the corresponding contact-line geometry, with the pressure directly obtained from the Sur-

face Evolver output and the force calculated using the capillary force equation (see Sections 4.3.3 and 4.3.4 for details). For capillary-driven removal (Chapter 5), the focus is on morphological transitions and detachment thresholds rather than continuous force curves; these are identified from changes in interface configuration and stability during the quasi-static evolution. In all cases, consistency between energy, pressure, and geometric measures is verified to ensure reliable interpretation of the simulation outputs. The resulting forces are then normalised to dimensionless form, allowing direct comparison with experimental measurements.

References

[1]K. A. Brakke, "The surface evolver", Experimental Mathematics **1**, 141–165 (1992).

[2]G. Binnig, C. F. Quate, and C. Gerber, "Atomic force microscope", Physical Review Letters **56**, 930–933 (1986).

[3]H.-J. Butt, B. Cappella, and M. Kappl, "Force measurements with the atomic force microscope: technique, interpretation and applications", Surface Science Reports **59**, 1–152 (2005).

[4]K. Sándor, *Nepenthes jardin des plantes - free photo on pixabay*, `https://pixabay.com/photos/nepenthes-jardin-des-plantes-861488/` (visited on 09/08/2025).

[5]DEZALB, *Nepenthe epiphyte carnivorous - free photo on pixabay*, `https://pixabay.com/photos/nepenthe-epiphyte-carnivorous-plant-1686965/` (visited on 09/08/2025).

[6]T.-S. Wong, S. H. Kang, S. K. Y. Tang, E. J. Smythe, B. D. Hatton, A. Grinthal, and J. Aizenberg, "Bioinspired self-repairing slippery surfaces with pressure-stable omniphobicity", Nature **477**, 443–447 (2011).

[7]A. Lafuma and D. Quéré, "Slippery pre-suffused surfaces", Europhysics Letters **96**, 56001 (2011).

[8]H. F. Bohn and W. Federle, "Insect aquaplaning: nepenthes pitcher plants capture prey with the peristome, a fully wettable water-lubricated anisotropic surface", Proceedings of the National Academy of Sciences of the United States of America **101**, 14138–14143 (2004).

[9]F. Box, C. Thorogood, and J. Hui Guan, "Guided droplet transport on synthetic slippery surfaces inspired by a pitcher plant", Journal of The Royal Society Interface **16**, 20190323 (2019).

[10]M. Villegas, Y. Zhang, N. Abu Jarad, L. Soleymani, and T. F. Didar, "Liquid-infused surfaces: a review of theory, design, and applications", ACS Nano **13**, 8517–8536 (2019).

[11]A. K. Epstein, T.-S. Wong, R. A. Belisle, E. M. Boggs, and J. Aizenberg, "Liquid-infused structured surfaces with exceptional anti-biofouling performance", Proceedings of the National Academy of Sciences **109**, 13182–13187 (2012).

[12]G. Wang and Z. Guo, "Liquid infused surfaces with anti-icing properties", Nanoscale **11**, 22615–22635 (2019).

[13]L. Xiao, J. Li, S. Mieszkin, A. Di Fino, A. S. Clare, M. E. Callow, J. A. Callow, M. Grunze, A. Rosenhahn, and P. A. Levkin, "Slippery liquid-infused porous surfaces showing marine antibiofouling properties", ACS Applied Materials & Interfaces **5**, 10074–10080 (2013).

[14]C. Wei, B. Jin, Q. Zhang, X. Zhan, and F. Chen, "Anti-icing performance of superwetting surfaces from icing-resistance to ice-phobic aspects: robust hydrophobic or slippery surfaces", Journal of Alloys and Compounds **765**, 721–730 (2018).

[15]S. J. Goodband, S. Armstrong, H. Kusumaatmaja, and K. Voïtchovsky, "Effect of ageing on the structure and properties of model liquid-infused surfaces", Langmuir **36**, 3461–3470 (2020).

[16]B. V. Orme, G. McHale, R. Ledesma-Aguilar, and G. G. Wells, "Droplet retention and shedding on slippery substrates", Langmuir **35**, 9146–9151 (2019).

[17]S. Goodband, H. Kusumaatmaja, and K. Voïtchovsky, "Development of a setup to characterize capillary liquid bridges between liquid infused surfaces", AIP Advances **12**, 015120 (2022).

[18]M. Mancini, E. M. Guène, J. Lambert, and R. Delannay, "Using surface evolver to measure pressures and energies of real 2d foams submitted to quasi-static deformations", Colloids and Surfaces A: Physicochemical and Engineering Aspects **468**, 193–200 (2015).

[19]X. Sun, H. J. Lee, S. Michielsen, and E. Wilusz, "Profile of capillary bridges between two vertically stacked cylindrical fibers under gravitational effect", Applied Surface Science **441**, 791–797 (2018).

[20]L. Zhang, G. Imani, H. Sun, D. Fan, S. Fu, Y. Yang, and J. Yao, "Energy-minimized mobilization of trapped non-aqueous phase liquids ganglia in three-dimensional biconical pores: insights from surface evolver simulations", Physics of Fluids **36**, 122121 (2024).

[21]K. A. Brakke, *Surface evolver examples*, Surface Evolver, `https://kenbrakke.com/evolver/examples/default.htm` (visited on 09/19/2025).

[22]K. Sun, Y. Gizaw, H. Kusumaatmaja, and K. Voïtchovsky, "Nanoparticle adhesion at liquid interfaces", Soft Matter **21**, 585–595 (2025).

Chapter 3

Nanoparticle adhesion at liquid interfaces

Particle adhesion at air-liquid and liquid-liquid interfaces is a ubiquitous phenomenon in nature and applications. When a particle contacts such an interface, a liquid meniscus forms around the particle, creating a capillary bridge that generates strong adhesion forces. For systems close to equilibrium, this adhesion phenomenon can be understood through classical thermodynamic principles, where the adhesion force arises from surface tensions and the Laplace pressure. In this chapter, we investigate this phenomenon down to nanoscale, examining the impact of surface chemistry and particle geometry on adhesion behaviour. We also discuss the possible contribution from line tension at the three-phase contact line, which becomes increasingly important at smaller length scales.

3.1 Abstract

Nanoparticle adhesion at liquid interfaces plays an important role in drug delivery, dust removal, the adsorption of aerosols, and controlled self-assembly. However, quantitative measurements of capillary interactions at the nanoscale are challenging, with most existing results at the micrometre to millimetre scale. In this chapter, we combine atomic force microscopy (AFM) and computational simulations to investigate the adhesion and removal of nanoparticles from liquid interfaces as a function of the particles' geometry and wettability (Fig. 3.1). Experimentally, AFM tips with controlled conical geometries are used to mimic the nano-asperities on natural nanoparticles interacting with silicone oil, a model liquid for many engineering applications including liquid-infused surfaces. Computationally, continuum modelling with the Surface Evolver software allows us to visualise the interface configuration and predict the expected force profile from energy minimisation. Quantitative agreement between the experimental measurements and the computational simulations validates the use of continuum thermodynamics concepts down to the nanoscale.

We demonstrate that the adhesion of the nanoparticles is primarily controlled by surface tension, with minimal line tension contribution. The particle geometry is the main factor affecting the length of the capillary bridge before rupture. Both the particle geometry and liquid contact angle determine the shape of the adhesion force profile upon removal of the particle from the interface. We further extend our simulations to explore more complex geometries, rationalising the results from experiments with imperfect AFM tips. Our results could help towards the design of smart interfaces, for example, able to attract or repel specific particles based on their shape and chemistry.

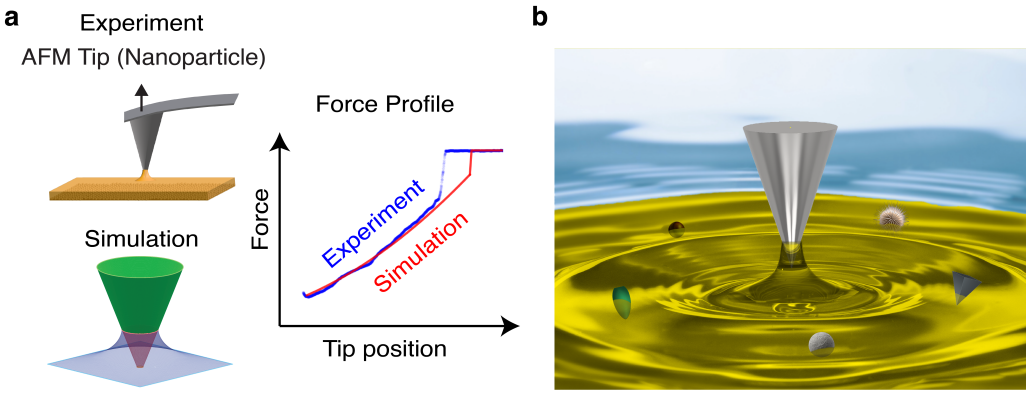

Figure 3.1: Nanoparticle adhesion at liquid interfaces is ubiquitous in nature and plays an important role in numerous technological applications. **(a)** A combination of atomic force microscopy measurements and modelling quantifies the force needed to remove nanoparticles from the interface as a function of their chemistry and shape. As featured on the journal cover of the publication of this chapter **(b)**. [1]

3.2 Introduction

Particles often get trapped at liquid interfaces. This naturally occurring process is important for fields as diverse as drug delivery [2], dust removal [3, 4], aerosol inhalation [5, 6], and controlled self-assembly [7, 8]. When a particle encounters a liquid interface, a meniscus forms between the particle and the surface of the liquid. Depending on the position of the particle, the meniscus can exert a capillary force that drives the particle to a position which minimises the associated interfacial free energy. The details of this process depend on the particle size and geometry, the liquid properties, and the interactions between the liquid and the particle. Experimental

methods for quantifying particle adhesion often involve detaching particles from interfaces while recording the necessary force to carry out the task. Initial studies have mainly focused on micron- to millimetre-sized particles with simple geometries to ensure ease of experimental tractability with standard optical microscopy, force measurements, and a relatively straightforward implementation of capillary theory. For example, Scheludko [9] and Huh [10] investigated the force necessary to pull millimetre-sized spheres from liquid–air interfaces. By comparing experiments and theoretical force calculations derived for spherical particles, they were able to infer the liquid interfacial tension. More recent works explored different surface functionalisation to vary the liquid contact angle and different particle geometries, including cylinders, ellipsoids, pyramids, and cubes. [11–15] There is also growing interest in exploring and manipulating the interplay between multiple particles at liquid interfaces, which can interact *via* a variety of forces, including electrostatic, depletion, and capillary-mediated forces. [16–18]

Despite these advances, there remains an open question whether capillary theory can be applied at the nanoscale, in particular on the role of line tension. For instance, it has often been argued that line tension can become important in describing wetting phenomena at the nanoscale. [19, 20] In contrast, Pakarinen [21] and Cappella [22] have suggested that capillary theory that only considers Laplace pressure and surface tension generally remains valid in the nanoscale systems they tested. In any case, both schools of thought highlight the necessity of comparing theoretical predictions with experimental data and investigating more complex geometries. Studying capillary phenomena at the nanoscale presents both a challenge and an opportunity: on the one hand experiments are difficult with the need to control particle geometry and the associated forces well beyond the capabilities of traditional optical approaches. On the other hand, the enhanced surface-to-volume ratio of nanoparticles offers new opportunities for interfacial targeting and related nanotechnological applications. [23, 24]

To tackle this issue, we employ an experimental setup based on atomic force microscopy (AFM), a technique that measures forces down to the piconewton range. Over the last decade, AFM has often been used for studies on capillary and interfa-

cial forces, typically attaching a microsphere or a droplet to the AFM tip to measure adhesion. [25–30] In contrast, akin to the work of Schellenberger [30], here we use the AFM tip itself as a model nanoparticle with a controlled conical shape. Conical nanoparticles are relevant for a wide range of medical and engineering applications and can serve as a model system for nanoscale asperities on naturally occurring particles. Examples include the cone-shaped HIV-1 capsids that penetrate nuclear pore complex [31]; conical Janus particles that serve as effective stabilisers for emulsions [32]; and pollen particles with nanoscale conical spikes that exhibit strong mucoadhesion [33].

For the liquid interface, we use liquid-infused surfaces (LIS) [34–37] with silicone oil as the lubricant. Aside from their potential for applications in technology and industry, LIS offer a good model for nanoparticle adsorption to viscous interfaces, for example in mucus and the natural biofilms in airways or in the lubricant film of moving mechanical parts. In the context of LIS, understanding the deposition and removal of nanoparticles (*e.g.*, dust and other contaminants) has important implications for their performance and longevity. First, particles often have irregular shapes [38, 39], emphasising the need to investigate non-spherical particles. Second, nanoparticles are directly detrimental to the performance of LIS, as in the context of self-cleaning surfaces [40] or anti-fouling surfaces [41], or because they can seed other processes, such as nucleation in anti-icing applications [42].

Practically, we use conical AFM tips with different cone angles, with the tip characteristics independently confirmed by electron microscopy. We also interface the silicone oil with both air and water to vary the effective particle wettability. To complement our AFM experiments, we harness computer simulations set up to mimic the experimental geometry, offering a quantitative comparison of the capillary effects. This is achieved with the software Surface Evolver [43], a continuum simulation method specialised in interfacial modelling. The simulations make it possible to quantify and visualise the intricacies of the nanoparticles' adhesion to the liquid interfaces and are used to systematically evaluate the impact of different interfacial and line energy contributions, as well as that of the particles' geometrical features.

3.3 Materials and methods

3.3.1 Fabrication of liquid-infused surfaces (LIS)

The LIS used in this study is composed of a porous solid base infused with a thin film of lubricant on top. The base is formed by layered hydrophobic nanoparticles, and the lubricant is silicone oil. [34, 35] The LIS substrates were fabricated as follows. First, rectangular glass slides (24×60 mm, Deckgläser, VMRTM, Lutterworth, UK) were sonicated in deionised water (18.2 MΩ·cm, Merck-Millipore, Hertfordshire, UK) for 30 min at 30 °C, followed by sonication in 5 wt% Decon 90 (Merck, Sigma-Aldrich, Gillingham, UK), and deionised water again. Subsequently, the slides were rinsed consecutively with acetone (Technical, Thermo Scientific^{TM}, Cambridge, UK) and isopropanol (99.5% for HPLC, Thermo Scientific^{TM}, Cambridge, UK), and then dried under nitrogen. Second, the porous structure was created on the slides using Glaco^{TM} (SOFT 99 Corp., Japan), a commercially available spray of hydrophobised silica nanoparticles. Glaco was sprayed across the cleaned glass slides and then dried for an hour at ambient temperature. This process was repeated until five layers of spray coating were applied to the slides. In the final step, a thin layer of silicone oil was infused on the porous substrate. Three drops (approx. 0.15 mL) of silicone oil (10 cSt at 25 °C, Merk, Sigma-Aldrich, Gillingham, UK) were deposited on a slide and subsequently spin-coated for 1 min at 1000 rpm, followed by 1 min at 500 rpm. LIS fabricated through this process retains an oil layer thickness of more than 3 μm in 16 days after fabrication [34], which is sufficient to prevent contact between the tip and the underlying porous structure during our experiments.

3.3.2 AFM setup and experimental strategy

Adhesion force curve measurements were conducted using two commercial AFMs: a Cypher ES (Oxford Instruments, USA) and a JPK NanoWizard 3 (Bruker, USA). Individual tips (Spark 70, Nu Nano Ltd, Bristol, UK; SNL-10, Bruker, USA) were used in each measurement. The Spark 70 tips are platinum-coated silicon tips, whereas the SNL-10 tips have silica surfaces in ambient conditions. All measurements used for quantification were conducted using Cypher ES AFM with Spark 70

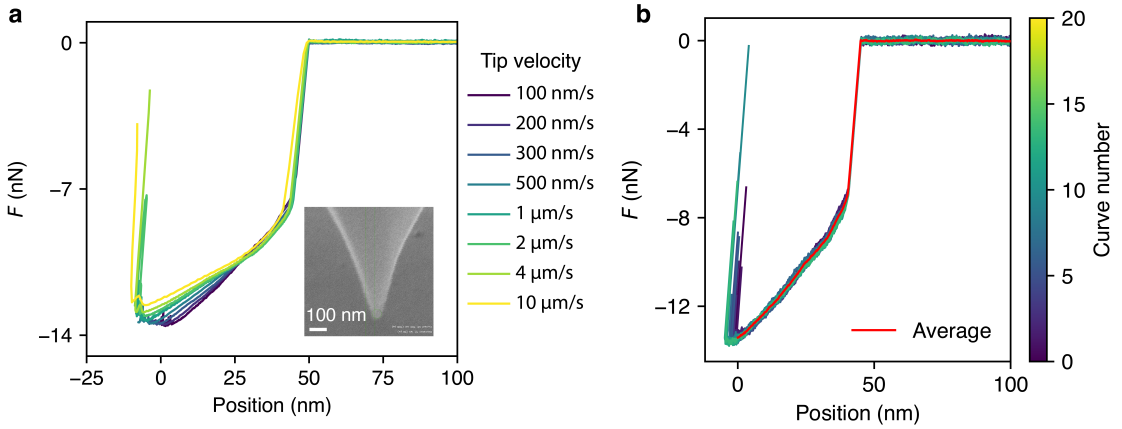

Figure 3.2: **(a)** Example force curve acquired at different velocities (100 nm/s – 10 µm/s) in otherwise identical conditions to access the dynamic effect. The curves were acquired with a same SPARK 70 tip (inset) and at a controlled temperature of 30.0 ± 0.1°C. As the velocity decreases, the deviation between force curves diminishes, indicating a reduced influence of dynamic effects. **(b)** Multiple repeats of experimental force curve measurements taken consecutively with the tip (the same Spark 70 tip used in (a)). The curves are aligned at the rupture point of the capillary bridge. The good overlap of the curves near the rupture point indicates full reproducibility of the measurements. The red line represents the average.

tips at a controlled temperature of 30 ± 0.1°C, except for the one involving imperfect geometry (see Fig. 3.16b), which was carried out using JPK NanoWizard 3 with an SNL-10 tip. Every Spark tip 70 was pre-characterised using electron microscopy, and we primarily selected tips with axisymmetric conical shapes to ensure reproducibility of the measurements across different setups. The tip cone angle near the apex varies from 10° to 38°, as measured from electron microscopy images using the ImageJ freeware. [44] Before each experiment, the tip was rinsed with isopropanol and then UV-treated for 5 minutes to gently remove organic contaminants from the manufacturing process and storage box. Each force spectroscopy measurement was repeated at least ten times and performed at a constant velocity of 100 nm/s. This velocity was chosen to minimise (and ideally remove) any dynamical effects dependent on tip motion and to allow comparison with the quasi-static simulation model, which assumes the system is always at equilibrium. In detail, considering the travel distance of the tip inside the liquid (< 100 nm) and the velocities experimentally accessible (< 20 μm/s), inertial or viscosity effects are likely negligible. Instead, possible velocity dependence may arise from the movement of the contact line along

the surface of the cantilever. Therefore, we tested different tips and systematically varied operating velocities as exemplified in Fig. 3.2a. The force profile depends on the tip velocity, but differences between curves become less important as the velocity decreases. Notably, the force profiles at velocities of 100 nm/s and 200 nm/s exhibited very similar characteristics, suggesting proximity to a quasi-static state (Fig. 3.2a). Consequently, we opted to systematically use the slowest velocity of 100 nm/s for comparison with the simulation results. Velocity-dependent effects can still not be excluded altogether, but the present strategy offers a good compromise between minimising them while allowing for velocities high enough to avoid significant motion drift. Successful comparison with the simulation results (Fig. 3.7 and 3.10) confirms the suitability of this compromise.

This experimental protocol yielded reproducible results, as the capillary bridge between the tip and the surface of the liquid was elongated and subsequently ruptured. For example, we repeated force spectroscopy measurements multiple times over an experiment with a given tip (Fig. 3.2b). The curves all overlap well except for slight shifts along the position axis (left-most part of the curves). This is due to the indentation depth of the tip in the liquid varying by up to a nanometre between consecutive measurements. This evolution is likely due to molecules of the liquid (oil) partly remaining at the surface of the tip after the rupture of the capillary bridge. Consistently, the changes occur immediately after initial contact with the liquid, but as the experiment progresses, all the force curves fully overlap. The average force curve (red line) serves as the displayed force profile for this particle adhesion. This method was employed in each measurement. After the desired measurements were completed, the spring constant and sensitivity were systematically characterised on a clean glass slide using the thermal method [45]. We obtained the cantilever spring constant for Spark 70 tips used in this study in the range 0.75–2.38 $\mathrm{N\,m^{-1}}$ (resonance frequency of 44–63 kHz in air). The SNL-10 tip used has a spring constant of 0.39 ± 0.05 $\mathrm{N\,m^{-1}}$ (resonance frequency 64.18 kHz in air).

3.3.3 Experimental determination of the liquid–solid contact angles

Due to the nano- to micro-scale size of the AFM tips and cantilevers, direct contact angle measurements are not feasible. Instead, we measured the contact angle by depositing a droplet of silicone oil on surfaces composed of the same material as the tip. A platinum film (99.99%, Sigma-Aldrich, Gillingham, UK) was used to replicate the tip surface of platinum coated tip Spark 70, while a silicon wafer (n-type, Inesto, Hampshire, UK) represented the silica surfaces of the silicon nitride SNL-10 tip. The contact angle measurements of silicone oil on representative tip surfaces were performed in both air and water to replicate the experimental conditions. In ambient air, the silicone oil exhibits nearly complete wetting (contact angle $\sim 0°$) on both the platinum film and silicon wafer (see Fig. 3.3a-d). For convenience, we typically assumed $\theta = 5°$ in the simulation model to directly compare with the experimental measurement in air (Fig. 3.7). This is justified because the force profile does not exhibit a significant difference when we carry out simulations from $\theta = 3°$ to $\theta = 10°$ (see Results Section 3.4.4). For measurements in water, the contact angle was determined by injecting a silicone oil droplet from below onto a platinum film immersed in a water bath. This upside-down configuration was necessary due to the density difference between silicone oil and water. The measured contact angle was $106.8 \pm 3.8°$, determined using the drop shape analysis LBADSA [46] fitting method in ImageJ [44] (Fig. 3.3e).

Notably, the platinum film used to represent the AFM tip surfaces has an intrinsic roughness significantly larger than that of the tip on the scale of the contact angle measurement. While addressing nanoscale roughness on the actual tip surfaces is not feasible, the measured contact angle on the platinum film can be corrected by the Wenzel model [47]:

$$\cos\theta_m = r \cdot \cos\theta_y \tag{3.1}$$

where θ_m is the measured contact angle, θ_y is the corrected Young's contact angle, and r is the roughness ratio, defined as the ratio between the actual surface area and

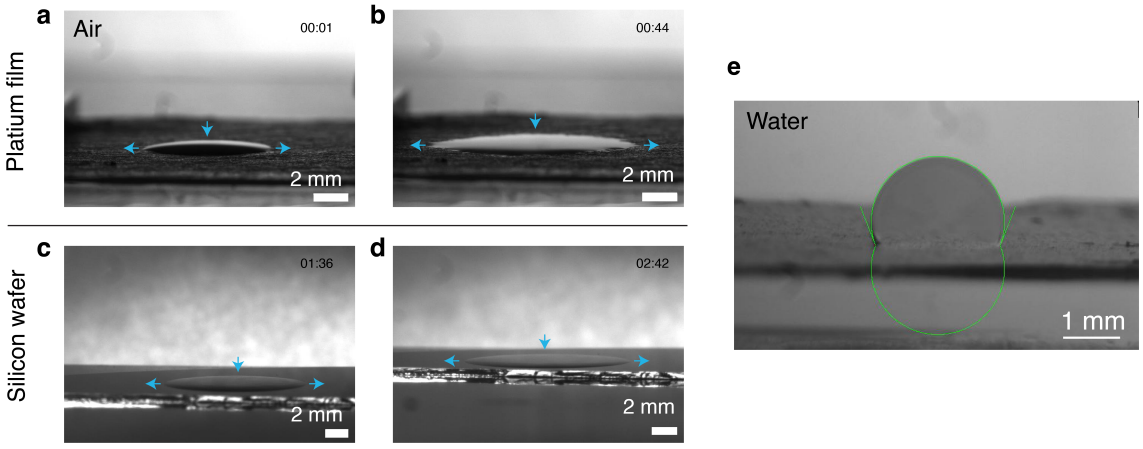

Figure 3.3: Spreading dynamics of silicone oil droplets on platinum film and silicon wafer in air show near-complete wetting $\theta \sim 0°$ at longer timescales. After deposition, the droplets spread uniformly across the surface **(a)** and **(c)**, and eventually spread towards the edges to fully wet the surfaces **(b)** and **(d)**. Arrows in the figures highlight the edges of the droplet for better visualisation. Time stamps (mm:ss) are shown in the top right corner of each figure. **(e)** Contact angle measurement of 10 cSt silicone oil on platinum film surrounded by ultrapure water. Due to the density difference, the measurement was performed by immersing a glass slide coated with platinum film in ultrapure water and injecting a drop of silicone oil from below. The image is flipped horizontally. The droplet was fitted by drop shape analysis LBADSA method [46] (green line), resulting in a measured contact angle of $\theta = 106.8 \pm 3.8°$ based on three repeat measurements.

the projected area ($r > 1$ for rough surfaces). The roughness ratio was determined by topography imaging using JPK NanoWizard V BioScience AFM (Bruker, USA), followed by triangulation of the measured surfaces to calculate the actual surface area, yielding $r = 1.015 \pm 0.006$. After correction, the contact angle in air remains $\theta \sim 0°$, while in water, the corrected contact angle is $\theta = 106.5 \pm 3.8°$. The contact angles do not show significant difference when considering surface roughness.

3.3.4 Surface Evolver

We used the Surface Evolver [43] to determine the energy and configuration of a system comprising a solid truncated cone as a function of the particle position from the liquid interface (Fig. 3.4). This mimics pulling the particle off the interface in the quasi-static limit. In Surface Evolver, each interface is triangulated. Subsequently, suitable interfacial and line tension energy contributions can be assigned to the facets and edges of the triangles.

In our simulations, the cone angle α is adjusted to mimic the AFM tips (cone

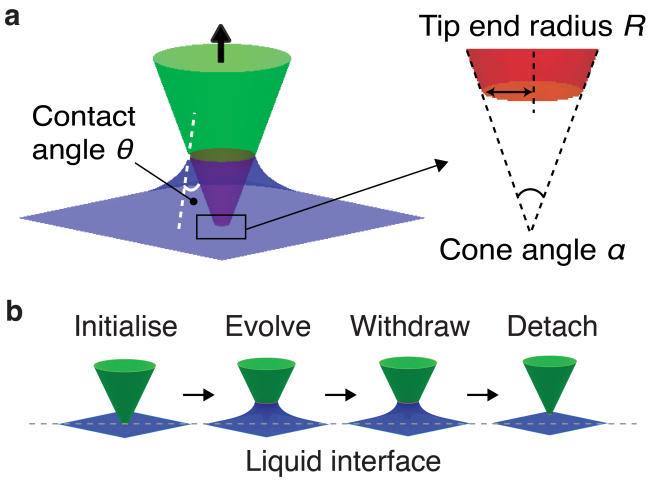

Figure 3.4: Surface Evolver simulation set up. **(a)** The desired particle geometry, here a truncated cone, is highlighted in green above the liquid, with the immersed part of the particle shown in red inside the liquid, and the liquid interface visible in blue. Particles with a cone angle in the range of $\alpha = 12$–$38°$ and a contact angle of $\theta = 3$ –$115°$ with the liquid were investigated. **(b)** The system was initialised with the tip apex immersed into the liquid, followed by relaxation of the interface and then progressive withdrawal of the tip away from the surface.

angle $\alpha = 12 - 38°$). The liquid contact angle on the particle surface was set in the range of $\theta = 3 - 115°$ to investigate the effect of liquid wettability on the particle (see diagram in Fig. 3.4a). The contact angle is related to the interfacial tensions via the well-known Young's equation, $\gamma_{SL} = \gamma_{SG} - \gamma_{LG}\cos\theta$, with γ_{SL}, γ_{SG} and γ_{LG} referring to the interfacial tensions (or energies) for the solid–liquid, solid–gas (or other surrounding fluid) and liquid–gas (or other surrounding fluid) interfaces, respectively. Since the capillary length of silicone oil is $\lambda = 1.48\,\text{mm}$ in air and $\lambda = 7.14\,\text{mm}$ in water ($\lambda = \sqrt{\frac{\gamma}{\Delta\rho\, g}}$, with $\gamma_{\text{oil–air}} = 20\,\text{mN}\,\text{m}^{-1}$, $\gamma_{\text{oil–water}} = 35\,\text{mN}\,\text{m}^{-1}$, $\rho_{\text{oil}} = 930\ \text{kg}\,\text{m}^{-3}$, $\rho_{\text{water}} = 1000\ \text{kg}\,\text{m}^{-3}$, and $g = 9.8\,\text{m}\,\text{s}^{-2}$), gravity can be neglected in the nanoscale measurement and hence ignored in the simulations. In several cases, we also included line tension energy as an extra free energy term associated with the three-phase contact line. We varied the line tension energy from $|\tau| = 1 \times 10^{-12}\,\text{N}$ to $1 \times 10^{-6}\,\text{N}$, encompassing a wide range of possible magnitudes reported in the literature. [20, 48–50]

The system was initiated with the tip already indented in the liquid. A Surface Evolver script providing a routine of energy minimisation iteration (using gradient descent) and mesh refinement was written to achieve an equilibrium state by evolving

the liquid to form a meniscus around the tip (Fig. 3.4b). The tip was then withdrawn in fine steps, with the energy of the system minimised at each tip position. For each step, the tip moves incrementally upwards along the z-direction by 1% of its own height. This allows for a gradual evolution of the system, ensuring that the mean curvature evolution of the liquid interface is accurately captured throughout the retraction process with sufficient data points. The liquid interface evolves and relaxes using gradient descent to minimise the total energy of the system, considering both surface tension and geometric constraints. The equilibrium configuration from the previous step serves as the initial condition for the energy minimisation, effectively mimicking the retraction process of the AFM experiment (Fig. 3.4b). An example Surface Evolver script is provided in the associated paper [1].

3.4 Results and discussion

3.4.1 AFM force spectroscopy measurement

AFM force spectroscopy measurements enable precise quantification of the adhesion force experienced by the tip as it enters and is subsequently removed from the interface. During a typical measurement, the AFM tip initially approaches the silicone oil surface from the air or pure water. Upon contact, a capillary meniscus forms around the tip, exerting a vertical capillary force. The tip is then withdrawn, and the meniscus elongates until it ruptures (Fig. 3.5a). The capillary force deflects the cantilever, allowing quantification of the force's magnitude and direction. Additionally, the precise position of the tip relative to the point of contact can be determined from the combined measurement of the cantilever base position and its deflection. [15, 26, 51] Here, since we aim for nanometre-level precision in our measurements, careful control over the indentation depth h at which the tip dips into the interface is needed (Fig. 3.5b, inset). This is challenging due to the fluid nature of the interface and the ability of the liquid to form a moving capillary bridge with the tip apex. To overcome this issue, we employ dynamic sensing strategy whereby the tip is externally oscillated close to the resonance frequency of the cantilever. As the tip contacts the liquid, the formation of a capillary bridge instantaneously quenches the

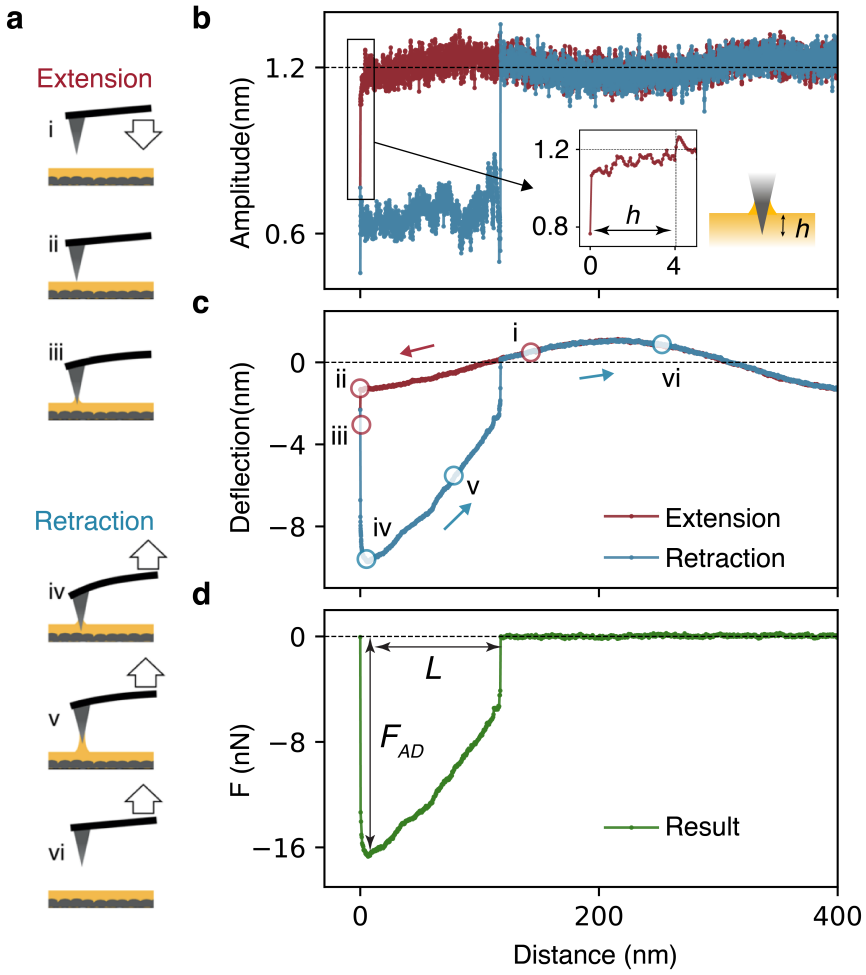

Figure 3.5: Example of a typical AFM force spectroscopy measurement. **(a)** Schematic representation of the measurement process: the cantilever and tip approach the surface of the liquid at a constant velocity (i) until contact is made (ii). This leads to the formation of a meniscus and a net force acting on the tip, inducing a static deflection on the cantilever (iii). The capillary force draws the tip deeper into the liquid as the cantilever is being retracted (iv). Upon retraction, the capillary meniscus is extended into a bridge (v), which eventually ruptures (vi), allowing the cantilever deflection to return to zero. **(b)** By superimposing a small oscillation on the cantilever's static deflection, the point of contact between the tip and the liquid can be accurately and dynamically detected, allowing for an immediate retraction trigger. An example of a measurement is shown for the amplitude acting as a trigger and the static deflection acquired simultaneously **(c)**, indicating the different stages of the measurement. From the static deflection, the capillary force can be readily obtained by multiplication with the spring constant of the cantilever **(d)**. L represents the maximum capillary bridge length, and F_{AD} represents the maximum adhesion force. In this example, the trigger point is reached once the amplitude has decreased to 60% of its value in air, leading to an indentation depth into the liquid of $h \sim 4$ nm.

free oscillating amplitude due to the significant difference in viscosity between the fluid media: the dynamic viscosity of air and water are respectively $\mu_{\mathrm{air}} = 0.018$ cP and $\mu_{\mathrm{water}} = 0.89$ cP at 25°C, at least an order of magnitude lower than that of the

LIS oil (μ_{oil} = 9.3 cP at 25°C). By setting a trigger on the cantilever amplitude, it is possible to control h with nanometre-level precision (Fig. 3.5b). The magnitude of the capillary force is then measured from the static (average) deflection of the cantilever, with the free oscillation amplitude kept small (< 1.2 nm, Fig. 3.5b) compared to static deflection (typically > 8 nm, Fig. 3.5c) to minimise possible crosstalk. For example, at the adhesion point (iv in Fig. 3.5c), the static cantilever deflection exceeds ∼10 nm, whereas the oscillation amplitude during retraction, the segment from which the force curve is extracted, is only on the order of ∼0.6 nm (Fig. 3.5b, blue trace). Thus, the oscillatory component is at least an order of magnitude smaller than the capillary deflection signal. Together with the smooth force profile observed during retraction, this indicates that the resonance-driven oscillation does not significantly affect the extracted force curve in the quasi-static regime. Depending on the coating and geometry of the cantilever, the deflection baseline may show small sinusoidal oscillations (Fig. 3.5c) due to optical interferences from the laser measuring the cantilever deflection. These can be removed by subtracting the retraction part of the curve from the extension part. In the resulting force curve (Fig. 3.5d), the maximum force encountered by the tip is defined as the particle's maximum adhesion force F_{AD}, representing the force required to overcome the capillary adhesion and detach the particle from the interface. The maximum capillary bridge length L is the capillary bridge length before rupture, as indicated by tip displacement from the interface (Fig. 3.5d). It is worth noting that the vertical feature observed at the very beginning of the force curve in Fig. 3.5c-d arises from the finite response time of the trigger and the turnaround between the approach and retraction phases. This transition happens too rapidly for precise control of the tip indentation and is not captured by our quasi-static computational model. This onset of the retraction has therefore been excluded from Fig. 3.7 and subsequent figures.

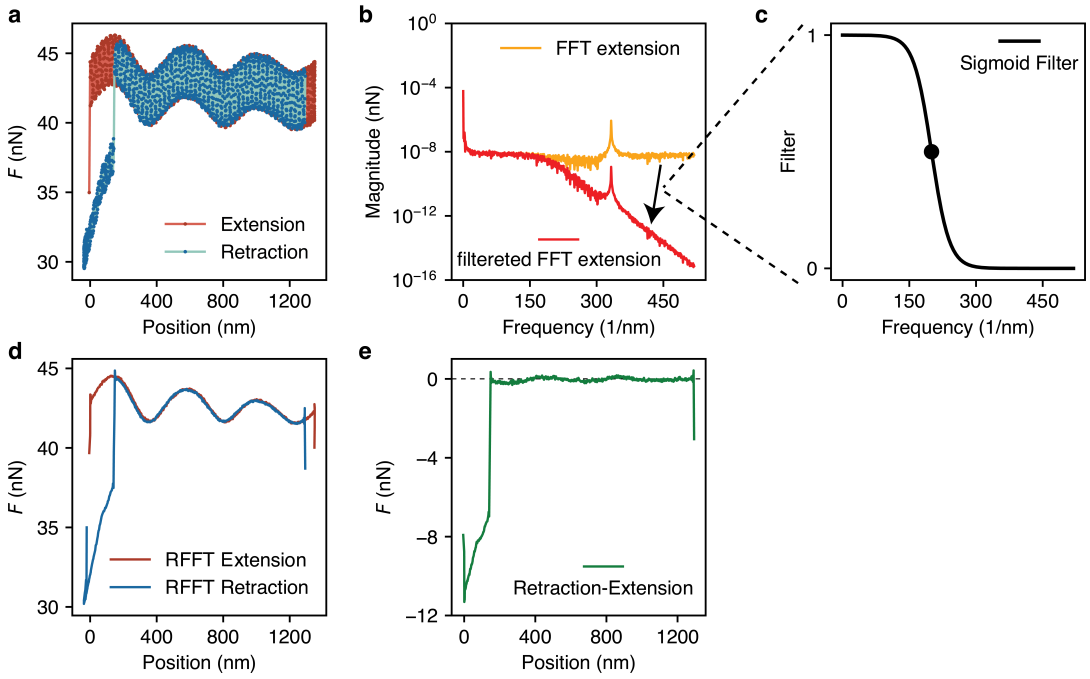

Figure 3.6: Example data processing for deflection curves with periodic noise. The original experimental data **(a)** exhibits the high-frequency oscillations of the cantilevers as well as low-frequency optical interferences. The Fourier Transform for the extension data **(b)** reveals a clear peak for the higher frequency oscillations that can be removed using a sigmoid low-pass filter **(c)**. Taking the Inverse Fourier Transform of the filtered data **(d)** shows that the high-frequency noise has indeed been removed. Further subtraction of the retraction curve from the extension curve **(e)** yields a suitable force profile for comparison with the simulations.

A typical procedure for processing raw AFM data is outlined below. The experimental data was processed by a Python script to obtain force versus tip-sample position results. Firstly, the raw deflection photodetector signal $P_{\mathrm{V}}(V)$ was converted to cantilever deflection $Z_{\mathrm{c}}(m)$: $Z_{\mathrm{c}} = P_{\mathrm{V}} \times$ Sensitivity. The piezo position Z_{p} was adjusted to the actual tip position relative to the sample surface through a bending correction, using $separation = Z_{\mathrm{p}} + Z_{\mathrm{c}}$. Finally, the force F was calculated from Hooke's law: $F = k \times Z_{\mathrm{c}}$, where k is the spring constant. In some cases (*e.g.* an experiment using JPK NanoWizard 3 with a Scout 70 Nu Nano tip, Fig. 3.6), the deflection signal requires further filtering to remove oscillations associated with dynamic sensing, particularly when using soft cantilevers with low resonance frequencies. To address this, a filtering approach based on the Fast Fourier Transform (FFT) was built into our analysis script: in a force curve containing high-frequency noise as seen in Fig. 3.6a, taking the extension part as an example, the force signal

was decomposed into constituent frequency components using the FFT (Fig. 3.6b, yellow line). A sigmoid filter function: $y = \frac{1}{1+\exp\left[-\beta(x_0-x)\right]}$ (Fig. 3.6c) was then applied to eliminate high-frequency noise. The parameters x_0 and β govern the midpoint and the decreasing rate of the function, respectively. Both parameters were tailored specifically to experimental values, ensuring appropriate filtering. The filtered low-frequency signal can then be restored to the original force data through the Inverse Fast Fourier Transform (IFFT) (Fig. 3.6d). In the final step, the low-frequency laser interference was removed by subtracting the retraction curve from the extension curve (Fig. 3.6e). These low-frequency oscillations arise from constructive interference between the laser reflection from the cantilever and light scattered by the sample surface. Overall, this protocol effectively processes force curves exhibiting both high-frequency noise and low-frequency interference, producing a clean set of data while preserving all characteristic features.

3.4.2 Comparing experimental results with computer simulations

To complement the AFM measurements, computer simulations were conducted with Surface Evolver [43]. The goal is to gain detailed insights into the nanoparticle detachment from the liquid interface. An exemplar result, presented in Fig. 3.7, shows the comparison for an axisymmetric cone-shaped tip (Spark 70) with a truncated radius of $R = 28 \pm 4$ nm and cone angle of $\alpha = 30 \pm 8°$, determined through electron microscopy. The contact angle between the liquid and the tip is taken as $\theta = 5°$ to represent the highly wetting behaviour of silicone oil on a platinum film (see Section 3.3.3). These experimental parameters are then imposed into the Surface Evolver simulations (see Section 3.3.4). The orange-shaded area in the simulation results corresponds to the uncertainty in the experimental cone angle measurements (Fig. 3.7a).

The simulations are conducted in the quasi-static limit. This is justified by the fact that experimentally, the tip is moved with a constant velocity of 100 nm/s on approach and retraction. This slow velocity aims to strike a compromise between keeping the system close to equilibrium while limiting thermal drift over the rel-

atively long travel distance (> 1 μm). Viscous forces are negligible compared to interfacial forces, as indicated by the small capillary numbers: $Ca = 4.65 \times 10^{-8}$ (oil–air) and $Ca = 2.66 \times 10^{-8}$ (oil–water).

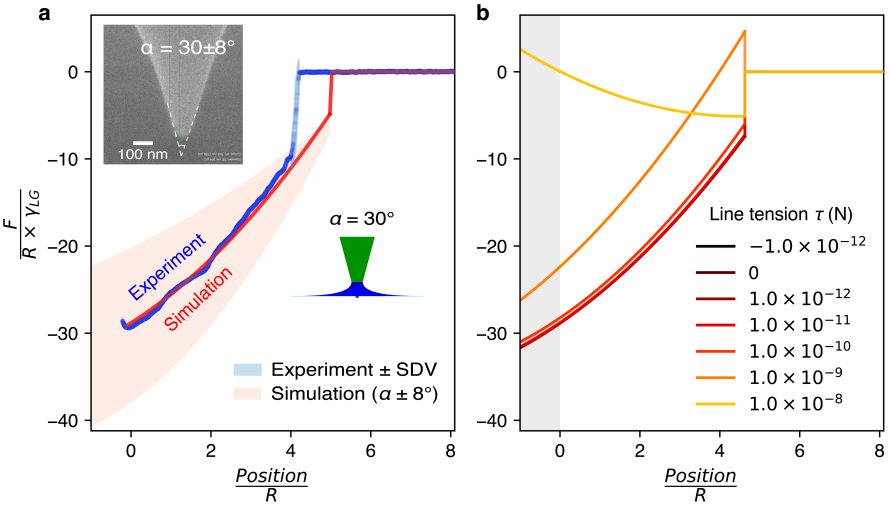

Figure 3.7: Quantitative comparison of simulations and experiments conducted with the same tip geometry. The simulations were first conducted without taking into consideration line tension **(a)**. An electron microscopy image of the tip is shown in inset, indicating a cone angle of $\alpha = 30 \pm 8°$ and an end radius of $R = 28 \pm 4$ nm. The liquid–air interface is taken as the reference point, indicating where the tip-liquid separation is zero. The x-axis (tip position relative to the liquid interface) is normalised by R, and the y-axis (measured force) by the product of $R \times \gamma_{\mathrm{LG}}$, rendering both axes unitless. Experimental measurements were repeated twenty times and subsequently averaged to minimise random fluctuations. The orange-shadowed area around the simulated curve indicates the maximum error based on the experimental cone angle uncertainty (8°). The contact angle between the liquid and the tip is $\theta = 5°$ in the simulation. **(b)** Further simulations are performed including the line tension τ, varying from $\tau = -1 \times 10^{-6}$ N to 1×10^{-6} N. The simulated force curves with $-1 \times 10^{-12} \leq \tau \leq 1 \times 10^{-10}$ N are indistinguishable and correctly reproduce the experimental results shown in (a). When $1 \times 10^{-9} \leq \tau \leq 1 \times 10^{-8}$ N, the line tension significantly influences the force profile which no longer reproduces the experimental results. For $\tau \leq -1 \times 10^{-11}$ N and $\tau \geq 1 \times 10^{-7}$ N (not shown), the simulated system becomes too unstable to reach a static state. Note that Position/R $= 0$ corresponds to the point where the tip apex meets the liquid interface when at rest. The shaded grey region represents the range where the tip end is immersed. Experimentally, the immersion depth is negligible compared to the length of the capillary bridge. Comparison with the simulations should therefore be taken outside the grey-shaded area.

As discussed in the caption of Fig. 3.7, comparison with quasi-static simulations is restricted to the retraction segment outside the grey-shaded region, where the interface evolves smoothly and the force varies continuously with displacement. Under these conditions, a close quantitative agreement between experiments and simulations can be obtained (Fig. 3.7). The experimental data is not as smooth as the

simulated curve, but this disparity can be explained by the nanoscale surface imperfections of the AFM tip. While the effect is minimised by our use of relatively low velocities (see Section 3.3.2 and Fig. 3.2a), local imperfections are still omnipresent on any polycrystalline surface such as the AFM tip, even if too small to be seen in the electron microscopy image.

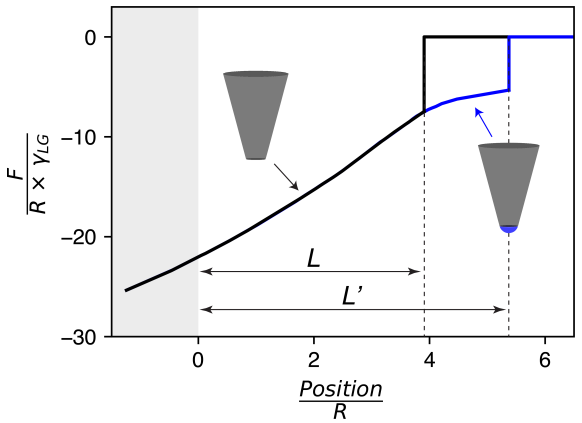

Figure 3.8: Simulated force profiles for different truncated tips. Inset: cartoon illustrations of the two conical tips: one with a smooth spherical end and the other with a sharp truncation. The maximum length of the capillary bridge before rupture is labelled as L' for the spherical-end cone and L for the sharp-truncated cone. These lengths are measured with position x = 0 being the point of contact between the tip end and the liquid interface. The simulations were initialised with the tip partially immersed in the liquid (grey-shaded area) and proceeded by evolving the interface between each step of tip withdrawal from the liquid's surface. The force profile of the sharp-truncated cone is shown in black, while that of the spherical-end cone is shown in blue. The two profiles overlap at positions where $\frac{\text{Position}}{R} < 3.9$. Both axes are normalised with end radius R and liquid-gas surface tension γ_{LG} to be unitless.

In addition, the tip apex differs from the ideal sharp truncation used in the simulations (Fig. 3.4), with the experimental tip often assumed to be pseudo-spherical. [52, 53] This discrepancy can be partially addressed by adjusting the simulated geometry, though variations in the precise shape of the apex can still lead to differences between experimental and simulated capillary bridge rupture. At the point of rupture, the capillary bridge is attached precisely to the apex region, which likely dominates the rupture process. Experimentally, controlling the shape of the tip apex is challenging, regardless of the degree of control over the cone angle. To reflect this situation, most simulations in this work employed a truncated conical tip. While a simplification, it reflects the finite size and inherent imperfections of the experimental apex. Beyond this, it offers an opportunity to investigate numerically

the impact of the truncation on the resulting force profile. For example, we set up two tips with identical overall cone shapes, but with either a sharp truncation or a smooth transition to a spherical end. Fig. 3.8 shows simulations run comparatively for these two geometries, referred to as 'sharp-truncated' (black line) and 'spherical-end' (blue line). Initially, when the three-phase contact line is on the conical section, both models exhibit the same profile. However, when the contact line reaches the end of the conical section, the behaviour diverges: for the sharp-truncated cone, the liquid detaches from the tip, and the capillary bridge ruptures. In contrast, for the spherical-end tip, the contact line continues to slide along the spherical part. Consequently, the capillary bridge ruptures at different positions, with the maximum capillary bridge length L' for the spherical-end cone greater than L for the sharp-truncated cone. This comparison suggests that the details of the particle truncation may be at the origin of the discrepancy in rupture point between experiments and simulations observed in Fig. 3.7.

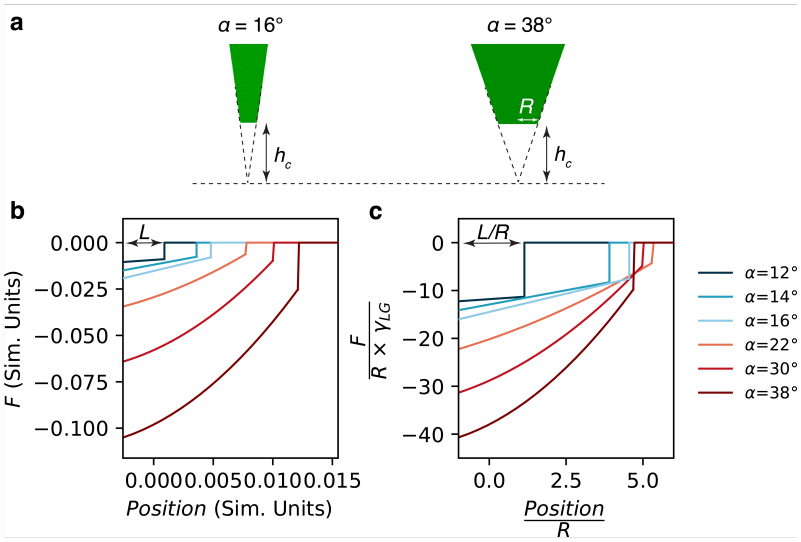

Figure 3.9: (a) Schematic illustration of narrow and wide cones used in the simulation model, where α represents the cone angle. Both cones were truncated at the same height, h_c, resulting in different end radii, R. **(b-c)** Simulation force profiles for cones with varying α: before normalisation (b) and after normalisation by end radius and surface tension (c). L denotes the capillary bridge length. L/R denotes the normalised capillary bridge length.

Aside from the details of truncation geometry, it is worth noting that the normalisation process used to compare directly the experimental and simulated curves affects the apparent non-monotonic dependence of the capillary bridge length L on

the cone angle α. The simulations employ cones truncated at the same height, resulting in different end radii, R, which are used as the characteristic length in the normalisation (Fig. 3.9a). In Fig. 3.9b, the raw simulation data (prior to normalisation) show that L increases monotonically with α. However, after normalisation (Fig. 3.9c, same as Fig. 3.10), L/R exhibits a non-monotonic behaviour due to the variation in end radius R, across cone angles. In addition, when considering L across both experimental and simulation contexts, variations in apex features can further contribute to differences in capillary bridge length L, as noted above. Taken together, these observations indicate that quantitative comparisons should focus on the retraction force profile rather than on the capillary bridge rupture, where nanoscale geometrical details dominate.

An important point of the simulated curve shown in Fig. 3.7a is that no line tension has been considered. The concept of line tension, first introduced by Gibbs as an additional free energy term at the three-phase contact line [54], can play an important role in surface and wetting phenomena. [19, 20] However, the magnitude and sign of line tension remain controversial to date, with the magnitude of theoretical and simulation values ranging from $|\tau_{\text{sim}}| = 1 \times 10^{-12}$ N to 1×10^{-10} N and experimental values from $|\tau_{\text{exp}}| = 1 \times 10^{-12}$ N to 1×10^{-6} N. [20, 48–50] Here, given the nanometre scale of the system, line tension could in principle play a role. We therefore conducted simulations for a range of line tension values in addition to the usual interfacial energy contributions. We explore line tensions in the range of $|\tau| = 1 \times 10^{-12}$ N to $|\tau| = 1 \times 10^{-6}$ N (Fig. 3.7b). The results show that for values in the range of $-1 \times 10^{-12} \leq \tau \leq 1 \times 10^{-10}$ N, the contribution of the line tension term is negligible in the simulations. In fact, this provides the bounds for the magnitude of a possible line tension contribution in our system. Outside these bounds, if $1 \times 10^{-9} \leq \tau \leq 1 \times 10^{-8}$ N, the simulation predictions are no longer able to reproduce our experimental observations. This suggests that no significant contribution from the line tension to the adhesion force profile is experimentally present in our system. Furthermore, when $\tau \leq -1 \times 10^{-11}$ N or $\tau \geq 1 \times 10^{-7}$ N, the simulations exhibit high fluctuations, making it difficult to reach a static state and reliable predictions. The associated results are hence not presented in Fig. 3.7b.

While negligible in the present system, line tension can play a significant role for nanoparticles at interfaces depending on its size. [20, 48–50] A simple criterion can be obtained from the ratio of τ/γ for a given interface, with line tension becoming significant for particles exhibiting a radius $R < \tau/\gamma$. [48] Here, using the upper estimate derived for τ and the measured air–oil and water–oil interfacial tensions yields a maximum value of $R \sim 5$ nm. This is below the size of our tip particles' end radii, whose apex are in the range of $R = 25$–31 nm. Using sharper tips with a truncated radius $\lesssim 5$ nm would require taking the line tension into consideration.

3.4.3 Impact of tip-particle cone geometry

Having established the suitability of our dual AFM-simulation method to investigate the detachment of nanoparticles from liquid interfaces, we now focus on the particle's shape. In practice, the number of parameters that can be controlled experimentally is limited, with this section investigating the impact of the cone angle α. We therefore selected two AFM tips with significantly different cone angles. The tips and cantilever are the same by design, but we selected on purpose outliers from the average commercial production, choosing those with cone angles of $\alpha = 30 \pm 8°$ (same data as in Fig. 3.7) and $\alpha = 14$–$21°$. For the simulations, we varied the tip cone angle from $\alpha = 12°$ to $\alpha = 38°$.

The experimental results are shown in Fig. 3.10a, demonstrating that the geometry of nanoparticles significantly influences their adhesion profile to the surface of the liquid. The sharper cone (smaller α) exhibits lower adhesion than the wider cone and the maximum capillary bridge length increases with α. Moreover, for the sharper cone, the adhesion force profile remains relatively constant during retraction until rupture of the capillary bridge. For the wider cone, the capillary force magnitude gradually decreases (becoming less negative in the figure) upon retraction until the bridge is ruptured and the tip is fully withdrawn from the liquid.

The simulations corroborate the experimental observations as α is systematically varied (Fig. 3.10b). We note that the non-monotonic evolution of the normalised maximum capillary bridge length L/R with α is due to the normalisation process enabling direct comparison of the simulations with the experiments; non-normalised

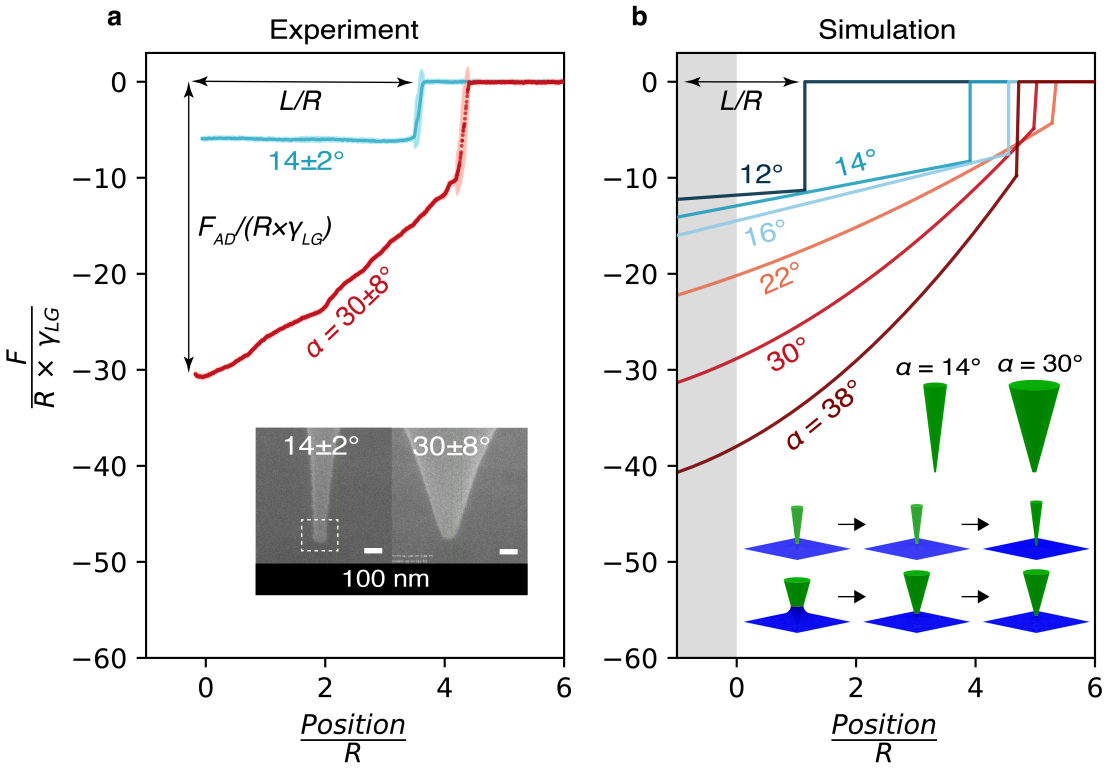

Figure 3.10: Effect of the cone angle on the adhesion force of the tip at the air–LIS interface. The experiments in **(a)** are conducted with platinum-coated tips exhibiting a cone angle of $\alpha = 30 \pm 8°$ and $\alpha = 14 \pm 2°$ (see electron microscopy images, with a slight reversal geometry at the apex highlighted by a dashline square). The simulations **(b)** are conducted with cone angle in the range of $\alpha = 12$–$38°$. The contact angle with the oil is set to be $\theta = 5°$, consistent with measurements on flat surfaces and results in contact angle discussion (see Methods Section 3.3.3 and Results Section 3.4.4). The inset shows simulation frames for cone angles of $\alpha = 14°$ and $\alpha = 30°$ during withdrawal from the liquid interface. All quantities have been normalised as in Fig. 3.7 to make them unitless. The grey-shaded area indicates the part of the curve with the tip apex below the liquid's surface. L/R represents the normalised maximum capillary bridge length, and $F_{\mathrm{AD}}/(R \times \gamma_{\mathrm{LG}})$ represents the normalised maximum adhesion force.

curves show a monotonic dependence as can be expected from the theory as aforementioned in Fig. 3.9. Both the normalised force profile $F/(R \times \gamma_{\mathrm{LG}})$ and the slope of the force increase with α. This is to be expected with wider cones presenting a larger, but height-dependent contact area with the liquid compared to sharper cones. Conversely, when the cone shape approaches that of a cylinder, the meniscus area hardly changes upon retraction, and the normalised force profile $F/(R \times \gamma_{\mathrm{LG}})$ varies little until the bridge ruptures. Interestingly, the experimental results indicate a cylinder-like behaviour already at a $\alpha \sim 14°$. This can be explained by the imperfect shape of the tip (Fig. 3.10a, inset), with the slight reversal of the cone

shape near the tip apex. The effect is likely subtle, and local variations in the tip-liquid contact angle could also be responsible for this effect, as explored in the next section.

3.4.4 Impact of the tip-liquid contact angle

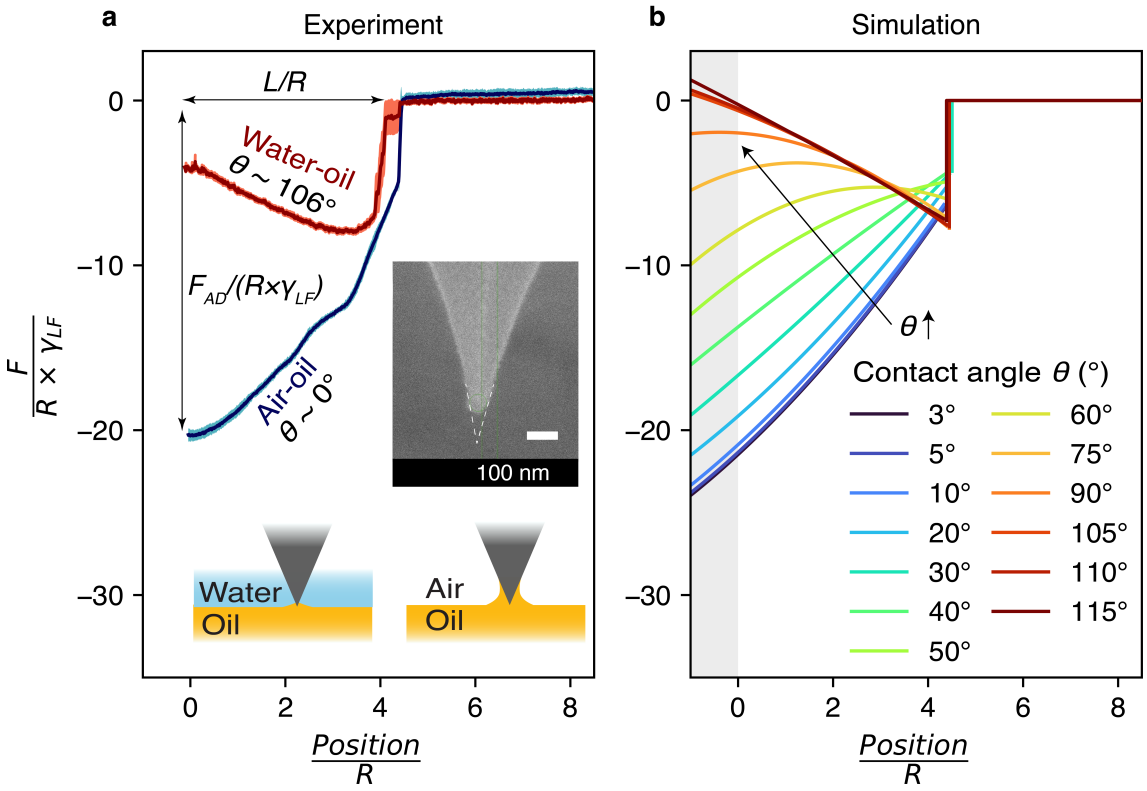

Figure 3.11: Impact of the contact angle θ between the liquid and the tip on the measured adhesion force profile. **(a)** Experimentally, two θ values are explored by varying the approach fluid in contact with the LIS: air and water (cartoons in inset). Position and force axes are normalised to be unitless as in the previous figures. The simulation results **(b)** are obtained by systematically varying θ with a conical tip of angle $\alpha = 26°$ to compare with the experimental result. The shaded grey area represents the region where the tip apex is below the surface of the oil. L/R represents the normalised maximum capillary bridge length, and $F_{\mathrm{AD}}/(R \times \gamma_{\mathrm{LG}})$ represents the normalised maximum adhesion force.

Aside from the shape of the particle tip, the contact angle θ formed by the liquid (here the oil) with the surface of the particle offers another crucial factor affecting adhesion at the interface. θ quantifies the liquid ability to wet the tip surface and hence influences the capillary force. To quantitatively explore this parameter, we used the same dual AFM-simulation approach: experimentally, systematically varying θ is challenging, but two values could be explored with the same tip by com-

paring curves obtained at the air–oil ($\theta \sim 0°$) and water–oil ($\theta \sim 106°$) interfaces (Fig. 3.11). From the electron microscopy image, the tip used for this set of experiments exhibits an average cone angle of $\alpha = 26 \pm 4°$, with simulations conducted imposing $\alpha = 26°$. It should be noted, however, that this conical tip is not perfectly axisymmetric (Fig. 3.12) with small variations in α visible, depending on the side of the tip observed. We believe these variations to be responsible for the imperfect match between the experimental results and the simulations. In the simulations we systematically varied the contact angle from $\theta = 3°$ to $\theta = 115°$, which captured well the range of possible experimental contact angles once measurement uncertainties are taken into account.

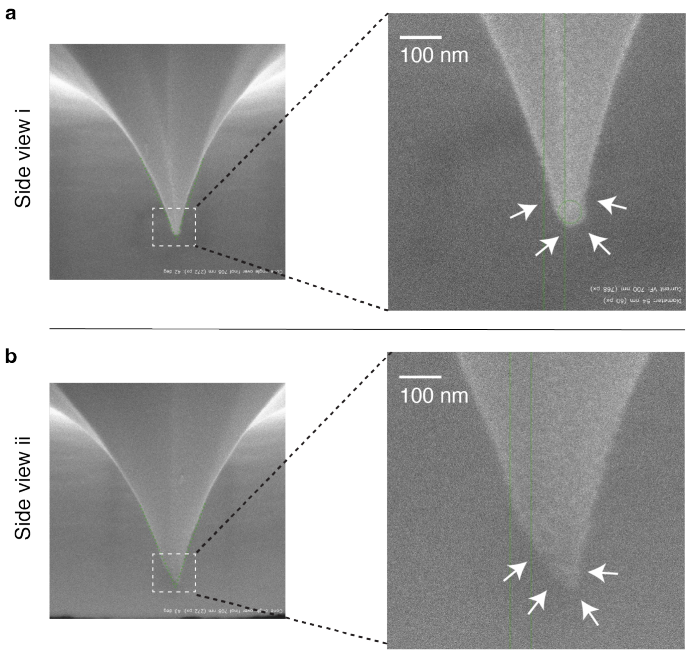

Figure 3.12: Electron microscopy images for the tip used for the air-oil and water-oil interface measurements (Fig. 3.11). Images taken with different side views illustrate a typical tip imperfection with geometrical variations between different viewpoints. **(a)** The tip is observed to be relatively symmetric with a slightly rounded shape at the apex from side view i. This view was used to measure the geometrical characteristics for Fig. 3.11 **(b)** The tip shows asymmetry from side view ii, with a noticeable cone angle change at the apex. Apex features are highlighted by white arrows to aid visualisation.

For the sake of clarity, we hereafter refer to oil as the liquid, and the air or water (tip approach medium) as the fluid. The measured force is normalised by liquid–fluid interfacial tension γ_{LF} and the tip apex radius R, where $\gamma_{\mathrm{LF}} = 20\,\mathrm{mN\,m^{-1}}$ for an oil–air interface and $\gamma_{\mathrm{LF}} = 35\,\mathrm{mN\,m^{-1}}$ for an oil–water interface. The results indicate

good agreement between simulation predictions and experimental observations, with a general trend of the magnitude of $F/(R \times \gamma_{\mathrm{LF}})$ decreasing (becoming less negative) with increasing θ – the intuitive fact that lower wettability benefits removal from the interface (Fig. 3.11). Comparing the force curves highlights the complexities as we vary the contact angle, with a reversal of the shape of the force profile depending on the specific value of θ.

During particle withdrawal, the solid-fluid interfacial area increases while the solid-liquid area decreases until reaching zero when the three-phase contact line reaches the tip apex end. The behaviour of the liquid-fluid interfacial area is more complex: it may either decrease or increase depending on the contact angle and the position of the contact line. The systematic simulation study in Fig. 3.11b reveals three main regimes based on the tendencies observed in the force profiles. To rationalise these behaviours, we analyse the corresponding changes in interfacial energy contributions and illustrate typical features in the three regimes using examples of $\theta = 30°$, $75°$ and $100°$ as shown in Fig. 3.13. The interfacial energy profile can be divided into two parts for analysis depending on whether the contact line (i) slides along the conical particle, or (ii) is pinned at the apex edge of the particle.

For $\theta \leq 53°$, the strong affinity of the liquid for the tip creates a large capillary meniscus, resulting in an instantaneous adhesion $F/(R \times \gamma_{\mathrm{LF}})$ when the tip 'touches' the surface of the liquid. Withdrawal of the tip away from the surface induces a monotonic decrease in the magnitude of the capillary force with a steeper gradient before detachment of the bridge (Fig. 3.11b). This behaviour is dominated by the sliding of the three-phase contact line along the conical particle before it reaches the tip apex. An example at $\theta = 30°$ illustrates the contributions of various interfacial energies (Fig. 3.13): strong wetting drives the formation of a pronounced meniscus, and during withdrawal the contact line slides upward along the cone, reducing solid–liquid and liquid–fluid energies while increasing solid–fluid energy. Once the contact line reaches the truncation edge of the conical tip, it becomes pinned, leading to a small increase in liquid–fluid energy over the final stages of withdrawal before the capillary bridge eventually ruptures.

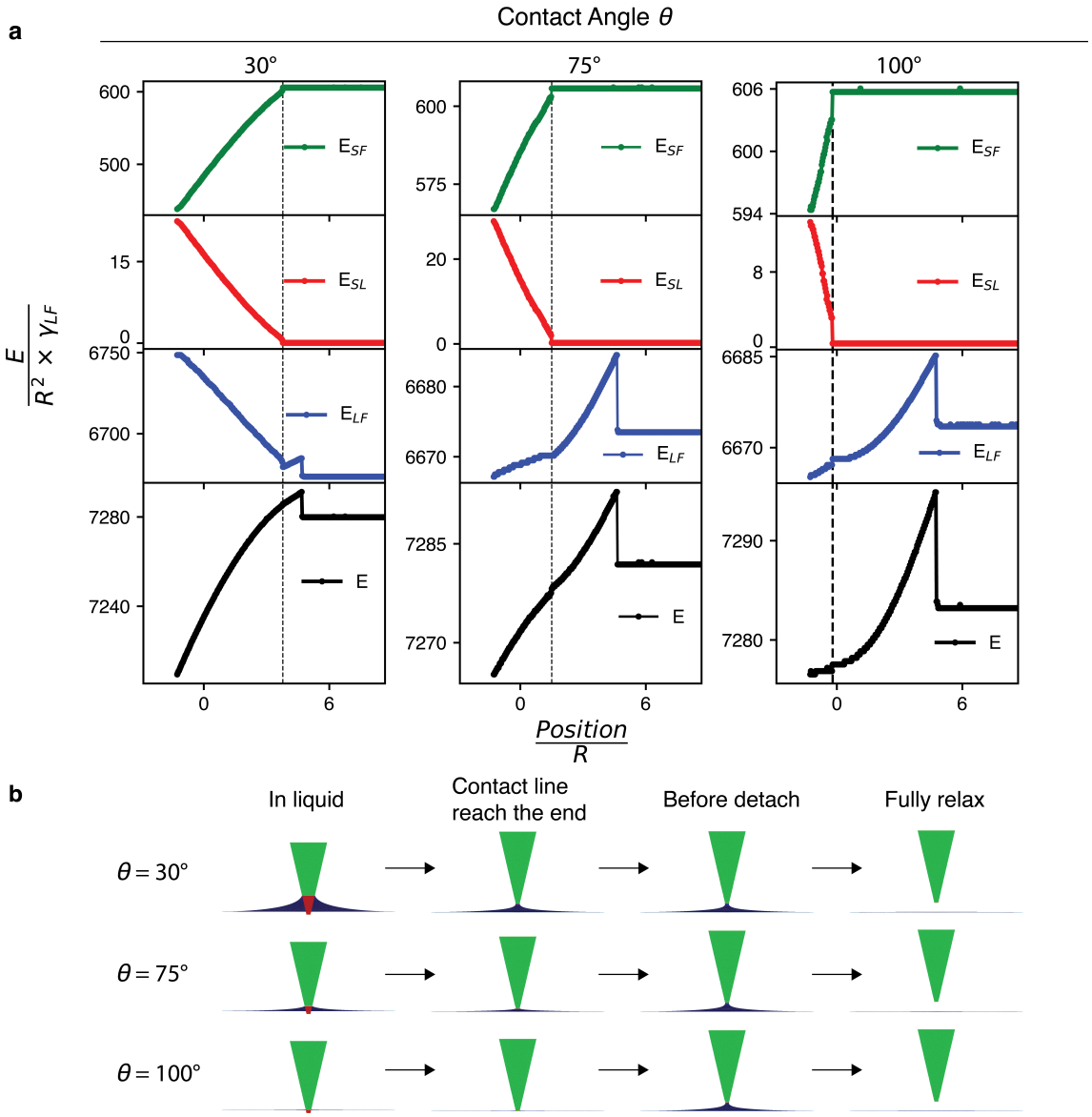

Figure 3.13: **(a)** Energy contributions from the different interfaces in the three-phase system, simulated for different contact angles. In simulation, we set the interfacial tensions $\gamma_{\mathrm{LF}} : \gamma_{\mathrm{SF}} : \gamma_{\mathrm{SL}} = 1 : 1 : (1 - \cos\theta)$, with L , S and F standing for liquid, solid and surrounding fluid, respectively. The total energy for each interface is simply $E = \gamma \times A$, with A is the area of the interface considered. E_{LF}, E_{SF}, and E_{SL} are the energy contributions from the three interfaces, respectively. E is the overall energy in the simulation system. Note that all energies are normalised by $R^2 \times \gamma_{\mathrm{LF}}$ to be unitless, and the position axis is normalised by R.The dash line represents the tip position where the three- phase contact line reached the edge of the tip apex and pinned there until fully detachment. **(b)** Simulation snapshots (clip view) during tip particle withdrawal from the liquid interface. Initially, the tip particle is immersed within the liquid interface. As it withdraws, the three-phase contact line moves along the particle's side wall until it reaches the particle's apex, where it becomes pinned before the particle fully detaches.

For $53° < \theta < 97°$, the force profile becomes nonmonotonic and can be divided into two stages (Fig. 3.11b). Initially, before the contact line reaches the apex of the tip, the capillary force magnitude decreases (becoming less negative), driven by the combined contributions of the three interfaces as the contact line slides along the conical particle, along with a slight increase of the liquid–fluid interfacial energy. Midway through the withdrawal process, the contact line reaches the apex edges and becomes strongly pinned due to the comparable wetting properties of the liquid and fluid on the solid. The capillary force behaviour shifts to being dominated solely by the liquid–fluid interface, leading to an increase in the capillary force (more negative value) until complete detachment. This behaviour is illustrated at $\theta = 75°$ as in Fig. 3.13.

For $\theta \geq 97°$, the force magnitude increases (becoming more negative in Fig. 3.11b) until rupture of the bridge, behaving monotonically again. As illustrated at $\theta = 100°$ (Fig. 3.13), the meniscus is considerably smaller before the contact line meets the apex due to the similar affinities of the fluid and liquid for the solid particle. The energy profile is primarily governed by an increase in liquid-fluid energy after the contact line reaches the apex edges. Interestingly, comparing cone angle variation in Fig. 3.10b and contact angle variation in Fig. 3.11b, we found that the maximum capillary bridge length before rupture is primarily governed by the cone angle α, while the impact of the contact angle θ is negligible. This indicates that the amplitude of the vertical movement required to detach the particle from the interface is almost independent of the wetting properties of the liquid in the current interfacial configuration.

3.4.5 Towards more realistic systems

The results presented in the previous sections generally achieve good quantitative agreement between experiments and simulation. This is possible thanks to the ideal axisymmetric AFM tips used, although imperfections in the tip geometry and composition already show in the experimental curves. This is exemplified in Fig. 3.11 where electron microscopy highlights defects in the desired axisymmetric geometry as shown in Fig. 3.12. Generally, real-life nanoparticle–liquid interfaces are non-

ideal. Most solids exhibit chemical heterogeneities or geometric imperfections at the nanoscale, ranging from sharp edges to multiple facets with different chemical properties. Each of these factors can influence the force profile, sometimes with distinctive features that differentiate them from the simple cone model. Systematically examining the impact of nanoscale geometrical and chemical variations is experimentally challenging. However, our simulations offer the ideal tool for such a study, having been validated with experiments on simple regular geometries.

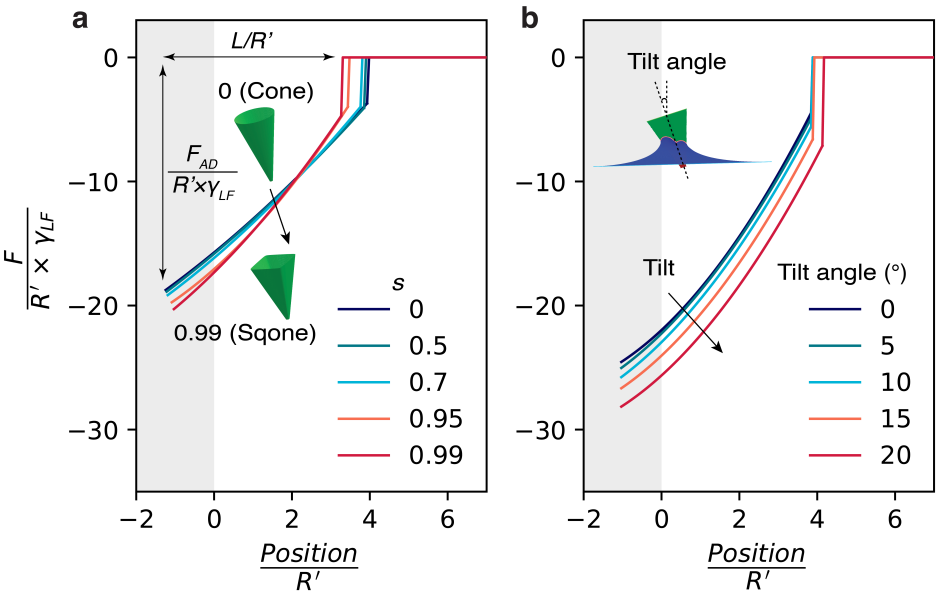

Figure 3.14: Simulation of the adhesion profile of more realistic nanoparticle-interface situations. **(a)** Variation of the shape factor s tuning a cone to a pyramid. **(b)** Tilting of the interface with respect to the axis of the particle. Both position and force axes are normalised to be unitless. L/R' represents the normalised maximum capillary bridge length, and $F_{\mathrm{AD}}/(R' \times \gamma_{\mathrm{LF}})$ represents the normalised maximum adhesion force.

Here, motivated by scenarios that can be anticipated in our AFM experiments, we explore two common experimental scenarios. We start by investigating the impact of a systematic shape alteration whereby a cone is progressively turned into a square pyramid (4 facets and edges) – most AFM tips are pyramidal. Mathematically, we do this by employing the following shape relation [55]:

$$x^2 + y^2 - \frac{s^2 c^2 x^2 y^2}{z^2} = \frac{z^2}{c^2} \quad \left(0 \leq z \leq c, -\frac{z}{c} \leq x \leq \frac{z}{c}, -\frac{z}{c} \leq y \leq \frac{z}{c}\right) \tag{3.2}$$

where $c = 3$, x, y, and z are the three coordinates defining the particle surfaces,

and s is the so-called shape factor. Depending on the value of s, the surface of the particle can be a cone ($s = 0$), a square pyramid ($s = 1$), or something in-between termed a squircular cone (or sqone) for $0 < s < 1$.

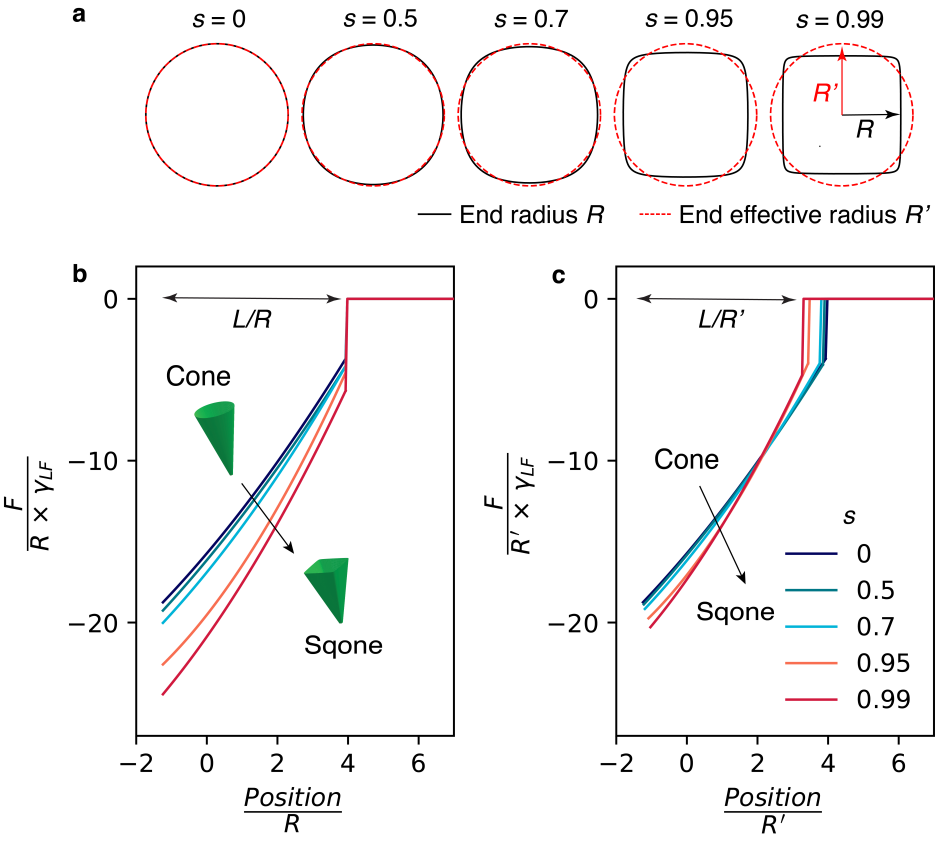

Figure 3.15: Simulation force profiles with varied shape factor s. **(a)** The end cross-sectional shape of the particle, with end radius R and the effective end radius R'. R' is determined by the perimeter of the particle apex. **(b-c)** show different choices of characteristic length for normalisation: (b) employs the end radius R, resulting in a constant normalised maximum capillary bridge length L/R before rupture. (c) employs the effective end radius R', resulting in L/R' decreasing as the shape factor s increases. Note that (c) is the same as Fig. 3.14a.

Simulated force-distance curves are obtained systematically varying s from 0 to 1 (Fig. 3.14a). The results show an increase in the maximum adhesion force as the cone particle transitions towards a pyramid, also leading to a steeper slope. There are two ways to normalise the tip position, either by using the width of the tip apex R or by using the equivalent radius (effective radius) R' of a circle that has the same perimeter as the sqone tip apex (Fig. 3.15a). Here, by choosing the latter in Fig. 3.14a (same as Fig. 3.15c), we observed a decrease in the normalised maximum capillary bridge length L/R' before rupture with increasing shape factor s. How-

ever, if we choose to normalise with R, L/R becomes invariant with s (Fig. 3.15b). Notably, both profiles show that the maximum adhesion force F_{AD} always increases with the increase of the shape factor s, regardless of the choice of normalisation (Fig. 3.15b-c). However, the maximum capillary bridge length L differs based on the normalisation method. This underscores once again that the capillary bridge rupture length depends sensitively on the details of the tip apex. Comparatively, varying the cone angle appears to have a much larger impact on the magnitude of the adhesion force (as discussed in Fig. 3.10b).

Beyond the geometric transition from cone to pyramid, we also account for the fact that in AFM experiments the tip (nanoparticle) often approaches the liquid interface at a tilt rather than perpendicularly. In this case, as shown in Fig. 3.14b, the shape of the force profile remains largely unchanged, but the magnitude of the force increases with the increase of the tilt angle due to the larger overall interface. The maximum capillary bridge length slightly increases with the tilt angle.

3.4.6 General discussion for imperfect particles

Nanoparticle adhesion at liquid interfaces is a complex process where small changes can significantly alter the force profile. Here we build on the variations in geometry and wettability systematically investigated in the previous section to help interpret experimental measurements on non-ideal particles: an irregular conical Spark 70 tip and a pyramidal SNL-10 tip. Although the Spark 70 tip is perfectly conical by design, its manufacture can occasionally lead to irregular tip shapes, as visible in Fig. 3.16a: the tip is sharp at the apex, but it becomes wider and loses its axisymmetry away from the apex. In a retraction process from the interface, the cone angle of the tip decreases as the contact line moves downwards to the apex. This results in a decreased force slope before the rupture of the bridge (Fig. 3.16a, see arrows), which aligns with the force profile's dependence on cone angle variation as shown in Fig. 3.10b. Another possible explanation is some chemical heterogeneity of the tip: the contact angle may be higher at the apex and lower at the bottom due to an imperfect platinum coating, causing the force slope to decrease.

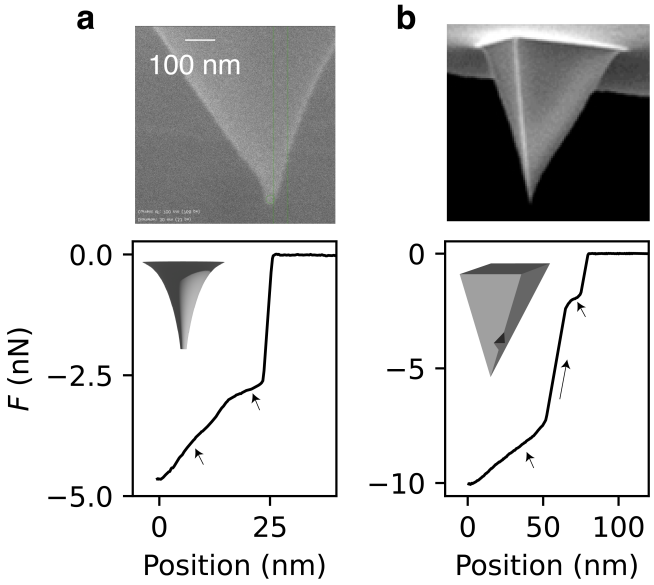

Figure 3.16: Examples of force curve features for imperfect particles in the experiment. **(a)** Retraction of an imperfect Spark 70 tip from an air–oil interface exhibits local decreases in the slope of the force profile (see arrows), likely due to a decrease in the effective tip cone angle as it emerges from the oil (electron microscopy image of the tip). A cartoon illustrates the possible cone angle variation on the tip (inset). **(b)** Retraction of a pyramidal SNL-10 tip shows a stepwise motion (see arrows), likely due to pinning by local geometrical imperfectness or pyramid edges. A cartoon depicts the design of the pyramidal tip with a geometrical imperfection. The electron microscopy is a general SNL-10 image from Bruker, reproduced with permission. [56]

As another example, a pyramidal tip SNL-10 exhibits a stepwise pattern in its force profile during retraction (Fig. 3.16b). The steps (Fig. 3.16b, see arrows) are characterised by sharp changes in the slope, which then return to their original value. This phenomenon is likely due to local geometric imperfections on the tip surface that introduce contact line pinning or tilting between the particle and the interface, hence introducing shifting in the force axis (as in the example in Fig. 3.14b).

Beyond these two simple examples, real-world systems such as dust particles and engineered functional nanoparticles are likely to have even greater variations in size, geometry, and heterogeneity, something that can significantly impact their adhesion profile, as illustrated in this study. A systematic investigation of these effects would require precise control over the tip's surface features down to the nanoscale. This can in principle be achieved through set geometric modifications [57] or controlled chemical alterations of the surface [58].

3.5 Conclusion

In this work, we have explored nanoparticle adhesion at liquid interfaces using experimental and computational simulation approaches. Using dynamic sensing with AFM, we measured the adhesion force profile of nano-cones at liquid interfaces. Continuum simulations of the experiments quantitatively match the experimental results for simple nanoparticle geometries.

We found that the adhesion force increases with the angle of the nano-cone, and with a decrease in contact angle between the liquid and the material composing the tip. The maximum length of the capillary bridge increases significantly with an increase in cone angle, but remains weakly dependent on the liquid wettability on the particle. This indicates that both particle geometry and interfacial properties contribute to the adhesion force of nanoparticles at a liquid interface, with geometry playing a dominant role in the capillary rupture during detachment.

This investigation fills a gap in the understanding of capillary adhesion phenomena for nanoparticles at liquid interfaces, demonstrating that classical thermodynamics still holds quantitatively at the nanoscale, with no significant contribution from the line tension. This enabled us to establish a bound of -1×10^{-12} N $< \tau <$ 1×10^{-10} N for the line tension of our system, in line with both experimental and theoretical values in the literature. [20, 48–50] A more detailed quantification of line tension would require complete control of the nanoscale geometry and chemistry in combination with molecular-level simulations, such as molecular dynamics. Here, nanoscale effects reveal themselves primarily through local tip imperfections inducing fluctuations in the experimentally measured force profile, but these effects cannot be controlled within error. In some cases, the effects can also be simply explained by geometrical effects or 'effective' wetting properties.

We believe this work could provide guiding principles for the design of smart interfaces. For example, these interfaces could be capable of attracting or repelling specific particles based on their shape and chemistry. The present results demonstrate that simulations could help derive effective surface properties of an unknown particle by matching experimental measurements with a range of possible simulation predictions. This foundation could be further expanded by exploring other liquid

interface combinations and investigating more complex particles, such as those with controlled irregular surface geometries or varied wettability (contact angles) across different facets. Beyond single-particle behaviour, our simulation model could also be extended to investigate particle–particle interactions at the liquid interfaces [12]. Additionally, the experimental approach described here can also be easily adapted to explore dynamic effects, for example due to high viscosities of the fluid interfaces. However, addressing such dynamic phenomena computationally would require different approaches such as computational fluid dynamics (CFD) [59] or the Lattice Boltzmann method [60, 61].

References

[1]K. Sun, Y. Gizaw, H. Kusumaatmaja, and K. Voïtchovsky, "Nanoparticle adhesion at liquid interfaces", Soft Matter **21**, 585–595 (2025).

[2]C. de Souza Carvalho, N. Daum, and C.-M. Lehr, "Carrier interactions with the biological barriers of the lung: advanced in vitro models and challenges for pulmonary drug delivery", Advanced Drug Delivery Reviews **75**, 129–140 (2014).

[3]T. Heckenthaler, S. Sadhujan, Y. Morgenstern, P. Natarajan, M. Bashouti, and Y. Kaufman, "Self-cleaning mechanism: why nanotexture and hydrophobicity matter", Langmuir **35**, 15526–15534 (2019).

[4]C. Gómez Suárez, J. Noordmans, H. C. van der Mei, and H. J. Busscher, "Removal of colloidal particles from quartz collector surfaces as stimulated by the passage of liquid-air interfaces", Langmuir **15**, 5123–5127 (1999).

[5]S. Bakand, A. Hayes, and F. Dechsakulthorn, "Nanoparticles: a review of particle toxicology following inhalation exposure", Inhalation Toxicology **24**, 125–135 (2012).

[6]Y. Fujitani, Y. Sugaya, M. Hashiguchi, A. Furuyama, S. Hirano, and A. Takami, "Particle deposition efficiency at air–liquid interface of a cell exposure chamber", Journal of Aerosol Science **81**, 90–99 (2015).

[7]D. S. Frost, E. M. Nofen, and L. L. Dai, "Particle self-assembly at ionic liquid-based interfaces", Advances in Colloid and Interface Science, Manuel G. Velarde **206**, 92–105 (2014).

[8]Y. Fu, S. Zhao, W. Chen, Q. Zhang, and Y. Chai, "Self-assembly of nanoparticles with stimulated responses at liquid interfaces", Nano Today **54**, 102073 (2024).

[9]A. D. Scheludko and D. Nikolov, "Measurement of surface tension by pulling a sphere from a liquid", Colloid and Polymer Science **253**, 396–403 (1975).

[10]C. Huh and S. G. Mason, "Sphere tensiometry: an evaluation and critique", Canadian Journal of Chemistry **54**, 969–978 (1976).

[11]H.-J. Butt and M. Kappl, "Normal capillary forces", Advances in Colloid and Interface Science **146**, 48–60 (2009).

[12]S. Dasgupta, M. Katava, M. Faraj, T. Auth, and G. Gompper, "Capillary assembly of microscale ellipsoidal, cuboidal, and spherical particles at interfaces", Langmuir **30**, 11873–11882 (2014).

[13]P. M. McGuiggan and J. S. Wallace, "Maximum force technique for the measurement of the surface tension of a small droplet by AFM", The Journal of Adhesion **82**, 997–1011 (2006).

[14]G. Soligno, M. Dijkstra, and R. van Roij, "Self-assembly of cubes into 2d hexagonal and honeycomb lattices by hexapolar capillary interactions", Physical Review Letters **116**, 258001 (2016).

[15]P. Sudersan, M. Müller, M. Hormozi, S. Li, H.-J. Butt, and M. Kappl, "Method to measure surface tension of microdroplets using standard AFM cantilever tips", Langmuir **39**, 10367–10374 (2023).

[16]H. Cooray, P. Cicuta, and D. Vella, "The capillary interaction between two vertical cylinders", Journal of Physics: Condensed Matter **24**, 284104 (2012).

[17]A. Dani, M. Yeganeh, and C. Maldarelli, "Hydrodynamic interactions between charged and uncharged brownian colloids at a fluid-fluid interface", Journal of Colloid and Interface Science **628**, 931–945 (2022).

[18]E. Guzmán, F. Ortega, and R. G. Rubio, "Forces controlling the assembly of particles at fluid interfaces", Langmuir **38**, 13313–13321 (2022).

[19]M. Kanduč, L. Eixeres, S. Liese, and R. R. Netz, "Generalized line tension of water nanodroplets", Physical Review E **98**, 032804 (2018).

[20]T. Pompe and S. Herminghaus, "Three-phase contact line energetics from nanoscale liquid surface topographies", Physical Review Letters **85**, 1930–1933 (2000).

[21]O. H. Pakarinen, A. S. Foster, M. Paajanen, T. Kalinainen, J. Katainen, I. Makkonen, J. Lahtinen, and R. M. Nieminen, "Towards an accurate description of the capillary force in nanoparticle-surface interactions", Modelling and Simulation in Materials Science and Engineering **13**, 1175–1186 (2005).

[22]B. Cappella, "Force-distance curves on lubricant films: an approach to the characterization of the shape of the AFM tip", Micron **93**, 20–28 (2017).

[23]X. Li, C. Chen, Q. Niu, N.-W. Li, L. Yu, and B. Wang, "Self-assembly of nanoparticles at solid-liquid interface for electrochemical capacitors", Rare Metals **41**, 3591–3611 (2022).

[24]S. Shi and T. P. Russell, "Nanoparticle assembly at liquid–liquid interfaces: from the nanoscale to mesoscale", Advanced Materials **30**, 1800714 (2018).

[25]J. Ally, E. Vittorias, A. Amirfazli, M. Kappl, E. Bonaccurso, C. E. McNamee, and H.-J. Butt, "Interaction of a microsphere with a solid-supported liquid film", Langmuir **26**, 11797–11803 (2010).

[26]S. E. Anachkov, I. Lesov, M. Zanini, P. A. Kralchevsky, N. D. Denkov, and L. Isa, "Particle detachment from fluid interfaces: theory vs. experiments", Soft Matter **12**, 7632–7643 (2016).

[27]W. R. Bowen, N. Hilal, R. W. Lovitt, and C. J. Wright, "An atomic force microscopy study of the adhesion of a silica sphere to a silica surface—effects of surface cleaning", Colloids and Surfaces A: Physicochemical and Engineering Aspects **157**, 117–125 (1999).

[28]D. Daniel, C. L. Lay, A. Sng, C. J. Jun Lee, D. C. Jin Neo, X. Y. Ling, and N. Tomczak, "Mapping micrometer-scale wetting properties of superhydrophobic surfaces", Proceedings of the National Academy of Sciences **116**, 25008–25012 (2019).

[29]T. Jiang and Y. Zhu, "Measuring graphene adhesion using atomic force microscopy with a microsphere tip", Nanoscale **7**, 10760–10766 (2015).

[30]F. Schellenberger, P. Papadopoulos, M. Kappl, S. A. L. Weber, D. Vollmer, and H.-J. Butt, "Detaching microparticles from a liquid surface", Physical Review Letters **121**, 048002 (2018).

[31]V. Zila, E. Margiotta, B. Turoňová, T. G. Müller, C. E. Zimmerli, S. Mattei, M. Allegretti, K. Börner, J. Rada, B. Müller, M. Lusic, H.-G. Kräusslich, and M. Beck, "Cone-shaped HIV-1 capsids are transported through intact nuclear pores", Cell **184**, 1032–1046.e18 (2021).

[32]H. Zhao, F. Liang, X. Qu, Q. Wang, and Z. Yang, "Conelike janus composite particles", Macromolecules **48**, 700–706 (2015).

[33]J. A. Finbloom, C. Huynh, X. Huang, and T. A. Desai, "Bioinspired nanotopographical design of drug delivery systems", Nature Reviews Bioengineering **1**, 139–152 (2023).

[34]S. J. Goodband, S. Armstrong, H. Kusumaatmaja, and K. Voïtchovsky, "Effect of ageing on the structure and properties of model liquid-infused surfaces", Langmuir **36**, 3461–3470 (2020).

[35]B. V. Orme, G. McHale, R. Ledesma-Aguilar, and G. G. Wells, "Droplet retention and shedding on slippery substrates", Langmuir **35**, 9146–9151 (2019).

[36]J. D. Smith, R. Dhiman, S. Anand, E. Reza-Garduno, R. E. Cohen, G. H. McKinley, and K. K. Varanasi, "Droplet mobility on lubricant-impregnated surfaces", Soft Matter **9**, 1772–1780 (2013).

[37]T.-S. Wong, S. H. Kang, S. K. Y. Tang, E. J. Smythe, B. D. Hatton, A. Grinthal, and J. Aizenberg, "Bioinspired self-repairing slippery surfaces with pressure-stable omniphobicity", Nature **477**, 443–447 (2011).

[38]B. J. Connolly, E. Loth, and C. F. Smith, "Shape and drag of irregular angular particles and test dust", Powder Technology **363**, 275–285 (2020).

[39]S. Zhou, Y. Yang, and H. Shang, "Adhesion behavior of underground coal dust with fused silica: effects of relative humidity and particle size", Processes **12**, 735 (2024).

[40]P. Zhang, H. Chen, L. Zhang, T. Ran, and D. Zhang, "Transparent self-cleaning lubricant-infused surfaces made with large-area breath figure patterns", Applied Surface Science **355**, 1083–1090 (2015).

[41]A. K. Epstein, T.-S. Wong, R. A. Belisle, E. M. Boggs, and J. Aizenberg, "Liquid-infused structured surfaces with exceptional anti-biofouling performance", Proceedings of the National Academy of Sciences **109**, 13182–13187 (2012).

[42]G. Wang and Z. Guo, "Liquid infused surfaces with anti-icing properties", Nanoscale **11**, 22615–22635 (2019).

[43]K. A. Brakke, "The surface evolver", Experimental Mathematics **1**, 141–165 (1992).

[44]C. A. Schneider, W. S. Rasband, and K. W. Eliceiri, "NIH image to ImageJ: 25 years of image analysis", Nature Methods **9**, 671–675 (2012).

[45]H.-J. Butt and M. Jaschke, "Calculation of thermal noise in atomic force microscopy", Nanotechnology **6**, 1 (1995).

[46]A. F. Stalder, T. Melchior, M. Müller, D. Sage, T. Blu, and M. Unser, "Low-bond axisymmetric drop shape analysis for surface tension and contact angle measurements of sessile drops", Colloids and Surfaces A: Physicochemical and Engineering Aspects **364**, 72–81 (2010).

[47]R. N. Wenzel, "RESISTANCE OF SOLID SURFACES TO WETTING BY WATER", Industrial & Engineering Chemistry **28**, 988–994 (1936).

[48]F. Bresme and M. Oettel, "Nanoparticles at fluid interfaces", Journal of Physics: Condensed Matter **19**, 413101 (2007).

[49]B. M. Law, S. P. McBride, J. Y. Wang, H. S. Wi, G. Paneru, S. Betelu, B. Ushijima, Y. Takata, B. Flanders, F. Bresme, H. Matsubara, T. Takiue, and M. Aratono, "Line tension and its influence on droplets and particles at surfaces", Progress in Surface Science **92**, 1–39 (2017).

[50]A. Amirfazli and A. W. Neumann, "Status of the three-phase line tension: a review", Advances in Colloid and Interface Science **110**, 121–141 (2004).

[51]S. Friedrich and B. Cappella, "Study of micro- and nanoscale wetting properties of lubricants using AFM force–distance curves", Tribology Letters **68**, 36 (2020).

[52]P. Boonpuek and J. R. Felts, "Determination of the radii of coated and uncoated silicon AFM sharp tips using a height calibration standard grating and a nonlinear regression function", Beilstein Journal of Nanotechnology **14**, 1200–1207 (2023).

[53]Y. D. Yan, T. Sun, and S. Dong, "Study on effects of tip geometry on AFM nanoscratching tests", Wear **262**, 477–483 (2007).

[54]J. W. Gibbs, "On the equilibrium of heterogeneous substances", American Journal of Science **s3-16**, 441–458 (1878).

[55]C. Fong, "Squircular calculations", arXiv, arXiv:1604.02174 (2021).

[56]Bruker, *Sharp nitride lever probes — contact mode — bruker AFM probes*, (2024) `https://www.brukerafmprobes.com/p-3693-snl-10.aspx?srsltid=AfmBOoolX-oStt1Uy_jf_0DAuG8ZMF1D-SSeWLlM6Wm-OLHxrT5wKXSF` (visited on 08/31/2024).

[57]J. Ally, M. Kappl, and H.-J. Butt, "Adhesion of particles with sharp edges to air–liquid interfaces", Langmuir **28**, 11042–11047 (2012).

[58]K. Kobayashi, J. Wei, R. Iida, K. Ijiro, and K. Niikura, "Surface engineering of nanoparticles for therapeutic applications", Polymer Journal **46**, 460–468 (2014).

[59]H. N. G. Nguyen, C.-F. Zhao, O. Millet, and A. P. S. Selvadurai, "Effects of surface roughness on liquid bridge capillarity and droplet wetting", Powder Technology **378**, 487–496 (2021).

[60]K. W. Connington, T. Lee, and J. F. Morris, "Interaction of fluid interfaces with immersed solid particles using the lattice boltzmann method for liquid–gas–particle systems", Journal of Computational Physics **283**, 453–477 (2015).

[61]T. Krüger, H. Kusumaatmaja, A. Kuzmin, O. Shardt, G. Silva, and E. M. Viggen, *The lattice boltzmann method: principles and practice*, Graduate Texts in Physics (Springer International Publishing, 2017).

Chapter 4

Stretching and compressing capillary bridges on hydrophilic, hydrophobic, and liquid-infused surfaces

Capillary bridging has long served as a benchmark in colloidal, granular, and adhesion research. From sand castles to biological tissues, the strong cohesive forces generated by liquid bridges underpin processes ranging from particle aggregation to mechanical stability. These forces are also central to technological applications, including surface manufacturing, water condensation, oil recovery, and printing. The work presented in this chapter focuses on capillary bridges between two parallel plates, a geometry that has been studied extensively for hydrophilic solid substrates. These studies have established how capillary forces depend on geometry, wettability, and liquid–gas interfacial tension. In this work, we retain hydrophilic substrates as reference systems, but extend the investigation to hydrophobised surfaces and to LIS, where additional liquid–liquid interfaces and lubricant ridges play a crucial role. LIS have emerged as high-performance superhydrophobic surfaces promoting droplet mobility. Yet, the behaviour of capillary bridges on LIS remains poorly understood. Do the frictionless features that facilitate droplet motion also allow bridges to move or relax more easily? Or do the lubricant ridges that form around the bridge impose new pinning constraints? In addition, could lubricant transfer from the infused layer to the bridge modify the capillary forces or bridge stability elsewhere in the system? In this chapter, we investigate these questions by systematically stretching and compressing capillary bridges across various surfaces, providing new insight into capillarity at multiphase interfaces. As stated in the Declaration, this is joint work with Sarah J. Goodband.

4.1 Abstract

Capillary liquid bridges are ubiquitous in nature and in technological processes. Here, we comparatively investigate capillary bridges formed between three distinct types of surfaces: (i) hydrophilic glass, (ii) hydrophobic dichlorodimethylsilane (DMS)-functionalised glass, and (iii) liquid-infused surfaces (LIS) (Fig. 4.1). We combine experimental measurements and computer simulations of the capillary bridges' evolution upon changes in the gap size between the surfaces, deriving in each case the bridge geometry and the resulting capillary force. The results, also compared with predictions from the existing theory, follow expected trends on glass and DMS-functionalised surfaces: contact line pinning dominates the bridge behaviour on glass with a characteristic stick-slip motion, whereas a pronounced advancing and receding hysteresis is observed on DMS surfaces (dichlorodimethylsilane-functionalised glass). On LIS, the absence of pinning leads to minimal force variation, gravity-driven breaking of the bridge symmetry, and possible liquid exchange between LIS through bridge cloaking. These effects become particularly significant in asymmetric bridge configurations combining LIS and DMS surfaces, where the transfer of lubricant from LIS to DMS modifies the effective surface tension and alters bridge–surface interactions. Our systematic comparison of the capillary bridge behaviour across solid and liquid interfaces with varying wettability provides a foundation for designing functional surface applications with controlled bridge-surface interactions.

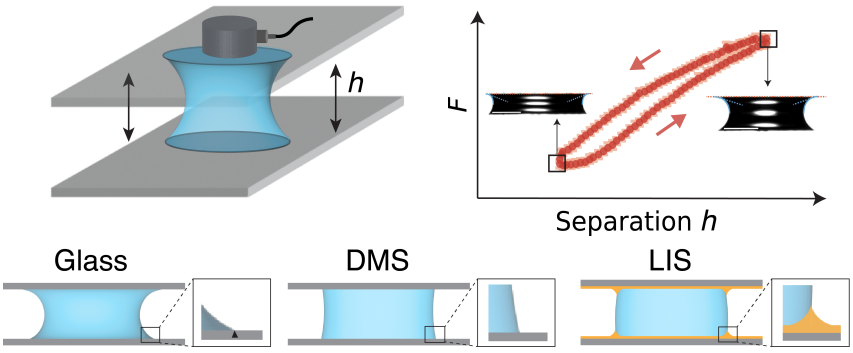

Figure 4.1: Capillary bridges between glass, dichlorodimethylsilane(DMS)-functionalised surfaces, and liquid-infused surfaces (LIS) under compression-stretching cycles, with the inset magnifying the contact between the capillary bridge and the surfaces. Top right: the force profile and images of the bridge between glass.

4.2 Introduction

Capillary liquid bridges form when a liquid meniscus bridges two surfaces, generating strong adhesion forces. They are ubiquitous in nature and industry, from insect adhesion to water surfaces [1, 2] to cohesion in soil and granular media such as sandcastles [3, 4] semiconductor fabrication [5], oil recovery [6], cement drying [7], and drug delivery [8, 9]. At the microscale, these capillary forces can be dominant, also influencing macroscopic properties and temporal evolution of the system. [10–12] The behaviour of capillary bridges is governed by the liquid's properties, bridge dimensions, the chemical and topographical characteristics of the surfaces, and environmental conditions such as temperature and humidity. These effects are reflected in extensive studies examining the impact of surface geometry [4, 13], chemical and topographical patterning [14, 15], wettability [16, 17], and length scales from nanometres [18–20] to millimetres [21, 22]. To uncover the underlying physics, studies usually quantify the bridges geometrical characteristics (*e.g.* contact angles (CAs), curvatures, and contact radius) [15, 23, 24] and measure the capillary forces they exert [22, 25] when they are extended or compressed between solid surfaces.

Despite substantial progress, our understanding of capillary bridge behaviour remains incomplete. Most previous studies have focused on hydrophilic solid surfaces, where contact line pinning dominates and induces hysteresis. [23, 24, 26] More recently, investigations on hydrophobic surfaces with liquid features are emerging [13, 27], reflecting their growing potential in applications such as self-cleaning and anti-fouling technologies. However, most studies hitherto employ solid surfaces, and capillary bridges between liquid-like surfaces are still largely unexplored. Liquid-infused surfaces (LIS) present a typical example of such surfaces, where porous structures are impregnated with a lubricant to achieve high liquid repellency and low friction properties. [28, 29] From a fundamental perspective, LIS represent a distinct capillary behaviour regime where a three-phase interface is present. From the application side, advances in LIS and related liquid-like functional surfaces such as slippery omniphobic covalently attached liquid (SOCAL) surfaces, are critical in liquid deposition and transport in fields such as anti-icing coatings, inkjet printing, and microfluidics. [30–32] On LIS, pinning and hysteresis are negligible [33, 34], and

the introduction of a lubricant creates more liquid-liquid and liquid-gas interfaces. This can alter capillary morphology and cause deviations from classical force models. Computational modelling by Shek *et al.* has shown lubricants on LIS can produce fundamentally different capillary geometries compared to solid surfaces, with increased vertical friction arising from oil ridges formed around the contact of the bridge and the surface. [35] Furthermore, the fluid nature of LIS could induce other unexplored phenomena, such as lubricant transport between surfaces via capillary bridges.

Here, we quantitatively compare capillary bridges evolution during extension and compression on hydrophilic, hydrophobic, and LIS using a micronewton-precision experimental setup. Experiments are complemented by computational modelling that incorporates apparent contact angle to account for oil ridge formation on LIS, which is experimentally challenging to capture but crucial for influencing bridge geometry and forces. Silicon oxide glass is selected as the hydrophilic surface for its routine use and technological relevance, while DMS-functionalised hydrophobic surface and silicone-oil-infused LIS are selected for their similar contact angles to isolate effects specific to the fluid nature of LIS. Comparison across these three surface types presents distinct force and geometry responses driven by phenomena such as stick-slip motion, contact angle hysteresis, and liquid ridge formation. Tests on dissimilar surface pairs of DMS and LIS further demonstrate bridge asymmetry induced by gravity under small capillary forces, as well as lubricant transfer from LIS to the opposing surface. Overall, we present a systematic experimental and computational study that establishes a benchmark for understanding and predicting capillary bridge evolution on solid and liquid functional surfaces, offering mechanistic insights to the rational design of surfaces with liquid features.

4.3 Methods

4.3.1 Surface preparation

Hydrophilic surface – Glass. Silicon oxide glass coverslips (25×25 mm, VWR, UK) are used directly from a freshly opened box without additional cleaning proce-

dures to ensure chemical stability during measurements.

Hydrophobic surface – DMS. Hydrophobic surfaces are prepared by chemical vapor deposition (CVD) of dichlorodimethylsilane (DMS) on glass coverslips (reference hydrophilic surfaces). [36] Glass slides are sequentially cleaned by acetone (99%, Sigma-Aldrich, UK) and isopropanol (99.8%, Fisher Scientific, UK), followed by 30 min of sonication. They are then dried under nitrogen and plasma-cleaned for 10 min (>30 W, VacuLAB-X, UK) and dehydrated in an oven at 100 °C for 1 h. For CVD, 1 mL of DMS is placed in an open dish in a desiccator along with the slides directly transferred from the oven and kept under vacuum overnight. Finally, the slides are rinsed with acetone and ultrapure water (18.2 MΩ · cm, Merck-Millipore, UK), then dried at 40° C overnight.

LIS. LIS are prepared following established protocols. [37, 38] In short, glass slides are first cleaned by soaking in an aqueous solution of Decon 90 (Decon Laboratories Ltd., UK) before rinsing and sonicating in ultrapure water to remove residual detergent, followed by air-drying. Prior to coating, slides are rinsed with acetone and isopropanol and dried under nitrogen and then air-dried. Five layers of nanoparticles are then sequentially applied to the surface using a liquid spray (GLACO™, SOFT 99 Corp.) with 1 h interval between layers. A drop of 50 µL silicone oil (20 cSt @ 25° C, Sigma-Aldrich, UK) is then placed on the surface and spin-coated (2000 rpm, 5 min). The slides are used immediately or stored without oil coating, in closed Petri dishes for a maximum of 2 weeks.

4.3.2 Capillary bridge measurement and error control

The setup and protocols are as described in Goodband et al. [39] We maintain identical capillary bridge volume and composition across all experiments to ensure direct comparison. Briefly, two solid surfaces prepared using the above protocols are mounted onto a custom-built plate using an adhesive (Reprorubber®, Bowers Group, UK) and are allowed to cure for 2 h before the plate is mounted to the force sensor. The force sensor is then equilibrated for 1 h before measurements. To ensure protocol consistency and data reproducibility, a 10 μL droplet (80 wt% glycerol in ultrapure water, to limit evaporation) is placed always onto the bottom surface

and is gently brought into contact with the top surface, followed by equilibration for 2 min. Preliminary experiments show that pinning and gravity impact are observed when varying the initial droplet placement, but the final capillary bridge behaviour was unaffected by whether the droplet started on the top or bottom surface (Fig. 4.2). During measurements, the bridge is firstly extended and then compressed at a constant rate of 0.008 mm s^{-1}, with a maximum separation difference of 0.5 mm between the most compressed and most stretched states. This velocity was selected based on the validation by Goodband et al. [39], where measurements at this rate showed negligible load cell creep. In addition, the corresponding capillary number ($Ca \sim 5 \times 10^{-6}$, Table 1.1) is small, indicating that viscous effects are negligible and that the measurements approximate the quasi-static regime. This assumption is further supported by the close agreement between experiment and simulation presented in the Results Section.

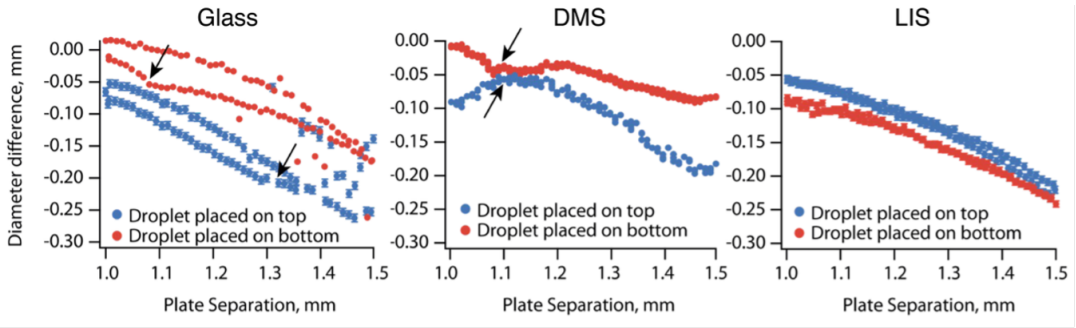

Figure 4.2: Variation of the difference between the top and bottom contact diameters of the capillary bridge over an extension-compression cycle. In all cases, a 10 μL droplet of glycerol solution is initially placed either on the top surface (blue) or bottom surface (red) before forming a capillary bridge with the other surface. The difference is negative for most surface separations, indicating a larger bottom diameter. This is consistent with the expected effect of gravity. However, on Glass, the difference can initially be positive at small separation, depending on where the droplet is initially placed. Additionally, for Glass and DMS, the largest difference is observed when the droplet is initially placed on the top surface. These observations are counterintuitive considering how gravity breaks the capillary bridge symmetry and point to pinning effects. On both Glass and DMS, significant pinning events can be seen during the experiment (see arrows). On LIS, the system behaves consistently as expected when considering gravity and in the absence of pinning. Overall, the droplet position at start does not affect the final capillary bridge behaviour.

Accurate tracking of the capillary bridge contact line is important for understanding pinning effects but is experimentally challenging to achieve simultaneously

at both the top and bottom interfaces due to limitations in optical focus. However, capturing information at both extremities is necessary for quantifying the gravitational effects, probing asymmetric bridges, and evaluating the experimental approach against theoretical predictions. In practice, we acquire top and bottom measurements separately by re-adjusting camera to capture top and bottom in subsequent extension-compression cycles, with control experiments confirming that the measured values do not vary significantly (Fig. 4.3). Even following the same protocol, variations in the measured geometrical parameters can be observed between data sets. For instance, changes in ambient humidity and temperature can result in CA variations of $\sim 2^\circ$ for a LIS sample [38], and DMS surfaces (dichlorodimethylsilane-functionalised glass) are observed to have up to 3° CA differences following the same protocol. In all cases, the measurements are conducted over a few hours to minimise environmental impact and ensure highly consistent data sets.

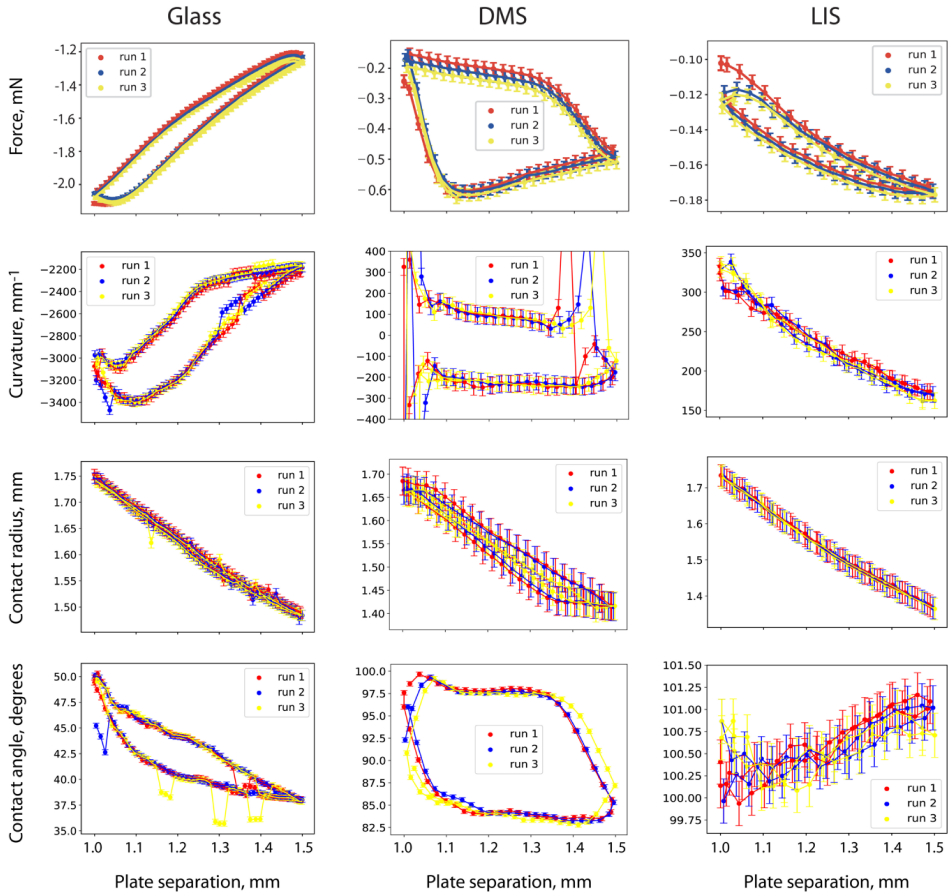

Figure 4.3: Evolution of the force, curvature, contact radius and contact angle for each system over a number of extension-compression cycles. In all cases the camera is focusing on the top part of the bridge. For each set of surfaces, the measurements are fully reproducible within error between consecutive cycles. This confirms the suitability of a sequential strategy for investigating the behaviour of the bottom and the top of a particular capillary bridge.

4.3.3 Capillary force calculation

To quantify the capillary force exerted by a capillary bridge, it is necessary to measure its geometry throughout the experiment. Fig. 4.4 shows the key geometrical parameters of a capillary bridge formed between two parallel substrates. Forces are measured exclusively on the top substrate, but they can theoretically be calculated for both.

When gravity is negligible, *e.g.* for a bridge much smaller than the capillary length, the equilibrium capillary force F between two identical parallel plates can

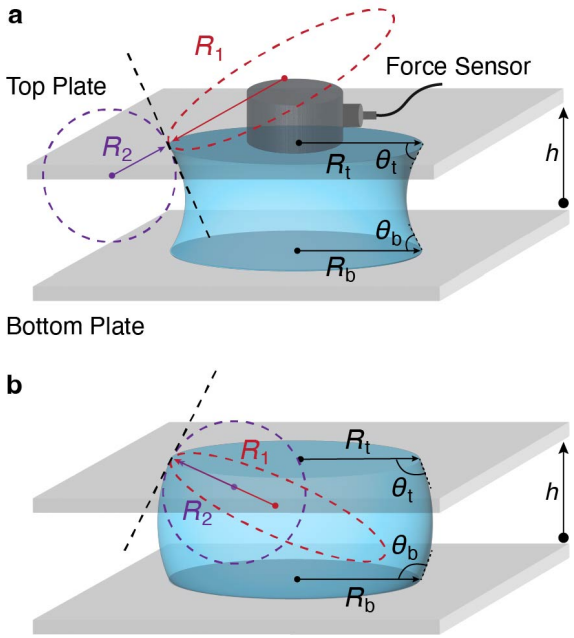

Figure 4.4: Schematics of concave **(a)** and convex **(b)** capillary bridges between two parallel plates separated by a distance h. θ_t and θ_b denote the contact angles at the top and bottom of the bridge, R_t and R_b are the corresponding top and bottom contact radii. The mean curvature of the bridge is determined from the azimuthal (R_1) and meridional (R_2) radii of curvature. R_1 and R_2 are obtained orthogonally at either the top (illustrated here) or the bottom of the bridge, depending on which plate the force is being calculated for.

be expressed by the direct action of surface tension and Laplace pressure: [11, 35]

$$F = -2\pi\gamma R\sin(\theta) + \pi R^2\Delta P \tag{4.1}$$

where γ is the liquid surface tension, R is the contact radius, θ is the contact angle, and ΔP is the Laplace pressure defined consistently with Eq. 1.5, $\Delta P = p_{in} - p_{out}$. When gravity is negligible, the top and bottom contact angles and contact radii are equal. When gravity cannot be neglected, the capillary bridge becomes asymmetric, and forces exerted by the top and bottom differ. Following the Young-Laplace equation (Eq. 1.5), the capillary force on the top plate can be calculated from the geometrical parameters at the top:

$$F_t^{\text{calc}} = -2\pi\gamma R_t\sin(\theta_t) + \pi R_t^2\gamma\left(\frac{1}{R_{1,t}} + \frac{1}{R_{2,t}}\right) \tag{4.2}$$

where R_t and θ_t are the top contact radius and contact angle. The radii of curvature

$R_{1,t}, R_{2,t}$ and $R_{1,b}, R_{2,b}$ correspond to the azimuthal and meridional radii of curvature, respectively, evaluated locally at the top and bottom plates. For a concave capillary bridge, R_1 is positive and R_2 is negative; for a convex capillary bridge, both R_1 and R_2 are positive. Hereafter, this equation will be called the 'top calculated force' F_t^{calc}. Similarly, the bottom capillary force can be expressed as:

$$F_b^{\text{calc}} = -2\pi\gamma R_b \sin(\theta_b) + \pi R_b^2 \gamma \left(\frac{1}{R_{1,b}} + \frac{1}{R_{2,b}} \right) \tag{4.3}$$

where R_b and θ_b are the bottom contact radius and contact angle. Since this expression relies on the bottom measured parameters, it will hereafter be called the 'bottom calculated force' F_b^{calc}. In the experimental setup, a force sensor is implemented on the top plate to acquire a 'top measured force' F_t^{meas}. While the bottom force cannot be measured directly, it can be easily inferred from the top measured force by accounting for gravity:

$$F_b^{\text{inf}} = F_t^{\text{meas}} + \rho g V \tag{4.4}$$

where ρ is the density of the droplet, V is the capillary bridge volume, and g is the gravitational acceleration. Since this approach relies on the top measured force to infer the bottom force, it will be referred to as the 'bottom inferred force' F_b^{inf}. Eq. 4.3 and Eq. 4.4 thus provide two complementary methods to determine the bottom force, the advantages of which are discussed in detail in the Results Section.

4.3.4 Computational model

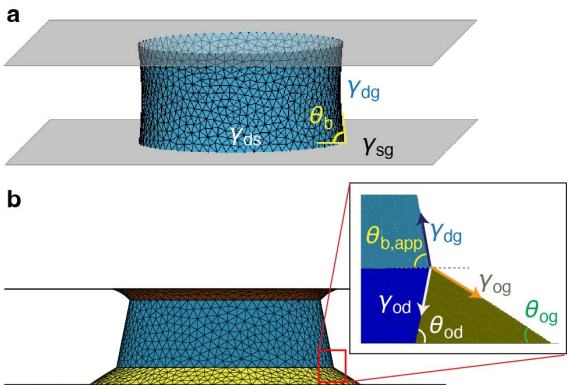

Figure 4.5: Simulation snapshots of capillary bridges between two solid parallel plates **(a)** and between plates with oil rings **(b)**. γ_{ds}, γ_{dg}, γ_{sg}, γ_{od}, and γ_{og} are the interfacial tensions of the droplet-solid, droplet-gas, solid-gas, oil-droplet, and oil-gas interfaces, respectively. θ_b is the contact angle of the capillary bridge on the bottom plate, and $\theta_{b,app}$ is the apparent contact angle of the droplets on oil-infused bottom substrates. The inset in (b) illustrates the Neumann triangle, with contact angles θ_{og} for the oil with at the bottom plate and θ_{od} for the oil in contact with the bridge.

We employ quasistatic simulation using the Surface Evolver [40] software. In brief, the model incorporates the fluid and solid interfaces, with vertices relax in a gradient descent manner to reach the system's minimum energy configuration. The capillary bridges studied here are several millimetres wide, with heights ranging from 1 to 1.4 mm, which is relatively close to the capillary length of the solution (2.39 mm). The corresponding Bond number falls within the range $0.1 < B_o < 0.4$, relatively close to 1. Gravitational effects must therefore be considered not only as an additional weight acting on the bottom surface, but also through their influence on the bridge geometry. In the simulations, gravity is incorporated by matching the Bond number to the experimental value. For simple solid surfaces (Glass and DMS), we initialise the droplets in between two plates, using experimentally measured droplet-gas interfacial tension γ_{dg} and the bottom contact angle θ_b (Fig. 4.5a). The rest of interfacial tensions are related via Young's equation, $\gamma_{ds} = \gamma_{sg} - \gamma_{dg}\cos\theta_b$, where γ_{ds}, γ_{sg} are the droplet-solid and solid-gas interfacial energies, respectively.

For the cases involving LIS or lubricant transfer from LIS to DMS, we include oil ridges surrounding the capillary bridges around its contact with the plate, forming a Neumann triangle at the three-phase interface of oil, droplet, and air (Fig. 4.5b).

Although these features are too small to resolve experimentally, simulations that incorporate the relevant interfacial tensions can infer the three-phase contact geometry. Specifically, the interfacial tensions γ_{od} (oil-droplet), γ_{dg}(droplet-gas), γ_{og} (oil-gas) are obtained from pendent drop measurements. The apparent bridge contact angle, $\theta_{b,app}$, is acquired by fitting the capillary bridge profile against the horizontal substrate. The oil-gas contact angles θ_{og} is either assumed from the intrinsic oil wettability on the substrate or independently determined from lubricant cloaking measurements (details in Result Section 4.4.4 and Fig. 4.13). These quantities are related through the following expression: [35]

$$\cos\theta_{b,\mathrm{app}} = -\cos\theta_{od}\,\frac{\gamma_{od}}{\gamma_{dg}} + \cos\theta_{og}\,\frac{\gamma_{og}}{\gamma_{dg}} \tag{4.5}$$

Eq. 4.5 allows θ_{od} to be derived once $\theta_{b,app}$, θ_{og}, and the interfacial tensions are known. The resulting values of θ_{od}, together with the measured interfacial tensions and a prescribed oil-ridge volume, are then used as inputs for the simulation model. For LIS-LIS systems, θ_{od} remains essentially constant with only minor variation ($\sim$2–3°) during compression and extension. In DMS-LIS systems, the LIS side again shows little change, whereas the DMS side varies strongly, by 30° between the most compressed and extended configurations due to lubricant transfer and ridge pinning. The actual size of the oil ridges depends on factors such as lubricant pressure and oil thickness, which could not be fully captured in the current experimental setup. To satisfy simulation resolution and system symmetry, the oil ridges input in the model may therefore be larger than those in the experiments. Nevertheless, this approximation is based on experimental measurements and yields good agreement between simulated and experimentally measured capillary bridges, indicating that both the oil ridges and the three-phase contact are accurately captured by the model (see Results Section).

The simulations also allow calculation of the exerted capillary force. For convenience, here we evaluate it at the bottom contact line between the droplet and the oil ridge. Adapted from Eq. 4.1, the force is given by:

$$F_{\mathrm{sim}} = -2\pi\gamma_{dg}R_{cl}\sin\theta_{b,\mathrm{app}} + \pi R_{cl}^2\,\Delta P \tag{4.6}$$

where R_{cl} is the contact-line radius between the bridge and the oil ridge, and ΔP is the pressure difference across the droplet body, obtained directly from the simulation output. This formulation links the simulated interfacial geometry to the measurable capillary force, and the resulting predictions are in good agreement with experimental measurements (see Results Section).

4.4 Results and discussion

4.4.1 Capillary bridge between identical parallel surfaces

To build a basic understanding of the capillary behaviour on distinct surfaces, we begin by comparing capillary bridges between identical top and bottom surfaces, ranging from the hydrophilic Glass surface, to the hydrophobic DMS-functionalised surface, and the LIS. For clarity, hydrophilic Glass surface and DMS-functionalised surface will hereafter be referred to as 'Glass' and 'DMS' respectively. Upon extension and compression of the capillary bridges, we simultaneously measure and calculate geometrical parameters and exerted forces. Figs. 4.6a-c present the most compressed and most stretched geometries of the capillary bridge, showing good agreement between experiments and simulations for all cases. The bridge geometry differs across surface types, exhibiting convex or concave shapes during extension and compression. To quantify these geometrical variations, we track the evolution of the contact angles, contact radii, and the meridional curvature as a function of plate separation. We first discuss the top contact angle θ_t and top contact radius R_t. On Glass, θ_t decreases as the plate separation increases, spanning a hydrophilic range of 38–50° in conjunction with contact line motion (Figs. 4.6d, g). Hysteresis is observed between extension and compression cycles. Notably, a stepwise increase in θ_t occurs during capillary bridge compression (Fig. 4.6d, inset), without dominant plateaus as the contact line advances or recedes. However, this stepwise feature is not observed in the contact radius R_t (Fig. 4.6g). This observation indicates a complicated stick-slip behaviour involving alternating pinning and rapid movements of the contact line, likely due to small and asymmetric local pinning points as the evolutions of contact angle and radius are not straightforwardly correlated. The ef-

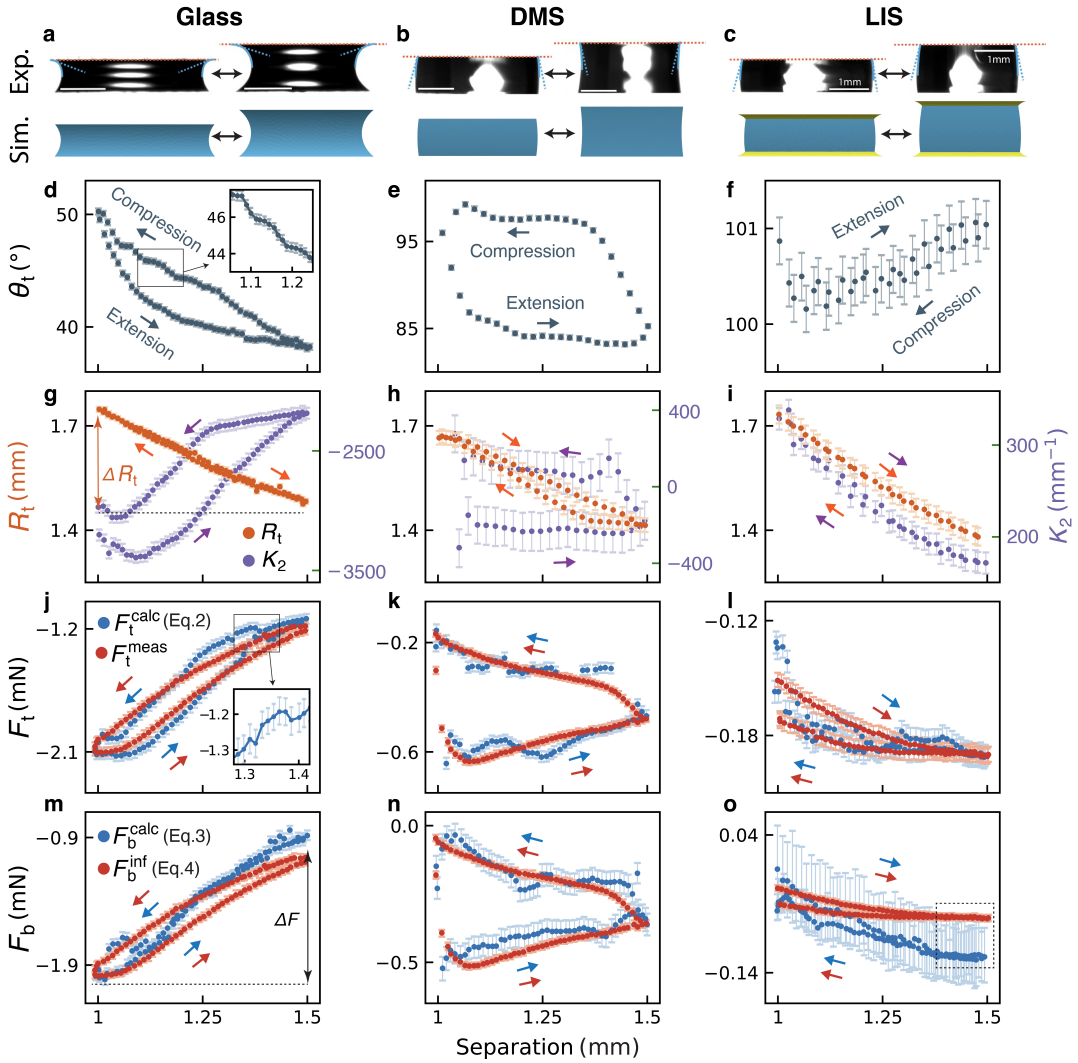

Figure 4.6: Geometry and force comparison of capillary bridges between identical top and bottom surfaces: hydrophilic glass surface, hydrophobic DMS-functionalised surface, and Liquid-infused surfaces (LIS). (a-c) Capillary bridge geometries in the most compressed and most stretched state. Evolution of the geometrical features is shown for top contact angles θ_t (d-f), top contact radius R_t, and meridional curvature K_2 (g-i, $K_2 = 1/R_2$ and R_2 is the meridional radius of curvature in Fig. 4.4). The change in contact radius within an extension-compression cycle, ΔR_t, is marked in (g) as an example. Panels (j-l) compare the measured (F_t^{meas}, red) and calculated force (F_t^{calc}, blue) for the top surface, while panels (m-o) compare the inferred (F_b^{inf}, red) and calculated force (F_b^{calc}, blue) for the bottom surface. Arrows indicate the extension-compression direction in each panel, with ΔF denoting the force variation in the process, as shown in (m). Insets in (d) and (j) highlight the stepwise stick-slip features in the measured contact angles and forces. The dashed square in (o) marks the deviation between the inferred and the calculated bottom forces, particularly at larger plate separations.

fect of pinning is particularly evident when comparing the change in contact radius ΔR_t. Glass exhibits the smallest contact radius variation ($\Delta R_t = 0.27\ mm$, Fig. 4.6g), whereas LIS, which exhibits no pinning, shows the largest $\Delta R_t = 0.4\ mm$

(Fig. 4.6i). For DMS, the CA exhibits typical hysteresis expected for hydrophobic surfaces [23, 26, 41, 42], with a hydrophobic ($> 90°$) advancing CA at $\sim 98°$ and a hydrophilic ($< 90°$) receding CA at $\sim 84°$, corresponding to the plateaus in CA observed during compression and extension, respectively (Fig. 4.6e). In contrast, LIS benefits from its low friction liquid characteristics, yielding a highly stable θ_t with negligible hysteresis within experimental error (Fig. 4.6f). During extension, the slight increase in θ_t at larger separation distance (Fig. 4.6f) can be attributed to interactions between the capillary bridge and the LIS lubricant ridge. This is addressed further in Fig. 4.11 and associated text.

The meridional curvature K_2 ($K_2 = 1/R_2$, where R_2 is the meridional radius of curvature in Fig. 4.4) is closely related to the CA and the overall capillary bridge geometry. Among the three cases, the capillary bridge on Glass experiences the highest curvature at $\sim -3000\,\mathrm{mm}^{-1}$ on average (Fig. 4.6g), due to its low CA and significant contact line pinning. The curvature remains negative, thus the capillary bridge on Glass retains a concave shape during extension and compression. On DMS, θ_t crosses between the hydrophilic and hydrophobic regimes at 90°, resulting in both positive and negative curvatures. The capillary bridge is concave when most stretched and convex when most compressed (Figs. 4.6b, h). As a hydrophobic surface with similar CA, the meridional curvature of the capillary bridge on LIS is of similar magnitude to that on DMS but remains positive, reflecting the relatively constant θ_t and negligible hysteresis (Fig. 4.6i). Overall, curvature hysteresis is highest on Glass, intermediate on DMS, and negligible on LIS, consistent with the observed contact angle hysteresis.

Aside from the geometrical parameters presented in Figs. 4.6d-i, it is useful to consider the symmetry of the contact line during an extension-compression cycle, as capillary bridges do not necessarily move symmetrically when pinning occurs. This can be quantified by tracking the displacement of the contact points at the top and bottom of the capillary bridge with the solid plates after full extension-compression cycles, thereby allowing quantification of asymmetry on both sides. Only small displacements are observed for Glass and LIS due to strong pinning in the former and frictionless motion in the latter. In contrast, DMS exhibits a much larger

asymmetry, resulting from a combination of pinning and contact line displacement (Fig. 4.7). These observations are consistent with the expected behaviour for each system, highlighting the various phenomena at play in capillary bridge behaviour.

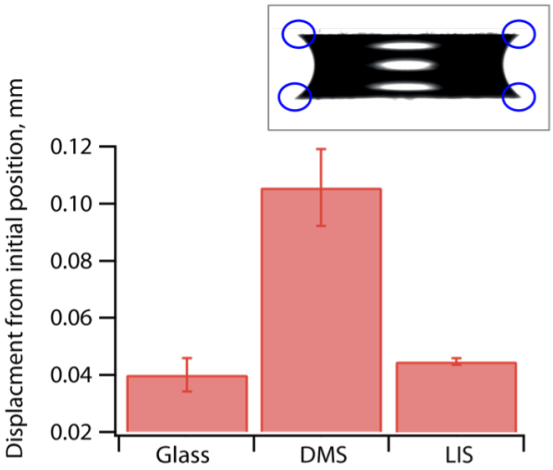

Figure 4.7: Contact line displacement over an extension-compression cycle. The data represents the average displacement of the contact line over 4 separate points (blue highlights in the inset image). On Glass, very little displacement occurs due to high pinning (as shown in Fig. 4.6g and Fig. 4.3), the contact angle constantly changes. The measurement uncertainty represents the uneven movement of the contact lines, where one side may preferentially move more than the other. On DMS, the capillary bridge experiences pinning and a large displacement (sliding). Uneven movement caused by pinning leads to greater displacement and larger errors. In contrast, on LIS, the capillary bridge slides very slowly during the course of the measurement, with all contact lines moving at the same rate, hence resulting in a small error.

From the geometrical parameter evolution during compression and extension, we can now calculate the associated capillary force exerted by the substrates using Eqs. 4.2, 4.3, and 4.4. The forces calculated from geometrical measurements are denoted as F_t^{calc} (Eq. 4.2) and F_b^{calc} (Eq. 4.3) for top and bottom surfaces, respectively. The force directly measured by the force sensor on the top surface is denoted as F_t^{meas}, while the bottom force is inferred by adding a gravity term, and denoted as F_b^{inf} (Eq. 4.4). Figs. 4.6j-o compare measured or inferred forces with the calculated values for each system. Generally, the top measured force F_t^{meas} agrees well with the calculated force F_t^{calc} within experimental error, including on LIS (Figs. 4.6j-l). This suggests that capillary theory developed for solid surfaces can be readily adapted to predict the capillary forces on LIS, at least in the limit of a small lubricant ridge considered in this work.

The magnitude of the capillary force, however, varies significantly across these different systems. On Glass, the stronger interactions between the capillary bridge and the surface yield an absolute force value of $F \sim 2\,\mathrm{mN}$ with a variation of $\Delta F \sim 1\,\mathrm{mN}$ over an extension-compression cycle (Figs. 4.6j, m). In contrast, the force magnitudes on the DMS and LIS are considerably smaller, on the order of 0.1 mN. Notably, the force variation over an extension-compression cycle is five times larger for DMS ($\Delta F \sim 0.4\,\mathrm{mN}$, Figs. 4.6k, n) than for LIS ($\Delta F \sim 0.06\,\mathrm{mN}$, Figs. 4.6l, o), thanks to the frictionless nature of LIS. On Glass and DMS, occasional small deviations between the calculated and measured forces are observed, arising from pinning events that cannot be easily captured experimentally, as pinned points may lie outside of view.

The bottom inferred force F_b^{inf} and calculated force F_b^{calc} still agree within error (Figs. 4.6m-o). However, it is noticeable that agreement is poorer for the bottom than the top of the bridge. This is to some extent expected since the comparison is less direct than at the top surface. On Glass and DMS, F_b^{inf} and F_b^{calc} show good agreement, with an overall behaviour of simply shifted version from the top surface data. On LIS, however, a noticeable difference is observed between the inferred and calculated force (see dashed square in Fig. 4.6o), and several factors contribute to this complex comparison. First, the exerted forces on LIS are considerably smaller than those on Glass or DMS, making the relative errors inevitably larger (Figs. 4.6m-o). Second, there are uncertainties in the surface tension used to calculate F_b^{calc} (Eq. 4.3), as the capillary bridge is likely to be cloaked by the LIS lubricant. Cloaking is a well-known phenomenon in LIS. [43–45] Here, we estimate the spreading coefficient of the lubricant over the capillary bridge to be $S \sim 20\,\mathrm{mN/m}$, suggesting full cloaking. Determining an effective surface tension for the cloaked capillary bridge is not straightforward as the surface tension of a thin film is known to vary with its thickness. [46] In this setup, we are unable to measure the thickness of the cloaking film which may not be uniform and may evolve over the course of an experiment. Moreover, lubricant transport between the two surfaces through the capillary bridge is possible. To reflect this uncertainty, we use an effective surface tension value of $\gamma_{dg} = 50 \pm 2\,\mathrm{mN/m}$, obtained by averaging our pendant drop mea-

surement (analysed by the Opendrop software [47, 48]) with a reported literature value of 52.9 mN/m for a similar system [49]. While relatively small, this change in surface tension is sufficient to significantly affect the data considering the small forces at play ($\sim$ 20–25% of the force value). Finally, the presence of a lubricant ridge around the capillary bridge on LIS further complicates the measurement of the meridional radius of curvature R_2, which is required for calculating F_b^{calc} (Fig. 4.8).

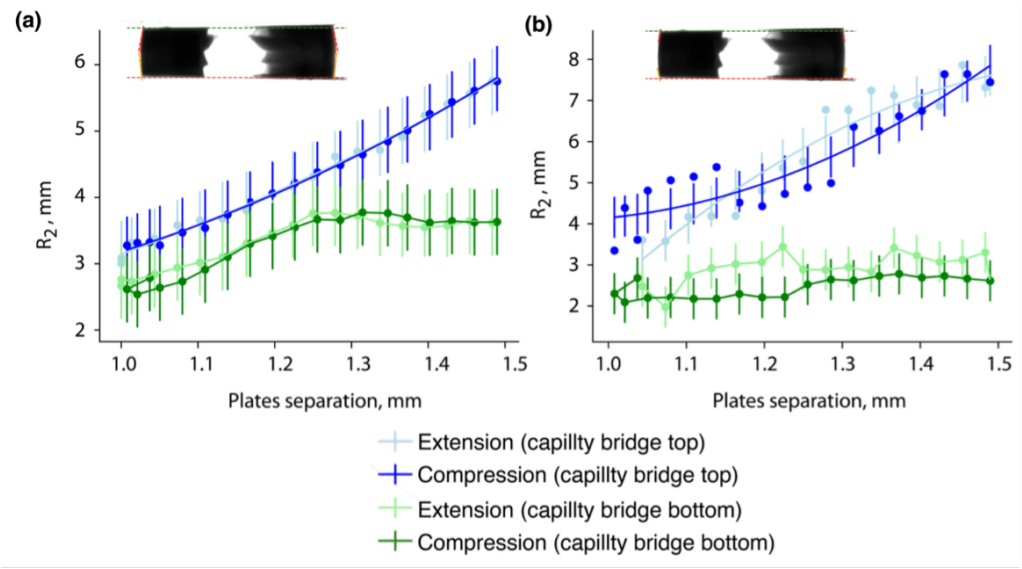

Figure 4.8: Impact of the selected region of the capillary bridge profile used in the fitting [39] carried out to derive the bridge's meridional radius of curvature R_2. To illustrate the issue, the upper graph **(a)** shows the curvature derived from fitting half of the bridge's height, whereas only a quarter of the bridge's height is taken in the lower graph **(b)**. In each graph, the curvature is shown for both the top surface (blue) and bottom surface (green) with the extension data shown darker than the retraction in order to aid visualisation. The example is taken for a capillary bridge between two LIS surfaces. The error bars on all curves represent 0.5 mm.

The above observations and the analysis of the bridges' geometrical features and exerted forces raise three immediate questions: i) For solid surfaces with roughness or chemical heterogeneities, how can the stick-slip motion of the contact line be described, and what is its impact on geometry and force? ii) Why does LIS show poorer bottom force comparison between inferred and calculated force compared to Glass and DMS surfaces? iii) Both DMS and LIS are hydrophobic surfaces but have distinct capillary behaviours. If combined in a single capillary bridge, which behaviour would dominate?

4.4.2 Simulation of stick-slip motion on heterogeneous surfaces

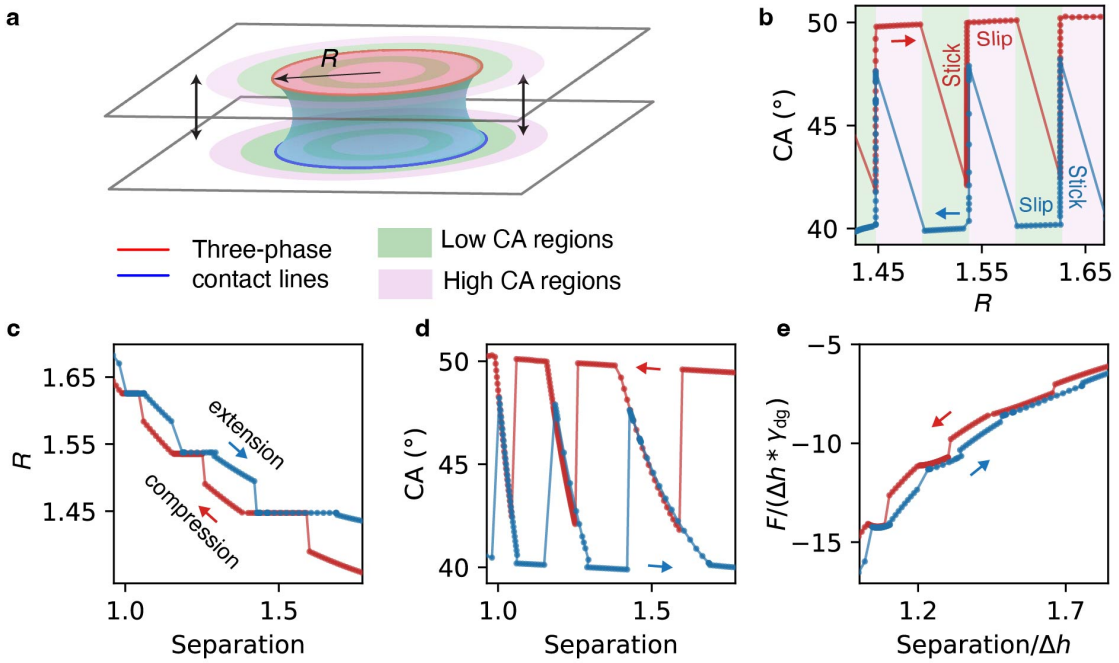

Figure 4.9: Simulated capillary bridge behaviour on a binary-patterned surface featuring alternating high-CA (purple, 50°) and low-CA (green, 40°) rings. The three-phase contact line between the bridge, air, and solid are highlighted in red and blue in **(a)**. The motion of the contact line across the heterogeneous surface exhibits stick–slip behaviour, with the corresponding geometric parameters (contact radius R, and contact angle CA measured near the contact line) and capillary forces shown in **(b–e)**. Gravitational effects are neglected to ensure symmetric contact with both patterned plates, resulting in equal top and bottom contact radii. Δh denotes the maximum plate separation during the compression–extension cycle, and γ_{dg} is the droplet–gas interfacial tension. Because the correlation between bridge separation and base radius is nonlinear, (b) additionally shows the CA plotted against R to directly reflect the imposed binary pattern, whereas (c–e) present all results as a function of separation for consistent comparison with Fig. 4.6

Experimentally, investigating the stick-slip motion in capillary bridges is challenging due to the asymmetric and highly localized nature of contact line pinning. To gain better insights into the underlying mechanisms, we performed numerical simulations examining the bridge geometry evolution and capillary force dynamics during compression and extension cycles over chemically heterogeneous surfaces. Practically, we use a binary-patterned substrate featuring alternating regions of high and low contact angles (40° and 50°, respectively) to systematically model surface chemical heterogeneity (Fig. 4.9). For simplicity, we ignore gravity in the simula-

tions since it is not critical for the contact line pinning-depinning behaviour. During compression (Fig. 4.9b), the three-phase contact line advances until it encounters a boundary transitioning from low-CA to high-CA regions, where strong pinning occurs. At this stage, the contact radius R remains fixed while the bridge height continues to decrease under the applied compression, resulting in an increase in the measured CA. Once the local contact angle reaches the prescribed high-CA value, the pinning constraint is released, allowing the contact line to advance across the high-CA region. When reaching the subsequent low-CA region, the contact line exhibits rapid forward motion due to the energetically favourable wetting conditions. This alternating sequence of pinning and release events repeats throughout the compression process. During stretching, the process is reversed: the receding contact line becomes preferentially pinned at boundaries transitioning toward low-CA regions, where higher wettability disadvantages receding. This pinning behaviour during both compression and extension cycles generates distinctive stepwise variations and hysteresis both in the R and CA evolutions (Figs. 4.9c-d), providing clear experimental signatures of the stick-slip phenomenon.

The capillary force in the above simulation was calculated by Eq. 4.1 with the pressure obtained from the simulation model and normalized by the product of the plate separation change Δh and the droplet-gas interfacial tension γ_{dg}. The resulting force (Fig. 4.9e) exhibits a stepwise behaviour similar to that visible for Glass in Fig. 4.6j.

Similarly, it is possible to simulate roughness-induced contact line pinning and depinning, also inducing stepwise features in force and geometry measurements. For example, we introduce pinning and release of the three-phase contact line on both plates simultaneously in an extension-compression cycle (Fig. 4.10a). When the contact line is free to move, the contact radius R increases during compression and decreases during extension (Fig. 4.10b), with the measured CA near the contact line remaining constant and close to the input parameters (Fig. 4.10c). When the contact line is pinned, the radius remains unchanged (Fig. 4.10b), and the CA increases during compression and decreases during extension as the plates move (Fig. 4.10c). The change in CA is more pronounced at smaller plate separation,

where the bridge is more compressed and constrained such that pinning triggers a stronger response. The capillary force in the simulation was calculated by Eq. 4.1 with the pressure obtained from the simulation model and normalised by the product of the plate separation change Δh and the droplet-gas interfacial tension γ_{dg}. The resulting force (Fig. 4.10d) exhibits a stepwise behaviour similar to that visible for Glass in Fig. 4.6j and that simulated in Fig. 4.9e for chemically heterogeneous surfaces. Together, these simulations confirm the ability of our model to capture the fundamental aspects of the stick–slip hysteresis on binary-patterned and rough surfaces, and offer a basis for studying more complex substrate designs and interfacial interactions.

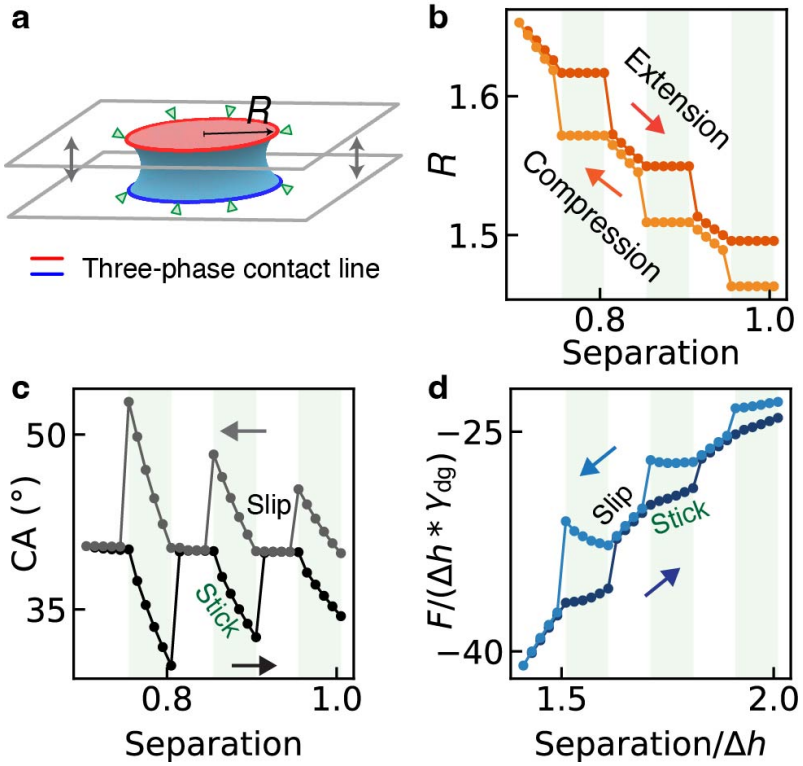

Figure 4.10: Simulation of the stick-slip contact line motion on a non-ideal surface. Here, this is achieved by employing three-phase contact line pinning and release during a capillary bridge compression-extension cycle, as illustrated in **(a)**. The green shaded area indicates where the contact line is pinned, and white area indicates where the contact line is free to move. The change in the bridge bottom radius R is shown in (b), the measured contact angle close to the bottom contact line is shown in (c), and the normalized measured capillary force through simulation is shown in (d).

4.4.3 Top and bottom symmetry of the capillary bridges

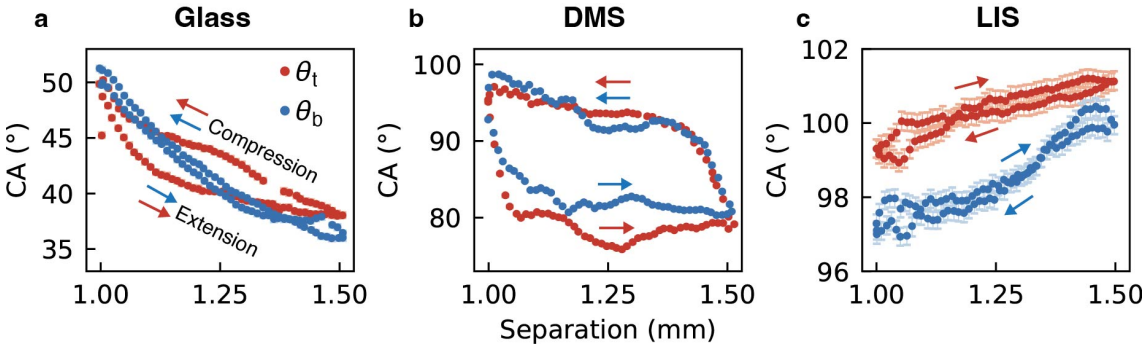

Figure 4.11: Variations in the capillary bridges' top contact angle θ_t (red) and bottom contact angle θ_b (blue) at their contact with Glass **(a)**, DMS **(b)**, and LIS **(c)**. Error bars represent two standard errors and may not be visible on Glass or DMS. The data shown comes from a different set than that presented in Fig. 4.6 but is obtained following an identical protocol.

As discussed in Section 4.4.1, the discrepancy between the bottom inferred force F_b^{inf} and calculated force F_b^{calc} of LIS can be attributed to uncertainty in the parameters used to obtain F_b^{calc} (Eq. 4.3). For capillary bridge on LIS, the capillary shape can be distorted due to differences in the top and bottom lubricant menisci that can modify local interfacial stresses. Also, the bridge-air interface may be non-ideal due to the presence of a cloaking lubricant film. Consequently, F_b^{calc} is a local approximation that may not capture the true force in asymmetric or complex interfaces.

To examine such symmetry effects, we analyse the evolution of the CAs at the top and bottom surfaces for Glass, DMS, and LIS systems (Fig. 4.11). On Glass, the top and bottom CA show similar monotonic decrease upon extension, consistent with contact line pinning and stick-slip motion (Fig. 4.11a). On DMS, both surfaces exhibit the characteristic hysteresis loop discussed in section 4.4.1 (Fig. 4.11b). For LIS, the CAs on both surfaces increase by 2–3° during extension with angles overlapping during outward and return motions, indicating the absence of hysteresis. As the capillary bridge is stretched on LIS, the droplet Laplace pressure decreases, explaining the increase in the apparent CA.

Notably, a small but consistent offset ($\sim 2°$) exists between the apparent top and bottom CAs, θ_t and θ_b (Fig. 4.11c). Unlike pinning-induced asymmetry, this offset originates from the pressure ratio between the bridge and the lubricant. [50,

51] For the typical capillary bridge considered in this work, the hydrostatic pressure difference between the top and bottom of the bridge is sufficient to account for the observed CA asymmetry. The maximum capillary force on LIS is around 5 to 10 times lower than for DMS and Glass (Figs. 4.6j-o), making the geometry more sensitive to gravitational effects. The maximum bottom force for LIS is $\sim 0.15\,\mathrm{mN}$ (Fig. 4.6o), while the gravity term $\rho g V$ (Eq. 4.4) for such capillary bridge is $0.1216\,\mathrm{mN}$, indicating gravity and surface tension effects become comparable. In contrast, capillary bridges on Glass and DMS formed by the same droplet reach maximum forces of 0.7–2.2 mN (Figs. 4.6m, n), where surface tension remains dominant throughout most of the extension-compression cycle.

4.4.4 Asymmetric hydrophobic capillary bridge with DMS and LIS by design

So far, our results have focused on capillary bridges formed between identical top and bottom surfaces. Moving from Glass to DMS to LIS, the surfaces become progressively more hydrophobic, with increasing CAs. Glass and DMS represent widely used bare or functionalised solid surfaces, where the capillary bridge behaviour is dominated by contact line pinning. LIS, in contrast, exhibits distinct behaviour arising from the lubricant's fluid nature, characterised by low friction, dynamic menisci, and low exerted forces. The capillary bridge on LIS is not perfectly symmetric at the top and bottom, although the effects of asymmetry are generally subtle. To explore this further, we design experiments with deliberately asymmetric systems, using different surfaces at the top and bottom. To prevent one surface from dominating, it is helpful to retain some similarity by selecting surfaces of comparable hydrophobicity. Here, we do this by using DMS and LIS surfaces, with each surface alternately positioned on the top or bottom. This asymmetric system is interesting because it represents two hydrophobic surfaces: one a solid surface that exhibits typical hysteresis and pinning, and the other a liquid-infused surface which is smooth, frictionless, and dynamically adaptive.

Fig. 4.12 shows the results of designed asymmetric capillary bridge. The CA measured on the LIS remains almost constant at 98–100°, regardless of whether LIS

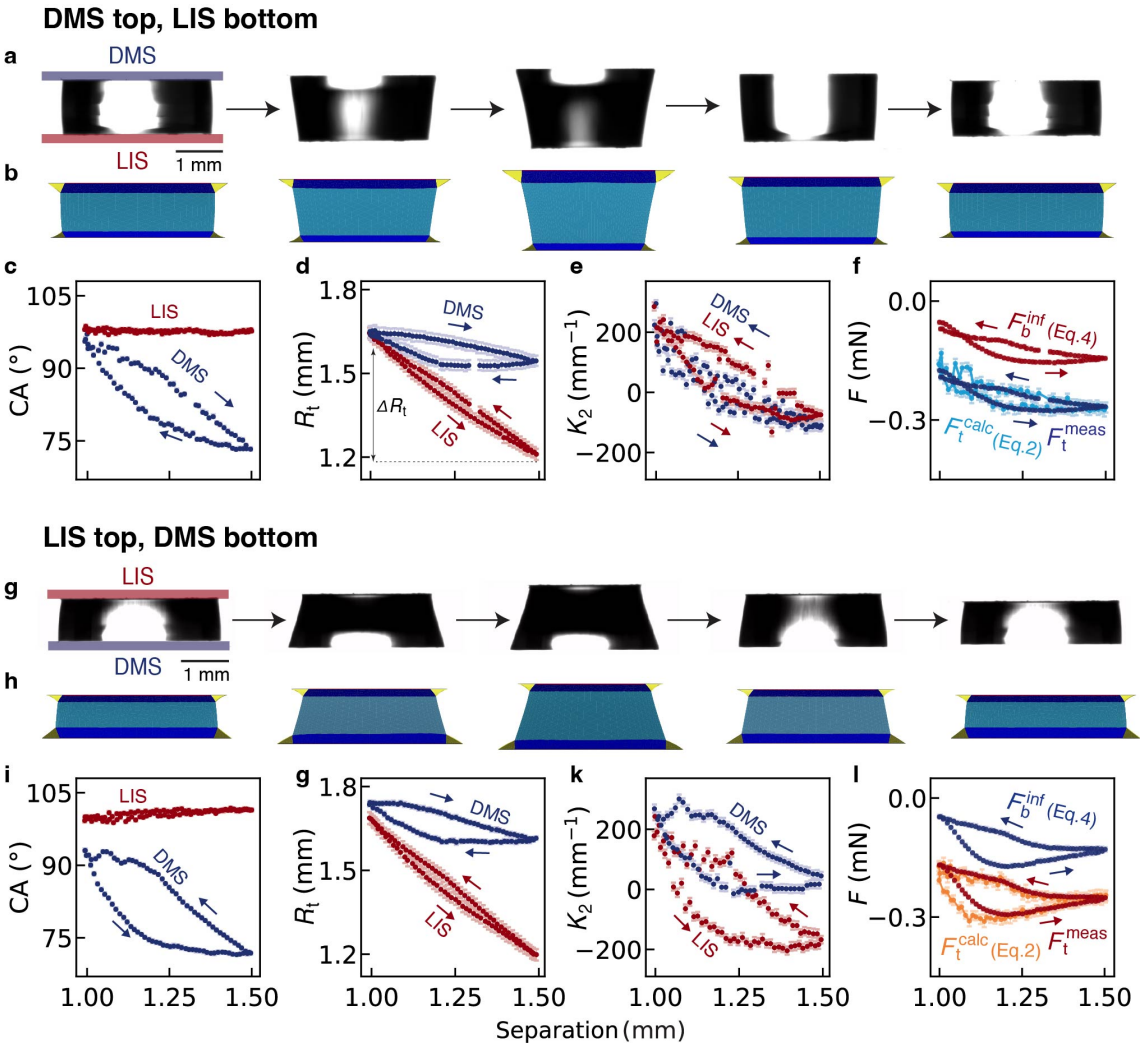

Figure 4.12: Comparative behaviour of asymmetric capillary bridge between LIS (red traces) and DMS (blue traces). **(a, g)** Experimental images of bridge configurations during extension-compression. **(b, h)** Computational simulations incorporating the lubricant ridge (see the Methods Section 4.3.4) are performed for both LIS and DMS, accounting for lubricant transport. The contact angles **(c, i)** remain almost constant on LIS, whereas DMS exhibits a pronounced hysteresis, exploring a larger range of angles than that observed in the symmetric DMS system in Fig. 4.6e. The evolution of capillary bridge-surface top contact radius R_t **(d, g)**, meridional curvature K_2 **(e, k)**, and the exerted forces **(f, l)** are shown. Change in contact radius, denoted by ΔR_t, is marked as an example in (d). Error bars represent standard errors.

is placed at the top or bottom (Figs. 4.12c, i, red traces). The small difference in CA between the two configurations arises from the gravitational deformation of the bridge, consistent with the behaviour observed in the symmetric system (Fig. 4.11c). However, the evolution of the CA on the DMS surfaces is markedly different from that observed in the symmetric DMS system. In the symmetric DMS case, pinning

induces a CA hysteresis loop with two plateaus, an advancing angle of $\sim 98°$ and a receding angle of $\sim 84°$ (Figs. 4.6e and 4.11b). In the asymmetric case here, this hysteresis loop becomes elongated. The CA changes monotonically with larger absolute variations (Figs. 4.12c, i, blue traces), and without stabilising at the typical advancing or receding plateaus. This behaviour originates from two concurrent effects. First, the surface tension of the capillary bridge is altered because the bridge is cloaked by the lubricant. Second, lubricant is transferred from the LIS to the DMS surface. This lubricant accumulation forms a ridge at the bridge–DMS contact line, which broadens the accessible range of CAs. To further investigate these effects, we perform droplet experiments on DMS under cycles of volume variation as lubricant diffuses slowly towards it (Fig. 4.13). Initially, we can identify advancing and receding angles in agreement with Figs. 4.6e and 4.11b for the capillary bridge setup, as the lubricant has no or very limited contact with the droplet. As the lubricant progressively wets the droplets, a ridge forms at the contact line on DMS. This ridge pins the droplet and produces larger droplet CA variation than observed before lubricant contact.

The lubricant ridge is too small for its details to be directly resolved with our experimental setup, but its role can assessed through computational simulations. This is achieved by introducing an oil meniscus around the three-phase contact region at both top and bottom surfaces. For the lubricant ridge on DMS, the oil-gas contact angle θ_{og} is set at 35° (inferred from Fig. 4.13), while for LIS it is set to 15° (representing high spreading; the resulting behaviour is very similar when lower contact angle is employed). Other relevant interfacial tensions are taken from measurements and derivation (see Methods Section 4.3.4 and Eq. 4.5). To maintain symmetry and to balance computational costs and accuracy, the ridge volumes used in the simulations are larger than those in the experiments. This approximation is valid as long as the ridge remains much smaller than the capillary bridge itself, since the local Neumann balance at the three-phase contact line is preserved. As shown in Figs. 4.12a-b and g-h, the simulated bridge geometries closely match the experimental images, confirming the importance of including lubricant ridges at both surfaces. Furthermore, the force calculated from the simulations

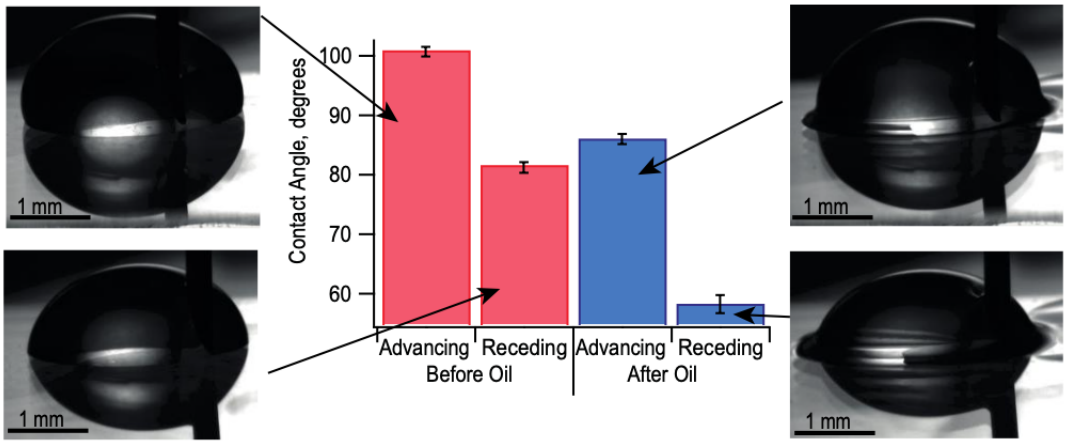

Figure 4.13: Silicone oil-induced droplet pinning on DMS. Representative advancing (top) and receding (bottom) contact angles are shown before (left) and after (right) the lubricant (silicone oil) contacted the base of a droplet of glycerol solution. As the oil contacts the base of the droplet, it spontaneously cloaks it resulting in a reduction of both the advancing and receding angles. The decrease is however more marked for the receding angle (histograms) due to pinning of the contact line by the oil ridge. The ridge forces the droplet to reduce its CA with the DMS as liquid is being pumped out of the droplet. It should be noted that due to the oil ridge, here the CA measurements are manually done by ImageJ rather than capillary bridge fitting method [39] applied elsewhere in this work. There is a 2° discrepancy between these two methods, with the capillary bridge fitting method being more accurate. Error bars represent standard errors.

using Eq. 4.6 agrees well with experimental measurements (Fig. 4.14). Overall, the consistency in both geometry and force demonstrates that the model in Fig. 4.5 reliably captures the physics of capillary bridges involving lubricant ridges. Beyond the present application, this framework can be extended to describe liquid–liquid, liquid–solid, and three-phase interactions on functional surfaces.

We now further examine the geometrical and force responses in these two asymmetric systems. The radius of the contact area changes by $\Delta R_t = 0.5\ mm$ at the LIS interface with no hysteresis, and by $\Delta R_t < 0.1\ mm$ at the DMS interface with some hysteresis (Figs. 4.12d, g). As expected, the bridge preferentially slides across LIS compared to DMS. When LIS is the bottom surface (with DMS on top), the meridional curvature K_2 remains comparable near the top and bottom of the bridge (Fig. 4.12e). This is expected, since the CAs are similar at the onset of the extension ($\sim 95°$ for DMS and $\sim 98°$ for LIS). However, when LIS is positioned at the top and DMS at the bottom, the K_2 at the two surfaces no longer match. An offset and distinct ranges of curvature values are observed near the top and bottom surfaces

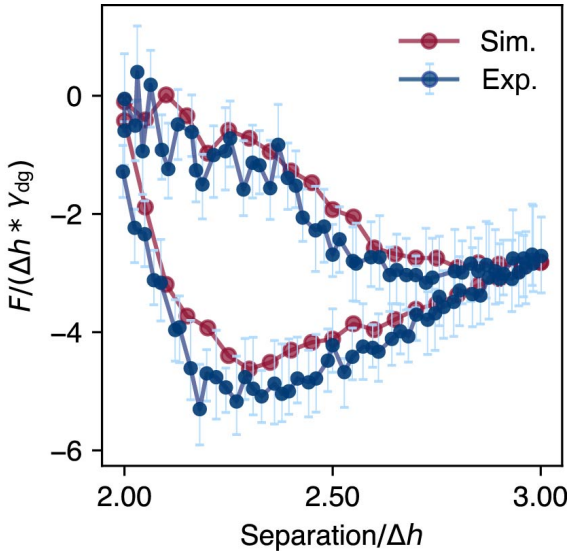

Figure 4.14: Normalised force versus separation for a capillary bridge with the LIS at top and DMS at bottom. The simulated force is obtained from the capillary bridge pressure output following Eq. 4.6, while the experimental force is inferred at the bottom surface using Eq. 4.4 of the main text. The good agreement between experiments and simulations indicates that the model accurately captures the behaviour of asymmetric capillary bridges.

(Fig. 4.12k). This effect can be explained by the influence of gravity on the capillary bridge geometry (CA and R_t), amplified by enhanced lubricant transfer from LIS when it is on top.

Comparison of the measured, calculated and inferred capillary force shows consistently good agreement (Figs. 4.12f, l), with larger hysteresis observed for the LIS-top-DMS-bottom system. In such system, gravity promotes oil transfer from the LIS top to the DMS bottom, leading to the formation of a large oil ridge that enhances pinning or friction during extension or compression of the bridge. Overall, the variations in force are comparable to those in the symmetric LIS systems (Figs. 4.6l, o) regardless of the configuration, which can be explained by a combination of two factors. First, when LIS is present in the system, the surface tension of the bridge drops from 67.4 mN/m [52] to $\sim$ 50 mN/m due to cloaking. Second, the LIS offers a non-pinning surface, allowing contact line to move preferentially and minimize the energy required to extend the bridge. Consequently, contact angles and contact radii follow similar trends on each surface in symmetric systems, whereas the radii of curvature and exerted force reveal the effects of oil transfer and friction characteristic of asymmetric bridges.

4.5 Conclusion

In this study, we systematically investigate capillary bridges on LIS and compare the observed behaviour with two 'standard' non-infused solid surfaces: hydrophilic Glass and hydrophobic DMS. The good agreement between experiments, modelling, and theory demonstrates that our model accurately captures the behaviour of capillary bridges in the quasistatic limit, including for LIS through the use of an effective contact angle. In agreement with previous studies, contact line pinning is prevalent on Glass, giving rise to a complicated stick-slip motion; DMS exhibits typical contact angle hysteresis on hydrophobic surfaces, with well-defined geometrical features during extension-compression. [23, 52, 53] In contrast, LIS [33, 45, 54, 55] exhibits markedly distinct trends due to the absence of pinning. First, no hysteresis is observed during bridge extension or compression. Second, the variation in capillary force is substantially reduced thanks to the frictionless nature of the lubricant. Third, the small forces and absence of pinning allow gravity to break the bridge symmetry, an effect that is often masked by pinning on solid surfaces. On LIS, gravity can affect the apparent CA by altering the pressure balance within the capillary, in agreement with theoretical predictions. [35, 50] Finally, lubricant cloaking on LIS [43–45] reduces the effective surface tension and allows lubricant transport between the surfaces. The effect is most pronounced in asymmetric capillary bridges formed by a LIS and DMS, where lubricant transfer produces a ridge on the DMS surface, modifying capillary interactions and introducing localized pinning. Further work will focus on dynamic interactions between the lubricant and capillary bridges, particularly the evolution of oil ridges over time under mechanical deformation and varying pressures. Incorporating dynamic effects, such as lubricant viscosity and the velocity of capillary bridge extension-compression, would extend the predictive capability of the model to practical applications, including printing, coatings, cell culture, and microfluidics. Overall, this study establishes a fundamental framework that can help design functional liquid-like surfaces with tunable and controllable capillary interactions.

References

[1]M. Li, L. Shi, and X. Wang, "Physical mechanisms behind the wet adhesion: from amphibian toe-pad to biomimetics", Colloids and Surfaces B: Biointerfaces **199**, 111531 (2021).

[2]D. Tan, B. Zhu, K. Xiao, L. Li, Z. Shi, Q. Liu, S. Gorb, H. Gao, J. T. Pham, Z. Liu, and L. Xue, "Nanosized contact enables faster, stronger, and liquid-saving capillary adhesion", ACS Nano **19**, 8571–8578 (2025).

[3]D. J. Hornbaker, R. Albert, I. Albert, A.-L. Barabási, and P. Schiffer, "What keeps sandcastles standing?", Nature **387**, 765–765 (1997).

[4]M. Miot, G. Veylon, A. Wautier, P. Philippe, F. Nicot, and F. Jamin, "Numerical analysis of capillary bridges and coalescence in a triplet of spheres", Granular Matter **23**, 1–18 (2021).

[5]Y. Liu, P. Che, B. Zhang, J. Yang, H. Gao, J. Feng, Y. Wu, and L. Jiang, "One-step patterning of organic semiconductors on gold electrodes via capillary-bridge manipulation", ACS Applied Materials & Interfaces **14**, 32761–32770 (2022).

[6]M. Saadat, J. Yang, M. Dudek, G. Øye, and P. A. Tsai, "Microfluidic investigation of enhanced oil recovery: the effect of aqueous floods and network wettability", Journal of Petroleum Science and Engineering **203**, 108647 (2021).

[7]P. Zhang, Z. Chen, K. G. Brown, J. C. L. Meeussen, C. Gruber, A. C. Garrabrants, and D. S. Kosson, "Drying model of a high salt content cementitious waste form: effect of capillary forces and salt solution", Cement and Concrete Research **146**, 106459 (2021).

[8]S. Bian, C.-F. Tai, D. Halpern, Y. Zheng, and J. B. Grotberg, "Experimental study of flow fields in an airway closure model", Journal of Fluid Mechanics **647**, 391–402 (2010).

[9]E. O. Gabrielsson, Y. H. Jung, J. H. Han, D. J. Joe, D. T. Simon, K. J. Lee, and M. Berggren, "Autonomous microcapillary drug delivery system self-powered by a flexible energy harvester", Advanced Materials Technologies **6**, 2100526 (2021).

[10]O. H. Pakarinen, A. S. Foster, M. Paajanen, T. Kalinainen, J. Katainen, I. Makkonen, J. Lahtinen, and R. M. Nieminen, "Towards an accurate description of the capillary force in nanoparticle-surface interactions", Modelling and Simulation in Materials Science and Engineering **13**, 1175–1186 (2005).

[11]H.-J. Butt and M. Kappl, "Normal capillary forces", Advances in Colloid and Interface Science **146**, 48–60 (2009).

[12]J. Berthier, "Theory of wetting", in *Micro-drops and digital microfluidics (second edition)*, edited by J. Berthier (William Andrew Publishing, Jan. 1, 2013), pp. 7–73.

[13]M. Fan, Z. Fan, Z. Xu, J. Li, C. Li, and Z. Yang, "Investigation of capillary forces and capillary bridges between an end-adjusted three-finger microgripper with hydrophobic side surface and a plate", Journal of Adhesion Science and Technology **38**, 1702–1717 (2024).

[14]M. S. Rodrigues, R. C. V. Coelho, and P. I. C. Teixeira, "Dynamics of liquid bridges between patterned surfaces", Physica D: Nonlinear Phenomena **469**, 134322 (2024).

[15]E. Lee and F. Müller-Plathe, "Contact line friction and dynamic contact angles of a capillary bridge between superhydrophobic nanostructured surfaces", The Journal of Chemical Physics **157**, 024701 (2022).

[16]D. Daniel, C. L. Lay, A. Sng, C. J. Jun Lee, D. C. Jin Neo, X. Y. Ling, and N. Tomczak, "Mapping micrometer-scale wetting properties of superhydrophobic surfaces", Proceedings of the National Academy of Sciences **116**, 25008–25012 (2019).

[17]V. Liimatainen, M. Vuckovac, V. Jokinen, V. Sariola, M. J. Hokkanen, Q. Zhou, and R. H. A. Ras, "Mapping microscale wetting variations on biological and synthetic water-repellent surfaces", Nature Communications **8**, 1798 (2017).

[18]F. Cassin, R. Hahury, T. Lançon, S. Franklin, and B. Weber, "The nucleation, growth, and adhesion of water bridges in sliding nano-contacts", The Journal of Chemical Physics **158**, 224703 (2023).

[19]S. Cheng and M. O. Robbins, "Capillary adhesion at the nanometer scale", Physical Review E **89**, 062402 (2014).

[20]N. N. Nguyen, S. Davani, R. Asmatulu, M. Kappl, R. Berger, and H.-J. Butt, "Nano-capillary bridges control the adhesion of ice: implications for anti-icing via superhydrophobic coatings", ACS Applied Nano Materials **5**, 19017–19024 (2022).

[21]K. Tanaka, T. Ito, Y. Nishiyama, E. Fukuchi, and O. Fuchiwaki, "Double-nozzle capillary force gripper for cubical, triangular prismatic, and helical 1-mm-sized-objects", IEEE Robotics and Automation Letters **7**, 1324–1331 (2022).

[22]E. Portuguez, A. Alzina, P. Michaud, D. Hourlier, and A. Smith, "Study of the contact and the evaporation kinetics of a thin water liquid bridge between two hydrophobic plates", Advances in Materials Physics and Chemistry **7**, 99–112 (2017).

[23]Z. Shi, Y. Zhang, M. Liu, D. A. H. Hanaor, and Y. Gan, "Dynamic contact angle hysteresis in liquid bridges", Colloids and Surfaces A: Physicochemical and Engineering Aspects **555**, 365–371 (2018).

[24]E. J. De Souza, L. Gao, T. J. McCarthy, E. Arzt, and A. J. Crosby, "Effect of contact angle hysteresis on the measurement of capillary forces", Langmuir **24**, 1391–1396 (2008).

[25]L. Yang, M. Sega, and J. Harting, "Capillary-bridge forces between solid particles: insights from lattice boltzmann simulations", AIChE Journal **67**, e17350 (2021).

[26]H. Chen, A. Amirfazli, and T. Tang, "Modeling liquid bridge between surfaces with contact angle hysteresis", Langmuir **29**, 3310–3319 (2013).

[27]N. Nagy, "Capillary bridges on hydrophobic surfaces: analytical contact angle determination", Langmuir **38**, 6201–6208 (2022).

[28]J. Li, E. Ueda, D. Paulssen, and P. A. Levkin, "Slippery lubricant-infused surfaces: properties and emerging applications", Advanced Functional Materials **29**, 1802317 (2019).

[29]M. Villegas, Y. Zhang, N. Abu Jarad, L. Soleymani, and T. F. Didar, "Liquid-infused surfaces: a review of theory, design, and applications", ACS Nano **13**, 8517–8536 (2019).

[30]Y. Long, X. Yin, P. Mu, Q. Wang, J. Hu, and J. Li, "Slippery liquid-infused porous surface (SLIPS) with superior liquid repellency, anti-corrosion, anti-icing and intensified durability for protecting substrates", Chemical Engineering Journal **401**, 126137 (2020).

[31]J. Dawson, S. Coaster, R. Han, J. Gausden, H. Liu, G. McHale, and J. Chen, "Dynamics of droplets impacting on aerogel, liquid infused, and liquid-like solid surfaces", ACS Applied Materials & Interfaces **15**, 2301–2312 (2023).

[32]Y. Zhu, G. McHale, J. Dawson, S. Armstrong, G. Wells, R. Han, H. Liu, W. Vollmer, P. Stoodley, N. Jakubovics, and J. Chen, "Slippery liquid-like solid surfaces with promising antibiofilm performance under both static and flow conditions", ACS Applied Materials & Interfaces **14**, 6307–6319 (2022).

[33]T.-S. Wong, S. H. Kang, S. K. Y. Tang, E. J. Smythe, B. D. Hatton, A. Grinthal, and J. Aizenberg, "Bioinspired self-repairing slippery surfaces with pressure-stable omniphobicity", Nature **477**, 443–447 (2011).

[34]S. Hardt and G. McHale, "Flow and drop transport along liquid-infused surfaces", Annual Review of Fluid Mechanics **54**, 83–104 (2022).

[35]A. C. M. Shek, C. Semprebon, J. R. Panter, and H. Kusumaatmaja, "Capillary bridges on liquid-infused surfaces", Langmuir **37**, 908–917 (2021).

[36]R. Deng, L. Yang, and C. D. Bain, "Combining inkjet printing with emulsion solvent evaporation to pattern polymeric particles", ACS Applied Materials & Interfaces **10**, 12317–12322 (2018).

[37]B. V. Orme, G. McHale, R. Ledesma-Aguilar, and G. G. Wells, "Droplet retention and shedding on slippery substrates", Langmuir **35**, 9146–9151 (2019).

[38]S. J. Goodband, S. Armstrong, H. Kusumaatmaja, and K. Voïtchovsky, "Effect of ageing on the structure and properties of model liquid-infused surfaces", Langmuir **36**, 3461–3470 (2020).

[39]S. Goodband, H. Kusumaatmaja, and K. Voïtchovsky, "Development of a setup to characterize capillary liquid bridges between liquid infused surfaces", AIP Advances **12**, 015120 (2022).

[40]K. A. Brakke, "The surface evolver", Experimental Mathematics **1**, 141–165 (1992).

[41]J. Bowen and D. Cheneler, "Closed-form expressions for contact angle hysteresis: capillary bridges between parallel platens", Colloids and Interfaces **4**, 13 (2020).

[42]H. Kusumaatmaja and J. M. Yeomans, "Modeling contact angle hysteresis on chemically patterned and superhydrophobic surfaces", Langmuir **23**, 6019–6032 (2007).

[43]A. A. Günay, S. Sett, Q. Ge, T. Zhang, and N. Miljkovic, "Cloaking dynamics on lubricant-infused surfaces", Advanced Materials Interfaces **7**, 2000983 (2020).

[44]F. Schellenberger, J. Xie, N. Encinas, A. Hardy, M. Klapper, P. Papadopoulos, H.-J. Butt, and D. Vollmer, "Direct observation of drops on slippery lubricant-infused surfaces", Soft Matter **11**, 7617–7626 (2015).

[45]J. D. Smith, R. Dhiman, S. Anand, E. Reza-Garduno, R. E. Cohen, G. H. McKinley, and K. K. Varanasi, "Droplet mobility on lubricant-impregnated surfaces", Soft Matter **9**, 1772–1780 (2013).

[46]K. G. Pepper, C. Bahrim, and R. Tadmor, "Interfacial tension and spreading coefficient of thin films: review and future directions", Journal of Adhesion Science and Technology **25**, 1379–1391 (2011).

[47]J. D. Berry, M. J. Neeson, R. R. Dagastine, D. Y. C. Chan, and R. F. Tabor, "Measurement of surface and interfacial tension using pendant drop tensiometry", Journal of Colloid and Interface Science **454**, 226–237 (2015).

[48]A. Daerr and A. Mogne, "Pendent_drop: an ImageJ plugin to measure the surface tension from an image of a pendent drop", Journal of Open Research Software **4**, e3 (2016).

[49]M. R. Gunjan, A. Kumar, and R. Raj, "Cloaked droplets on lubricant-infused surfaces: union of constant mean curvature interfaces dictated by thin-film tension", Langmuir **37**, 6601–6612 (2021).

[50]C. Semprebon, M. S. Sadullah, G. McHale, and H. Kusumaatmaja, "Apparent contact angle of drops on liquid infused surfaces: geometric interpretation", Soft Matter **17**, 9553–9559 (2021).

[51]C. Semprebon, G. McHale, and H. Kusumaatmaja, "Apparent contact angle and contact angle hysteresis on liquid infused surfaces", Soft Matter **13**, 101–110 (2016).

[52]K. Takamura, H. Fischer, and N. R. Morrow, "Physical properties of aqueous glycerol solutions", Journal of Petroleum Science and Engineering **98-99**, 50–60 (2012).

[53]E. J. De Souza, M. Brinkmann, C. Mohrdieck, A. Crosby, and E. Arzt, "Capillary forces between chemically different substrates", Langmuir **24**, 10161–10168 (2008).

[54]M. S. Sadullah, J. R. Panter, and H. Kusumaatmaja, "Factors controlling the pinning force of liquid droplets on liquid infused surfaces", Soft Matter **16**, 8114–8121 (2020).

[55]A. Lafuma and D. Quéré, "Slippery pre-suffused surfaces", Europhysics Letters **96**, 56001 (2011).

Chapter 5

Droplet removal by capillary lifting

In this chapter, we harness interfacial capillarity to remove droplets from surfaces, representing an inverse process to adhesion. A rising working liquid contacts the deposited droplet and forms a capillary bridge, which stretches and deforms as the injected liquid continues to rise. This method exploits the high interfacial tension of the working liquid (*e.g.* water), eliminating the need for surfactants and enabling effective and sustainable removal of unwanted droplets. The bridge morphology and dewetting process are visualised through experiments and simulations, and interpreted using a simple theoretical framework that predicts dewetting performance based on the interfacial properties of the system. This chapter demonstrates how the subtle yet powerful capillary force can be harnessed for future liquid manipulation and surface cleaning technologies.

5.1 Abstract

The removal of liquid droplets from solid surfaces is central to cleaning, coatings and oil recovery. Here we investigate liquid droplets lifted by capillarity from surfaces by an immiscible working liquid. The rising working liquid triggers the formation of a capillary bridge between the droplet–solid and the droplet–air interfaces, which can lead to full, partial, or no droplet dewetting (Fig. 5.1). Our theoretical model predicts, and experiments confirm, that the effectiveness of droplet removal can be tuned by manipulating the droplet contact angle with the solid and the interfacial tensions at play. Significantly, dewetting can be enhanced by employing working liquids with high interfacial tension, in contrast to common surface cleaning strategies where surfactants are used to reduce interfacial tension. Our findings can open new avenues for droplet manipulation with reduced resources and more sustainable environmental impact.

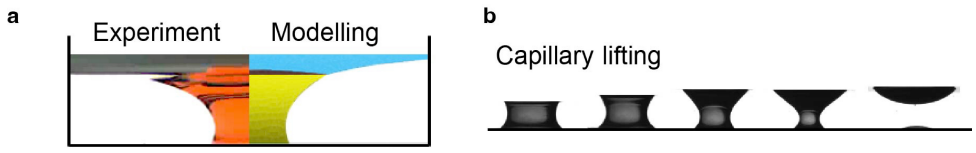

Figure 5.1: **(a)** Capillary-driven droplet removal in experiment and modelling. **(b)** Evolution of the capillary bridge during dewetting and removal.

5.2 Introduction

Droplet dewetting refers to the process where a liquid droplet retracts its contact from a solid surface. The phenomenon is central to a wide range of engineering and industrial applications, including self-cleaning surfaces [1], inkjet printing [2], and surface patterning [3, 4]. To date, most studies of droplet dewetting focus on binary fluid systems whereby the droplet is surrounded by air or an immiscible liquid. In such cases, a large body of literature has shown that liquid retraction can be driven by several mechanisms, such as the droplet interfacial energy in the case of droplet impact [5], spinodal dewetting [6], loss of volume in the case of evaporation [7] or change of effective contact angle due to external fields [8, 9].

In contrast, significant gaps remain in our understanding of dewetting in ternary systems, which involve three fluid components and a solid. Yet ternary dewetting is arguably more common than its binary counterpart, observed when a working liquid is used to induce droplet retraction, including for advanced oil recovery (immiscible water-alternating-gas displacement process) [10], surface coatings [4], hair dyeing [11] and various forms of surface cleaning [1, 12–14]. Moreover, in surface cleaning, there are strong economic and environmental pressures to devise new ways to displace soils (liquids or other forms of contaminants) from surfaces using less water, energy and surfactants. [15–17] This is further compounded by the emerging global water scarcity [18] and the toxicity and low degradability of synthetic surfactants [19, 20].

In this study, we explore a fundamental mechanism of ternary dewetting that we term capillary lifting, where a 'soil' droplet surrounded by air is lifted from the surface of a solid by a working liquid. Through a combination of experiments and simulations, we demonstrate the efficiency of capillary lifting across a wide range

of liquids and substrates. Significantly, our results show that dewetting is favoured when the working liquid has a high interfacial tension, enabling the capillary force to effectively lift the droplet. This is different to conventional cleaning methods that employ surfactants to reduce the interfacial tensions. We then propose a simple yet predictive model that describes the transition between dewetting and non-dewetting. Building on this, we extend our capillary lifting study to formulated working liquid and chemically heterogeneous soils, demonstrating its potential relevance for real-world systems. Our findings reveal capillary lifting as an effective droplet dewetting method that requires minimal resources (energy, water, surfactant) input, offering a more sustainable approach for droplet manipulation in ternary systems.

5.3 Methods

5.3.1 Experimental methods

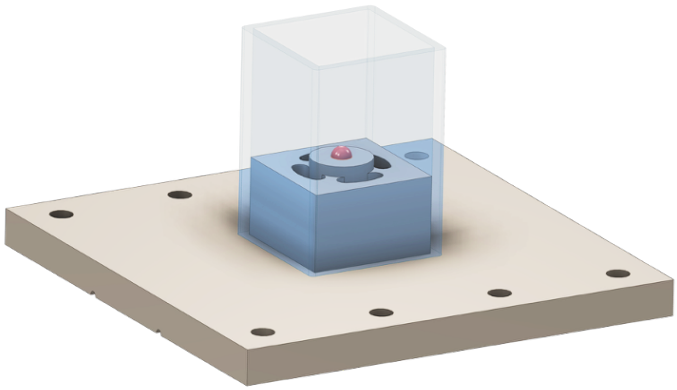

Figure 5.2: 3D drawing of the bespoke droplet dewetting device developed for this study. The central substrate (*e.g.*, stainless steel, as shown) holds the soil droplet, while the working fluid is injected from below through four symmetric holes, ensuring uniform distribution.

Substrate and device preparation. Before each experiment, substrates and the dewetting device are cleaned sequentially with deionised water, isopropanol, and deionised water again, followed by drying with nitrogen gas. The fluid device features a central stage for substrate attachment, surrounded by four symmetric holes around it to ensure uniform fluid distribution (see Fig. 5.2). A 10 μL droplet is deposited on the substrate, and the working fluid is injected at a rate of 0.02 mL/min using a

syringe pump (Pump 11 Pico Plus Elite, Harvard Apparatus, Massachusetts, US), corresponding to a liquid rise velocity of 5.33×10^{-7} m/s. The device base measures 25 × 25 mm and is capped with either a borosilicate (CM Scientific Ltd., Silsden, UK) or acrylic cubic square tube for visualisation.

Imaging. The dewetting process was captured using: A colour digital camera (GV-79L0WP-C-HQ, IDS Imaging, Obersulm, Germany) with a 35 mm HP series lens (Edmund Optics Ltd., York, UK); A mono digital camera (UI-3880CP-M-GL Rev. 2, IDS Imaging, Obersulm, Germany) with a 6.5× zoom lens (MVL6X12Z, Thorlabs, New Jersey, US) and a 0.5× magnifying lens (MVL6X05L, Thorlabs, New Jersey, US). Lighting is provided by either an LED (RALENO, Amazon, UK) or a torch (ICEFIRE, Amazon, UK), coupled with a diffusive screen to ensure uniform illumination.

Materials. Substrates include stainless steel (SPI Supplies, West Chester, US), glass (LaboQuip, London, UK), poly(methyl methacrylate) (PMMA, Sheet Plastics, Leicester, UK), polycarbonate (PC, Sheet Plastics, Leicester, UK), and polytetrafluoroethylene (PTFE, Merck, Sigma-Aldrich, Gillingham, UK). Liquids used are deionised water (18.2 $M\Omega \cdot cm$, Merck-Millipore, Hertfordshire, UK), tetradecane (Merck, Sigma-Aldrich, Gillingham, UK), decane (Merck, Sigma-Aldrich, Gillingham, UK), silicone oil (10 cSt, Merck, Sigma-Aldrich, Gillingham, UK), olive oil (Solesta, Aldi, Essen, Germany), squalane (Merck, Sigma-Aldrich, Gillingham, UK), and isopropanol (99.5% for HPLC, Thermo Scientific^{TM}, Cambridge, UK). For visualisation in Fig. 5.4, tetradecane droplets are dyed with Sudan IV (Merck, Sigma-Aldrich, Gillingham, UK) at a concentration of 1 mg in 6 mL, while water droplets are dyed with fluorescein sodium salt (Merck, Sigma-Aldrich, Gillingham, UK) at a concentration of 100 ppm. The formulation is composed of tripropylene glycol methyl ether 0.45 wt%, diethylene glycol hexyl ether 0.45 wt%, ethylene glycol hexyl ether 0.45 wt%, and deionised water.

Interfacial measurements. Interfacial tensions were measured using the pendant drop method for binary systems and the Neumann triangle analysis for ternary systems (Fig. 5.3). In the binary configuration, a liquid droplet is suspended from a needle into another immiscible fluid. The equilibrium droplet shape results from

the balance between interfacial tension and gravitational forces, and the interfacial tension is obtained by fitting the droplet profile to the Young–Laplace equation. For ternary systems consisting of three immiscible phases (typically a droplet, the working fluid, and the surrounding air), the interfacial tensions were determined using the Neumann triangle method. In this case, the interfacial tension ratios are extracted from the equilibrium contact angles formed at the three-phase junction, satisfying the vector balance of interfacial tensions.

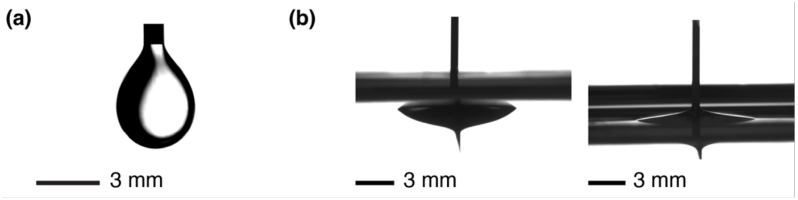

Figure 5.3: Interfacial tension measurements in binary and ternary systems. Binary systems were measured using the pendant drop method, and ternary systems using the Neumann triangle method. **(a)** Pendant drop measurement of a tetradecane droplet suspended in the formulated working fluid. **(b)** Neumann triangle analysis of a tetradecane droplet floating as a liquid lens at the interface between the formulated working fluid and air.

Contact angle hysteresis. In contact angle hysteresis (advancing and receding angles) measurements, droplets were deposited on the substrates while immersed in the working liquid, and the droplet was injected and withdrawn obtain advancing and receding angles (Table 5.1). Measurements under liquid are inherently much more challenging than measurements in air due to droplet mobility upon needle contact, non-uniform pinning along the contact line, gravitational deformation, and substrate heterogeneity across different measurement locations. These factors contribute to the relatively large uncertainties. In Table 5.1, the advancing and receding angles were determined directly from video frames at the moments when the contact line was advancing or receding, with standard deviations calculated from three repeated measurements.

Table 5.1: Advancing and receding contact angle measurements in the surrounding liquid. All measurements were repeated at least three times to determine the standard deviation.

Surface	Droplet	Surrounding liquid	Advancing angle (°)	Receding angle (°)
Stainless Steel	Tetradecane	Water	118.2 ± 6.5	37.0 ± 7.1
Stainless Steel	Decane	Water	125.1 ± 6.0	53.4 ± 5.8
Stainless Steel	Tetradecane	Formulation	118.7 ± 3.9	30.8 ± 1.4
Glass	Decane	Water	132.6 ± 5.6	65.8 ± 1.3
Glass	Tetradecane	Water	132.2 ± 5.5	57.9 ± 1.4
Glass	Silicone oil	Water	129.2 ± 6.5	118.7 ± 4.9
Glass	Water (fluorescein dyed)	Tetradecane	81.2 ± 8.2	75.5 ± 11.3
PTFE	Tetradecane	Water	28.2 ± 3.4	13.0 ± 2.0
PTFE	Tetradecane	Formulation	32.0 ± 9.8	25.0 ± 4.8
PTFE	Decane	Water	26.0 ± 3.6	15.2 ± 2.0
PTFE	Decane	Formulation	65.1 ± 4.4	40.4 ± 2.8
PMMA	Water (fluorescein dyed)	Tetradecane	98.6 ± 8.9	88.5 ± 3.1
PMMA	Tetradecane	Formulation	106 ± 20.3	130.0 ± 4.6
PMMA	Tetradecane	Water	126.5 ± 7.0	55.6 ± 8.1
PMMA	Squalane	Water	119.6 ± 3.8	59.6 ± 6.0
PMMA	Olive oil	Water	113.0 ± 16.8	50.5 ± 6.0
PMMA	Decane	Water	89.1 ± 6.1	59.6 ± 4.4
PMMA	Tetradecane (Sudan IV dyed)	Water	81.1 ± 11.1	71.7 ± 12.2
PC	Tetradecane	Formulation	113.6 ± 9.4	50.2 ± 4.3
PC	Tetradecane	Water	73.9 ± 8.9	19.9 ± 3.7
PC	Decane	Water	78.0 ± 2.0	22.2 ± 5.1

5.3.2 Simulation method

We employed Surface Evolver [21] to model the dewetting behaviour of a droplet lifted from a solid substrate by an invading fluid under quasi-static conditions. In Surface Evolver, each surface or interface is discretised into triangular facets, and interfacial tensions are assigned based on experimental measurements obtained via techniques such as the pendant drop method or Neumann triangle analysis.

For the solid substrate and side walls, we ensured the chosen interfacial tensions obey the Young's equation. For the droplet on the solid substrate, the relation is given by: $\gamma_{sd} = \gamma_{sl} - \gamma_{dl}\cos\theta_{dl}$, where γ_{sd}, γ_{sl}, γ_{dl} represent the interfacial tensions (or energies) for the solid-droplet, solid-liquid (working fluid), and droplet-liquid (working fluid) interfaces, respectively. θ_{dl} is the receding contact angle of the droplet on the substrate in the presence of the working fluid. The receding contact angle θ_{dl} used in the simulations was obtained from capillary bridge retraction experiments and is consistent with the measured contact angle hysteresis (Table 5.1), within experimental variability. This ensures that the model uses physically representative contact angles. For the working liquid on the side walls, the contact angle is set to $\theta_{lw} = 90°$, such that $\gamma_{lw} = \gamma_{wg} - \gamma_{lg}\cos\theta_{lw}$ leads to $\gamma_{lw} = \gamma_{wg}$, where γ_{lw} and γ_{wg} refer to the interfacial tensions (or energies) for the liquid-wall and wall-gas interfaces, respectively. See details in Fig. 5.4a.

In the model, measured interfacial tensions γ_{dg} and γ_{dl} are normalised by γ_{lg} before being input into the simulation, with γ_{sl}/γ_{lg} and γ_{wg}/γ_{lg} set to 1. Densities are normalised by the density of the working liquid. To match the experimental conditions, the gravitational strength g is set by matching the Bond number (Bo) of the experiment. The droplet volume remains constant, consistent with experimental conditions. The initial volume of the invading fluid is set to establish a stable liquid bridge between the air and the substrate. The fluid is then added incrementally, followed by energy minimisation at each step. The equilibrium state from each step serves as the initial condition for the next, simulating the continuous invasion process under quasi-static conditions.

5.4 Results and discussion

5.4.1 Typical quasi-equilibrium dewetting and non-dewetting trajectories

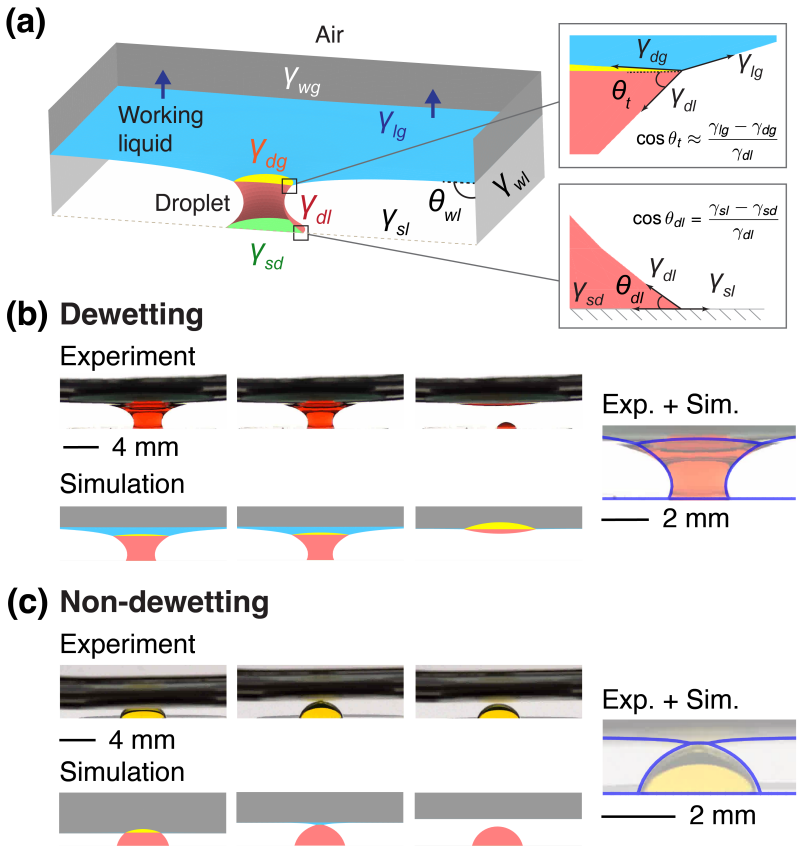

Figure 5.4: Capillary lifting of a droplet from a surface by a rising working liquid. **(a)** Schematic diagram of a soil droplet being lifted from a solid substrate by a rising working liquid. The relevant thermodynamic parameters are the interfacial tensions (or energies) of the solid substrate-droplet γ_{sd} (green), droplet-gas γ_{dg} (yellow), liquid-gas γ_{lg} (blue), substrate-liquid γ_{sl} (white), droplet-liquid γ_{dl} (red), liquid-wall γ_{lw} (white), and wall-gas γ_{wg} (grey). The receding contact angle of the droplet in liquid is θ_{dl}, and the effective top contact angle is θ_t, which can be expressed in terms of the balance of interfacial tensions (see insets). **(b-c)** Examples of capillary lifting observed experimentally and in simulations for two typical situations. (b) Dewetting of a dyed tetradecane droplet on a polymethyl methacrylate (PMMA) surface by water. (c) No dewetting observed for a dyed water droplet on PMMA upon addition of tetradecane. In (b-c), combined simulation and experimental results are shown with the simulated profiles as blue lines atop the experimental results.

We designed a fluidic device (see Fig. 5.2) to investigate the dewetting behaviour. The droplet ($\sim$ 10 μL) experiences the slow rise of the working liquid from the

surface of the solid (see experimental details in the Methods Section 5.3.1). The rise velocity is typically $\sim 5 \times 10^{-7}$ m/s. At such a small velocity, the system follows a quasi-equilibrium trajectory. As the working liquid contacts the droplet, the latter can be lifted due to capillary effects and fully or partially dewet from the surface (Fig. 5.4b). Alternatively, it can remain bound to the surface (Fig. 5.4c).

To quantify the extent of droplet removal, we define the dewetting percentage (Dewet, %) as the fraction of droplet volume removed from the solid surface, Dewet $(\%) = (V_0 - V_r)/V_0 \times 100$, where V_0 is the initial droplet volume prior to contact with the working liquid, and V_r is the residual droplet volume remaining on the surface after interaction. V_r is calculated from the measured droplet residue geometry assuming a spherical-cap shape. From Figs. 5.4b–c, we observe that water can remove $> 90\%$ of a tetradecane droplet ($\theta_{dl} = 64.8°$), whereas tetradecane cannot displace a water droplet ($\theta_{dl} = 76.4°$). This observation may seem surprising since tetradecane exhibits near-complete wetting on PMMA in air (contact angle $\sim 0°$) while water droplets show a significantly higher contact angle of $71 \pm 4°$ (Fig. 5.5). Tetradecane therefore has the strongest affinity for PMMA. The key to understanding this apparent contradiction is that effective capillary lifting requires a high interfacial tension for the working liquid. Here, water has a significantly higher interfacial tension (72 mN/m) than tetradecane (26.56 mN/m). Thus, for such ternary dewetting, the use of surfactants and other small molecules to reduce interfacial tension, ubiquitous in conventional surface cleaning strategies, can actually degrade performance. The fact that the capillary lifting mechanism benefits from the absence of surfactants opens an effective avenue for an alternative droplet removal and manipulation approach that is more sustainable and environmentally friendly.

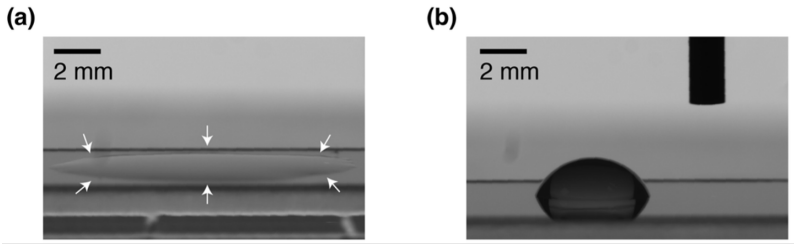

Figure 5.5: Contact angle measurements of $\sim 10\ \mu$L droplets on polymethyl methacrylate (PMMA) substrates: **(a)** tetradecane and **(b)** water. Tetradecane exhibits near-complete wetting on PMMA, corresponding to a contact angle of approximately 0°. White arrows indicate the droplet boundary profile to aid visualisation. In contrast, the water droplet on PMMA in air shows a contact angle of $71.2 \pm 3.9°$, measured using the LBADSA method [22].

This finding raises several questions. First, what are the key parameters controlling the lifting mechanism and its efficiency? Second, is the transition between a dewetting (Fig. 5.4b) and non-dewetting situation (Fig. 5.4c) continuous when varying the balance of interfacial energies between the media. Third, can the capillary lifting mechanism be extended to real-world complex soils that are chemically heterogeneous? To better understand the capillary lifting mechanism, we complement our experiments with computer modelling using Surface Evolver [21]. Since the capillary length (1.87 to 4.94 mm for fluid systems in this chapter) is comparable to the soil droplet size ($\sim 10\ \mu$L), gravitational force is included in our analysis together with the relevant interfacial tensions (see details in Fig. 5.6). The total energy of the system can be expressed as:

$$E_{\text{Total}} = \sum_{i,j} \gamma_{ij} A_{ij} + g \sum_{k} \int_{V_k} \rho_k z \, dV \tag{5.1}$$

where γ_{ij} represents interfacial tensions between two phases i and j, A_{ij} is the corresponding interfacial area, and the sum over i, j is taken over all unique interfaces (each interface counted once). g is the gravitational acceleration, z is the vertical coordinate, ρ_k and V_k denote densities and volumes of the fluids involved in the system. For simplicity, we take a quasi-static approximation, corresponding to the limit of $\text{Ca} \to 0$ (typically, $\text{Ca} \sim 10^{-8}$ in our experiments and we do not observe significant dynamic effects for $\text{Ca} < 10^{-3}$). In this limit, we slowly and incrementally increase the volume of the invading working liquid and carry out energy minimization

for each corresponding volume (see the Methods Section 5.3.2 for additional details of the numerical scheme). The simulated evolutions of the interface configuration agree well with experiments, as shown in Figs. 5.4b-c.

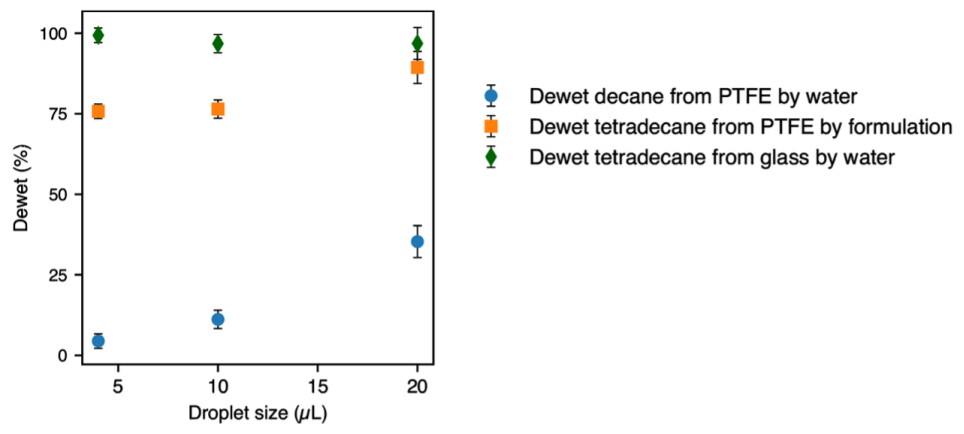

Figure 5.6: Influence of droplet size on dewetting behaviour. The increased dewetting for larger droplets indicates that gravity cannot be neglected. This trend is expected, as the droplets in these systems are less dense than the working liquid, allowing gravity to enhance dewetting for larger droplets. In systems exhibiting near complete dewetting (green), the effect of droplet size becomes negligible. This is because the system is already in a fully dewetting regime therefore the contribution of gravity is minimised.

5.4.2 Dewetting regime diagrams

Experimentally, we investigated soil droplets from pure liquids such as tetradecane and water to real-world contaminants including squalane (used in cosmetics and base oil lubricant), olive oil, and used engine oil. For the working fluid, we used either pure liquids or low-concentration glycol ether formulation relevant to industrial applications (0.45 wt% tripropylene glycol methyl ether, 0.45 wt% diethylene glycol hexyl ether and 0.45 wt% ethylene glycol hexyl ether in water). We tested capillary lifting on a range of commercial substrates with different surface energies, including polytetrafluoroethylene (PTFE), polycarbonate (PC), polymethyl methacrylate (PMMA), glass, and stainless steel. The corresponding interfacial tensions and static contact angles were experimentally determined using pendant drop and sessile drop methods, as described in Methods Section 5.3.1. The measured static contact angles of droplets surrounded by working fluid (Fig. 5.7a) demonstrate the wide range of surface wettability covered by the selected substrates. It should be noted that the

static contact angles in Fig. 5.7 are used only as a qualitative measure of wettability, whereas the receding contact angle θ_{dl} is used in the model and quantitative analysis. Higher static contact angles correspond to weaker droplet adhesion, promoting more dewetting behaviour, which is consistent across all systems examined (Fig. 5.7b). The measured interfacial tensions are summarised in Table 5.2.

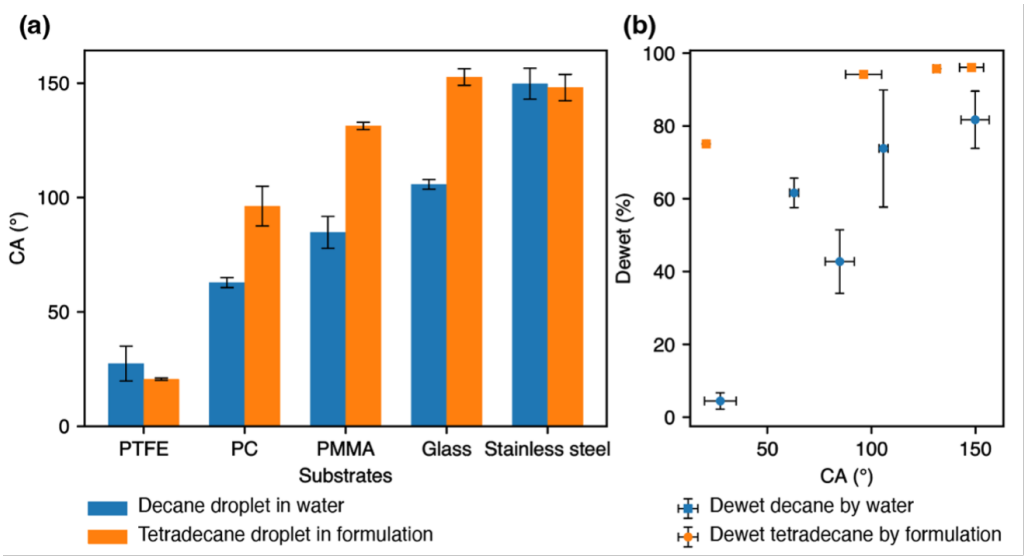

Figure 5.7: Measured static contact angles and dewetting outcomes for the investigated surfaces in two example systems: dewetting decane by water and dewetting tetradecane by the formulation. **(a)** Static contact angles of droplets on various substrates surrounded by the working fluid. **(b)** The dewetting behaviour of droplets as a function of static contact angle.

Fig. 5.8 summarizes the dewetting outcome for our simulations and experiments for wide-ranging systems. From Fig. 5.8a, it is clear that the dewetting and non-dewetting regions follow a trend that can be described theoretically as a function of θ_{dl} and θ_t (see Fig. 5.4a). This can be rationalised from simple geometrical considerations by analogy with capillary bridges. When a three-phase contact line is present, bridge stability is determined by the contact angles on the top and bottom substrates, here by analogy θ_{dl} and θ_t. Dewetting is favoured when $\cos\theta_{dl} < \cos\theta_t$ (bottom right corner in Fig. 5.8a), as the bottom contact radius vanishes faster than the top contact radius. [23, 24] This simple approximation yields excellent agreement between experiments, simulations, and theory, though small deviations appear near the boundary line due to slight curvature of the droplet–air and liquid–air interfaces. The theoretical line in the regime diagram (Fig. 5.8a) corresponds

Table 5.2: Measured interfacial tensions.

Phase I	Phase II	Interfacial tension (mN/m)	Standard deviation (mN/m)
Air	Tetradecane	26.56	0.85
	Decane	23.62	0.32
	Formulation	28.30	0.30
	Olive oil	32.73	0.75
	Squalane	26.14	0.58
	Water (fluorescein dyed)	73.36	0.91
	Tetradecane (Sudan IV dyed)	24.52	0.24
	Silicone oil	19.48	0.26
Water	Tetradecane	45.20	1.37
	Decane	36.67	0.39
	Tetradecane (Sudan IV dyed)	42.33	0.17
	Olive oil	35.06	1.41
	Squalane	46.11	1.54
	Silicone oil	35.22	0.57
Tetradecane	Water (fluorescein dyed)	36.82	2.76
	Formulation	18.15	0.38

to $\cos\theta_{dl} = \cos\theta_t$, where $\cos\theta_t \approx (\gamma_{lg} - \gamma_{dg})/\gamma_{dl}$. This geometrical model assumes flat liquid–air and droplet–air interfaces, whereas in practice these interfaces are slightly curved. As shown in Fig. 5.9, this leads to deviations of less than 10° near the transition between dewetting and non-dewetting regimes. However, the overall behaviour remains consistent with the theoretical prediction in Fig. 5.8a, with this small deviation introducing a minor correction. Apart from this minor deviation between simulation and theory, another clear outlier (blue arrow in Fig. 5.8a) was observed when a formulated solution, rather than a pure liquid, was used as the working fluid. This deviation can be explained by molecular migration, which will be discussed later in Fig. 5.10.

The regime maps obtained from the capillary lifting mechanism are shown in Figs. 5.8b–e, illustrating the dewetting and non-dewetting transitions in the parameter space of interfacial tension ratios γ_{dl}/γ_{lg} and γ_{dg}/γ_{lg} for four different values of θ_{dl}. For each map, six distinct regions can be broadly identified. The corresponding liquid morphologies for representative states are shown in Fig. 5.8f. In regime I

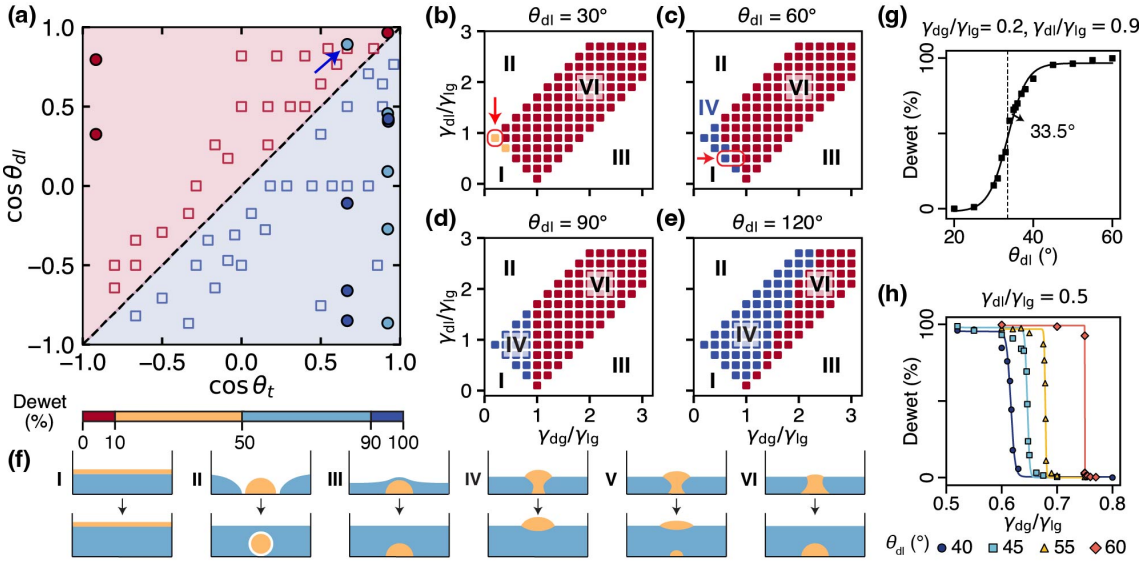

Figure 5.8: Experimental and simulated dewetting regime diagrams across various interfacial systems. **(a)** Ternary dewetting simulations (□) and experiments (●) shown as a function of the droplet apparent contact angle at the droplet–air interface (θ_t) and the droplet–solid interface (θ_{dl}). The background colour indicates the theoretical prediction for dewetting ($\cos\theta_t > \cos\theta_{dl}$) and non-dewetting ($\cos\theta_t < \cos\theta_{dl}$). The colour for the experimental data points indicates the level of dewetting achieved. **(b-e)** Simulations detailing the dewetting phase diagrams across a range of θ_{dl} and interfacial tensions γ_{dg} (droplet-gas), γ_{dl} (droplet-liquid), and γ_{lg} (liquid-gas). **(f)** Schematics of the six droplet morphology regimes, showing the droplets in yellow, the working fluid in blue, and the air in white. **(g)** Dewetting behaviour for an interfacial system ($\gamma_{dg}/\gamma_{lg} = 0.2$, $\gamma_{dl}/\gamma_{lg} = 0.9$, red arrow in (b)) as a function of θ_{dl}. **(h)** Transition boundary from dewetting to non-dewetting at $\gamma_{dl}/\gamma_{lg} = 0.5$ with varying γ_{dg}/γ_{lg}. Results for different θ_{dl} are shown, including for $\theta_{dl} = 60°$ (red arrow in (c)).

($\gamma_{dg} + \gamma_{dl} < \gamma_{lg}$), the soil droplet completely spreads, forming a film at the working liquid-gas interface. In II ($\gamma_{dg} + \gamma_{lg} < \gamma_{dl}$), an anti-bubble forms whereby the soil droplet is cloaked by the air, which in turn is surrounded by the invading liquid. In III ($\gamma_{dl} + \gamma_{lg} < \gamma_{dg}$), the droplet disfavours contact with the gas phase and always remains attached to the solid substrate. In regimes I–III, where complete spreading occurs or an anti-bubble is formed, a three-phase contact line is not present and θ_t is therefore not defined; these cases are not described by the θ_t–θ_{dl} criterion. In IV, V and VI, the three fluid interfaces can form a Neumann triangle, and a capillary bridge is formed between the droplet–solid interface and the droplet–air interface. The droplet can dewet, as previously illustrated in Fig. 5.4b, and we can further distinguish whether we find full (IV) or partial (V) dewetting. In VI, the droplet does not dewet from the surface. These regimes follow the θ_t–θ_{dl} criterion: (IV)

$\cos\theta_{dl} < \cos\theta_t$, (V) near the transition, and (VI) $\cos\theta_{dl} > \cos\theta_t$.

Importantly, we find that dewetting can occur for droplet contact angles significantly lower than 180°. Additionally, as θ_{dl} increases, the droplet is more likely to dewet across various interfacial tension ratios (Figs. 5.8b-e and Fig. 5.7b). This is expected since higher θ_{dl} indicates a lower interfacial energy between the working liquid and the surface, compared to the droplet. Dewetting is also preferred for lower γ_{dg} and higher γ_{lg}, which effectively lower θ_t, as they destabilise the submerged droplet and stabilise the liquid lens geometry.

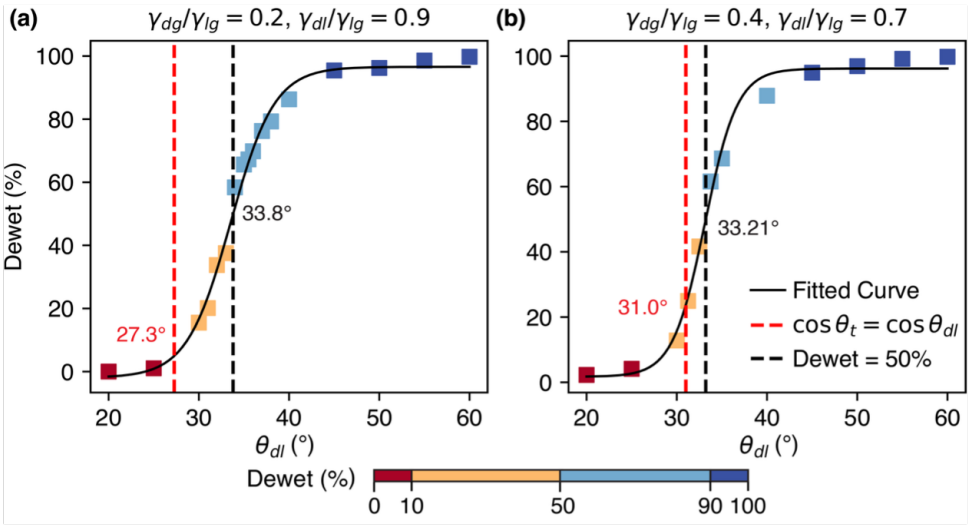

Figure 5.9: Dewetting and non-dewetting boundaries for fixed interfacial systems. **(a)** $\gamma_{dg}/\gamma_{lg} = 0.2$, $\gamma_{dl}/\gamma_{lg} = 0.9$; and **(b)** $\gamma_{dg}/\gamma_{lg} = 0.4$; $\gamma_{dl}/\gamma_{lg} = 0.7$. The bottom effective contact angle θ_{dl} is varied, and the data points are fitted with a hyperbolic tangent function. The theoretical boundary, defined by $\cos\theta_t = \cos\theta_{dl}$, is shown as a red dashed line, while the simulation predicted 50% dewetting threshold is indicated by a black dashed line. The deviation between these two boundaries is less than 10°.

We now focus on the sharpness of the boundary between full and non-dewetting as predicted by the computational model. When all interfacial tensions are held fixed (arrow in Fig. 5.8b), the transition typically follows a smooth hyperbolic tangent profile when varying the θ_{dl} (Fig. 5.8g). In contrast, when θ_{dl} is held constant and the interfacial tension ratio γ_{dg}/γ_{lg} varies (arrow in Fig. 5.8c), the transition becomes more abrupt and sharpens further with increasing θ_{dl} (Fig. 5.8h). These findings suggest that efficient dewetting can be achieved at relatively low contact angles by tuning interfacial tensions in a ternary system. For instance, abrupt dewetting transitions can be triggered by a slight decrease of γ_{dg}/γ_{lg}.

One important assumption of the model is that of perfectly smooth and homogeneous surfaces. However, experimentally most surfaces exhibit some roughness and chemical heterogeneities. As a result, we typically observe contact line pinning which leads to residues remaining on the surface upon dewetting and a slight deviation in the percentage of removal between experiments and simulations (Fig. 5.4b and Table 5.3). Partial dewetting is more prominent in the experiments than in the simulations.

Table 5.3: Measured dewetting results (mean ± SD, from three repeated measurements) and simulation predictions.

Droplet	**Working liquid**	**Substrate**	**Experiment dewet ± SD (%)**	**Simulation predicted dewet (%)**
Decane	Water	PTFE	4.45 ± 2.25	0
Decane	Water	Stainless steel	81.69 ± 7.83	100
Decane	Water	PC	61.59 ± 4.05	100
Decane	Water	PMMA	86.14 ± 3.63	100
Decane	Water	Glass	73.82 ± 15.04	100
Tetradecane	Formulation	PTFE	78.87 ± 3.11	100
Tetradecane	Formulation	Stainless steel	96.06 ± 0.47	100
Tetradecane	Formulation	PC	94.16 ± 7.83	100
Tetradecane	Formulation	PMMA	95.72 ± 0.44	100
Tetradecane	Water	PMMA	92.11 ± 0.42	100
Tetradecane	Water	Glass	96.77 ± 1.46	100
Tetradecane (Sudan IV dyed)	Water	PMMA	93.35 ± 1.40	100
Silicone oil	Water	Glass	88.30 ± 5.79	100
Squalane	Water	PMMA	79.14 ± 5.24	100
Olive oil	Water	PMMA	90.98 ± 4.77	100
Water (fluorescein dyed)	Tetradecane	PMMA	0 ± 0	0
Water (fluorescein dyed)	Tetradecane	Glass	0 ± 0	0

5.4.3 Capillary lifting with formulated working liquid and real-world soils

Another important aspect of surface cleaning is the common use of water-based formulations to enhance outcomes in binary systems. For comparison, we conducted capillary lifting experiments of tetradecane droplets from a PTFE substrate using the low-concentration glycol ether formulation (Fig. 5.10a). The interfacial tensions γ_{lg} and γ_{dl} were experimentally measured via the pendant drop (Fig. 5.3a), which is commonly applied to binary fluid systems. However, unlike for the pure liquid systems, when these interfacial tensions are input into the model, the predicted outcomes diverge significantly from experimental results (see panels 1–2 in Fig. 5.10a). The associated dewetting prediction for this system is the outlier data point highlighted in Fig. 5.8a, confirming that simple pairwise interfacial tension-based predictions for pure liquids no longer hold for complex ternary systems. The insufficiency of pairwise tensions suggests that additional mechanisms are at play.

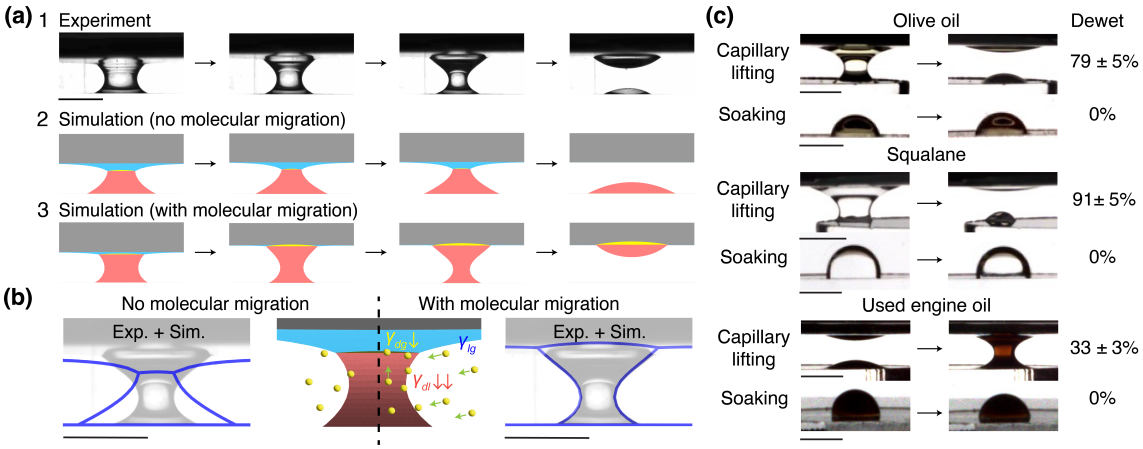

Figure 5.10: Capillary lifting mechanism in complex systems where droplets or working fluids are not chemically pure. **(a)** Dewetting using a low-concentration formulation as the working liquid. Simulations using binary interfacial tensions fail to capture the experimental profile. In contrast, incorporating the impact of molecular migration between interfaces yields good agreement with experiments. **(b)** Experimental snapshots overlaid with simulation profiles (blue lines), shown with (right) and without (left) molecular migration. A schematic illustrates the mechanism. **(c)** Comparison of cleaning effectiveness between capillary lifting and traditional soaking for real-world soil droplets. All scale bars represent 3 mm.

To answer this discrepancy, we need to consider molecular migration across the ternary system. When a droplet forms a capillary bridge between the droplet–solid

and the droplet–air interface, the simultaneous increase in liquid-droplet interfacial area and exposure to the hydrophobic air phase can stimulate amphiphile redistribution within a composite solution, here the formulation. This results in different molecular concentrations at the different interfaces. For example, it has been shown that oil vapour in the air phase can promote surfactant adsorption at water–air interfaces through cooperative interactions with oil molecules that thermodynamically stabilise the adsorption layers. [25] Here, the mechanisms and dynamics of surfactant migration are not known a priori. We start from the so-called Hansen solubility parameters [26] which can quantify the cohesive energy of a substance and help predict its solubility in another material. Here, we use it to assess the likelihood of glycol ether migration across the oil–water interface. The interaction distance $R_{a(A-B)}$ between two molecules A and B in Hansen space is given by Eq. 5.2: [26]

$$R_{a(A-B)} = \sqrt{4(\delta_{d,A} - \delta_{d,B})^2 + (\delta_{p,A} - \delta_{p,B})^2 + (\delta_{h,A} - \delta_{h,B})^2} \tag{5.2}$$

where δ_d, δ_p, and δ_h correspond to the dispersion, polar, and hydrogen bonding contributions to the cohesive energy density, respectively.

Table 5.4: Hansen solubility parameters (HSP).

Compound	**HSP ($[J/cm^3]^{1/2}$)**		
	δ_d	δ_p	δ_h
Diethylene glycol monoethyl ether (Carbitol™)	16.1[a]	9.2[a]	12.2[a]
Tripropylene glycol methyl ether (DOWANOL™ TPM)	15.1[b]	3.5[b]	11.5[b]
Ethylene glycol monohexyl ether (Hexyl CELLOSOLVE™)	16.2[c]	9[c]	5.5[c]
Decane	15.7[d]	0[d]	0[d]
Tetradecane	16.2[d]	0[d]	0[d]
Water	15.5[d]	16[d]	42.3[d]

[a] From Dow database, Technical Data Sheet, `https://www.dow.com/en-us/document-viewer.html?docPath=/content/dam/dcc/documents/110/110-00978-01-carbitol-solvent-tds.pdf`

[b] From Dow database, Technical Data Sheet, `https://www.dow.com/en-us/document-viewer.html?docPath=/content/dam/dcc/documents/110/110-00619-01-dowanol-tpm-tds.pdf`

[c] From Dow database, Technical Data Sheet, `https://www.dow.com/en-us/document-viewer.html?docPath=/content/dam/dcc/documents/110/110-00971-01-hexyl-cellosolve-solvent-tds.pdf`

[d] Taken from [27].

The calculated Hansen solubility parameters are listed in Table 5.4. The Hansen distance $R_{a(A-B)}$ between the glycol ethers and the oil phase (decane or tetradecane) ranges from 10.5 to 15.3 $(J/cm^3)^{1/2}$, with an average of 12.66 $(J/cm^3)^{1/2}$. In contrast, the distance to water is substantially larger, between 30.9 and 34.9 $(J/cm^3)^{1/2}$, averaging 33.03 $(J/cm^3)^{1/2}$. This approximately 2.6-fold lower Hansen distance to the oil phase indicates a much greater solubility of the glycol ethers in oil, suggesting that these molecules preferentially migrate toward the soil droplet and consequently modify the interfacial tensions in the ternary system. The influence of this migration on interfacial tension balance can be quantified with the Neumann triangle method [28], by depositing an oil droplet on the liquid-air interface to mimic ternary dewetting conditions (Fig. 5.3b). The results demonstrate a shift in the interfacial tensions from $\gamma_{dg}/\gamma_{lg} = 0.94$ and $\gamma_{dl}/\gamma_{lg} = 0.64$ in the binary system, to $\gamma_{dg}/\gamma_{lg} = 0.84$ and $\gamma_{dl}/\gamma_{lg} = 0.24$ in the ternary system where liquids are exposed to air. This change confirms the importance of glycol ether migration despite their relatively low concentration (1.35 wt%). Incorporating the corrected interfacial tensions into our model, with a receding contact angle $\theta_{dl} = 26.9°$, yields a good agreement between experimental and computational results (see panels 1 and 3 in Fig. 5.10a, and Fig. 5.10b).

Having demonstrated that our framework captures the dewetting behaviour in both pure liquids and formulations, we aim to move towards real-world cleaning situations through the capillary lifting mechanism. We do this by comparing the dewetting of common soils by capillary lifting and using the traditional soaking method with and without added detergent. For soils, we use olive oil (food residues), squalane (pharmaceutical, personal care and lubricants) and used engine oil (industrial soils with combustion residues). For the solid we use PMMA, a common, medium surface energy substrate, and pure water as the working liquid. For all soils, we can observe removal by capillary lifting, with dewetting efficiencies of $79 \pm 5\%$ for olive oil, $91 \pm 5\%$ for squalane, and $33 \pm 3\%$ for used engine oil. In contrast, when these soils are deposited on substrates in a water bath to simulate traditional soaking, they remain permanently adhered to the substrate (Fig. 5.10c), despite some changes in the contact angles. This contrast highlights the central role of

the capillary bridge and the rising liquid–air interface interacting with the droplet in the removal mechanism. A simple scaling estimate further shows that capillary forces dominate over buoyancy for the droplet sizes studied. The capillary force scales as $F_{\mathrm{cap}} \sim 2\pi\gamma L_{\mathrm{ref}}$, while buoyancy scales as $F_{\mathrm{buoy}} \sim \Delta\rho g V$. For a squalane–water system, using $\gamma = 45.1\ \mathrm{mN\,m^{-1}}$, $L_{\mathrm{ref}} = V^{1/3} \approx 2.15$ mm, $\Delta\rho = 190\ \mathrm{kg\,m^{-3}}$, and droplet volume $V = 10\ \mu$L, yielding capillary force $F_{\mathrm{cap}} \sim 6.1 \times 10^{-4}$ N and buoyancy $F_{\mathrm{buoy}} \sim 1.9 \times 10^{-5}$ N. Thus, capillary forces exceed buoyancy by more than one order of magnitude in this representative case, confirming that droplet removal is primarily capillarity dominated, with buoyancy acting as a secondary assisting contribution once the droplet is immersed. This also justifies the inclusion of gravity in the simulation models, where it acts to assist but not drive removal. Furthermore, the soaking experiments demonstrate that buoyancy alone is insufficient to overcome droplet adhesion to the substrate, directly confirming that both a free liquid–air interface and the formation of a capillary bridge are essential to the removal mechanism.

The soaking experiment (Fig. 5.10c) used pure water as the working fluid, while in real-world applications detergents are often added to enhance cleaning. To assess this, 0.1 mL of a 50 wt% Fairy washing-up liquid solution was added to a 10 mL water bath containing a 10 μL olive oil droplet. The detergent took approximately 40 minutes to reach the droplet and a further 10 minutes to remove it, typically in two or more stages, which is much slower than the capillary lifting process (Fig. 5.11).

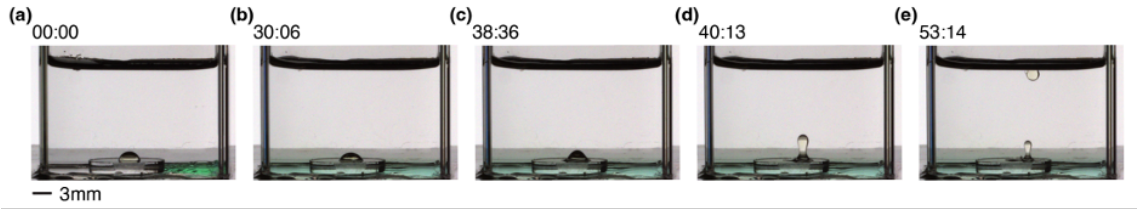

Figure 5.11: Droplet removal by soaking with a solution containing detergent. **(a)** A 0.1 mL solution of 50 w/w% Fairy in water is added to a 10 mL water bath containing a 10 µL olive oil droplet deposited on a PMMA substrate at the bottom. **(b)** Within the first 30 minutes, the washing-up liquid diffuses around the bottom of the container, lowering the water-droplet interfacial tension and causing the droplet to spread. **(c)** Then, the washing-up liquid deforms the upper curvature of the droplet, initiating detachment from the central top. This process continues until a significant portion of the droplet is lifted and detached, as shown in **(d)**. After some time, the effect repeats, detaching a second portion of the droplet **(e)**. Timestamps are shown in mm:ss.

5.5 Conclusion

In summary, we investigated capillary lifting mechanism for droplet dewetting in ternary system using a combination of experiments and computational modelling. Our results show that dewetting is favoured when $\theta_{dl} > \theta_t$. This corresponds to increasing θ_{dl} and hence decreasing γ_{dg}/γ_{lg}, offering an alternative to the use of surfactants to decrease the interfacial tension of the working liquid. For formulated fluids that often contain polymers and surfactants, we also show that molecular migration can significantly change the droplet dewetting outcome. Finally, we demonstrate the ability of capillary lifting to achieve significantly higher cleaning efficiency than soaking for real-world soils. This study advances the understanding of ternary dewetting mechanisms and highlights the potential of capillary lifting as an effective cleaning mechanism for situations with minimal energy and material input. Future studies will investigate the exploitation of related capillary-based phenomena to displace materials from solid surfaces, including solids, films, gels, and other viscoelastic materials.

References

[1]Q. Chen, T. Wang, L. Tang, Z. Zeng, and B. Zhu, "Study on the structure-activity relationship between oil dewetting self-cleaning and surface morphology for crude oil pollution treatment and crude oil/water separation", Journal of Environmental Chemical Engineering **11**, 109092 (2023).

[2]I. Torun, C. Huang, N. B. Kiremitler, M. Kalay, M. Shim, and M. S. Onses, "Coffee-ring mediated thinning and thickness-dependent dewetting modes in printed polymer droplets coupled with assembly of quantum dots for anti-counterfeiting", Small **20**, 2405429 (2024).

[3]X. Zhou, Y. Cai, M. Xu, J. Li, C. Sheng, Q. Zhang, X. Qiu, W. Wang, S. Xiong, C. Cong, Z.-J. Qiu, R. Liu, and L. Hu, "Dewetting-assisted patterning of organic semiconductors for micro-OLED arrays with a pixel size of 1 µm", Small Methods **6**, 2101509 (2022).

[4]Z. Golany, I. Weisbord, M. Abo-Jabal, O. Manor, and T. Segal-Peretz, "Polymer dewetting in solvent-non-solvent environment- new insights on dynamics and lithography-free patterning", Journal of Colloid and Interface Science **596**, 267–277 (2021).

[5]D. Liu, H. Yin, Z. Wu, and X. Luo, "Retraction dynamics of an impacting droplet on a rotating surface", Physical Review Fluids **10**, 033602 (2025).

[6]B. Bhatt, S. Gupta, V. Sumathi, S. Chandran, and K. Khare, "Electric field driven reversible spinodal dewetting of thin liquid films on slippery surfaces", Advanced Materials Interfaces **10**, 2202063 (2023).

[7]F. Wang, L. Chen, Y. Li, P. Huo, X. Gu, M. Hu, and D. Deng, "Self-lifting droplet driven by the solidification-induced solutal marangoni flow", Physical Review Letters **132**, 014002 (2024).

[8]S. Goel, R. Gowda BT, and D. S. Pillai, "Electric field-dependent scaling law for overdamped (di)electrowetting and dewetting on dielectric", Physical Review Fluids **10**, 014201 (2025).

[9]A. F. Demirörs, S. Aykut, S. Ganzeboom, Y. A. Meier, and E. Poloni, "Programmable droplet manipulation and wetting with soft magnetic carpets", Proceedings of the National Academy of Sciences **118**, e2111291118 (2021).

[10]Z.-H. Wang, B.-W. Sun, P. Guo, S.-S. Wang, H. Liu, Y. Liu, D.-Y. Zhou, and B. Zhou, "Investigation of flue gas water-alternating gas (flue gas-WAG) injection for enhanced oil recovery and multicomponent flue gas storage in the post-waterflooding reservoir", Petroleum Science **18**, 870–882 (2021).

[11]G. Zhang, R. L. McMullen, and L. Kulcsar, "Investigation of hair dye deposition, hair color loss, and hair damage during multiple oxidative dyeing and shampooing cycles", Journal of Cosmetic Science **67**, 1–11 (2016).

[12]C. Stubenrauch and W. Drenckhan, "Cleaning solid surfaces with liquid interfaces and foams: from theory to applications", Current Opinion in Colloid & Interface Science **72**, 101818 (2024).

[13]L. Wu, Z. Guo, and W. Liu, "Surface behaviors of droplet manipulation in microfluidics devices", Advances in Colloid and Interface Science **308**, 102770 (2022).

[14]K. He, H. Duan, G. Y. Chen, X. Liu, W. Yang, and D. Wang, "Cleaning of oil fouling with water enabled by zwitterionic polyelectrolyte coatings: overcoming the imperative challenge of oil–water separation membranes", ACS Nano **9**, 9188–9198 (2015).

[15]B. Tomšič, L. Ofentavšek, and R. Fink, "Toward sustainable household laundry. washing quality vs. environmental impacts", International Journal of Environmental Health Research **34**, 1011–1022 (2024).

[16]K. J. Pant, P. D. Cotter, M. G. Wilkinson, and J. J. Sheehan, "Towards sustainable cleaning-in-place (CIP) in dairy processing: exploring enzyme-based approaches to cleaning in the cheese industry", Comprehensive Reviews in Food Science and Food Safety **22**, 3602–3619 (2023).

[17]D. Zhang, C. Liu, K. Yu, C. Yan, Y. Shen, Z. An, and J. Jing, "Droplet cleaning method and water consumption analysis for superhydrophobic solar photovoltaic glass", Solar Energy **235**, 94–104 (2022).

[18]C. He, Z. Liu, J. Wu, X. Pan, Z. Fang, J. Li, and B. A. Bryan, "Future global urban water scarcity and potential solutions", Nature Communications **12**, 4667 (2021).

[19]S. O. Badmus, H. K. Amusa, T. A. Oyehan, and T. A. Saleh, "Environmental risks and toxicity of surfactants: overview of analysis, assessment, and remediation techniques", Environmental Science and Pollution Research **28**, 62085–62104 (2021).

[20]J. Arora, A. Ranjan, A. Chauhan, R. Biswas, V. D. Rajput, S. Sushkova, S. Mandzhieva, T. Minkina, and T. Jindal, "Surfactant pollution, an emerging threat to ecosystem: approaches for effective bacterial degradation", Journal of Applied Microbiology **133**, 1229–1244 (2022).

[21]K. A. Brakke, "The surface evolver", Experimental Mathematics **1**, 141–165 (1992).

[22]A. F. Stalder, T. Melchior, M. Müller, D. Sage, T. Blu, and M. Unser, "Low-bond axisymmetric drop shape analysis for surface tension and contact angle measurements of sessile drops", Colloids and Surfaces A: Physicochemical and Engineering Aspects **364**, 72–81 (2010).

[23]E. J. De Souza, M. Brinkmann, C. Mohrdieck, A. Crosby, and E. Arzt, "Capillary forces between chemically different substrates", Langmuir **24**, 10161–10168 (2008).

[24]Y. Wang, S. Michielsen, and H. J. Lee, "Symmetric and asymmetric capillary bridges between a rough surface and a parallel surface", Langmuir **29**, 11028–11037 (2013).

[25]V. B. Fainerman, E. V. Aksenenko, V. I. Kovalchuk, N. Mucic, A. Javadi, L. Liggieri, F. Ravera, G. Loglio, A. V. Makievski, E. Schneck, and R. Miller, "New view of the adsorption of surfactants at water/alkane interfaces – competitive and cooperative effects of surfactant and alkane molecules", Advances in Colloid and Interface Science **279**, 102143 (2020).

[26]C. M. Hansen, "The three dimensional solubility parameter and solvent diffusion coefficient and their importance in surface coating formulation.", Ph.D. thesis, Copenhagen: Danish Technical Press (1967).

[27]M. Murase and D. Nakamura, "Hansen solubility parameters for directly dealing with surface and interfacial phenomena", Langmuir **39**, 10475–10484 (2023).

[28]A. Nikolov and D. Wasan, "Oil lenses on the air–water surface and the validity of neumann's rule", Advances in Colloid and Interface Science, Special Issue in Honor of the 90th Birthday of Prof. Eli Ruckenstein **244**, 174–183 (2017).

Chapter 6

General discussion and outlook

6.1 General discussion

This thesis explored interfacial capillarity through three interconnected phenomena: adhesion, bridging, and capillary-driven removal. Collectively, these investigations provide a framework for understanding how capillary forces arise and interact across diverse systems and length scales, from the nanometre to the millimetre. By integrating experiments with modelling within the quasi-static hydrodynamic regime, the work elucidates how geometry, wettability, and interfacial tension collectively govern interfacial mechanical balance, shaping liquid morphology and motion. Building upon these fundamental insights, new approaches were developed that harness the subtle yet powerful nature of capillary interactions to achieve efficient and sustainable manipulation of liquids.

Common Formulation and Validity. In this thesis, the governing physics reduces to a common formulation in which the total interfacial energy $E = \sum_i \gamma_i A_i$ is minimised with respect to a single evolving state variable: the withdrawal displacement (Chapter 3), the plate separation (Chapter 4), or the working liquid volume (Chapter 5). Capillary forces follow from this thermodynamic formulation, arising from contributions of surface tension and Laplace pressure.

The minimal inputs are interfacial tensions, contact angles (via Young's equation), and system geometry; the outputs are capillary forces, interface shapes, pressure, and detachment or dewetting thresholds. What changes across chapters is the length scale, the number and nature of phases involved (solid or fluid) and the geometry and wettability; what remains invariant is the energy minimisation framework, the Laplace pressure relation, and the capillary force construction. This formulation is valid under quasi-static evolution with well-defined contact lines between phases, and breaks down under dynamic conditions or surface imperfections that cannot be

fully controlled or characterised. The mapping of each chapter onto this common formulation is summarised in Table 6.1, with typical examples of breakdown mechanisms given for each case. Across all systems, detachment or dewetting occurs when the capillary force can no longer be sustained by the available interfacial curvature under the imposed geometric and wetting constraints, causing contact lines to recede or interfaces to rupture.

Table 6.1: Mapping of each chapter onto the common capillary formulation.

	State variable	**Control parameters**	**Output**	**Breaks example**
Ch. 3	Tip displacement	θ, cone angle, line tension	Detachment force	High withdrawal velocity, surface imperfection
Ch. 4	Plate separation	θ, surface type	Capillary force, bridge geometry	Large oil ridge, viscous dissipation
Ch. 5	Working liquid volume	γ_{ij}, θ_{dl}, θ_t	Dewetting threshold, morphology	Viscoelasticity, kinetic molecular migration

Quantitative outputs. The key quantitative outputs from each chapter are summarised here. In Chapter 3, line tension effects become significant when the particle characteristic length falls below $\sim \tau/\gamma$ (where τ is the line tension and γ the interfacial tension, typically $\tau/\gamma \sim 5$ nm in the systems tested), below which deviations from classical capillary adhesion emerge; the dominant sensitivity arises from particle geometry (cone angle). In Chapter 4, capillary forces on liquid-infused surfaces are 5–10 times lower than on solid substrates ($\sim$0.15 mN vs 0.7–2.2 mN), placing the bridge in a gravity-sensitive regime where $\rho g V \sim F_{\text{cap}}$; cloaking by the lubricant reduces the effective surface tension by $\sim$25% and alters bridge geometry through lubricant transfer. In Chapter 5, for ternary systems where a three-phase contact line exists, dewetting is favoured when $\cos\theta_{dl} < \cos\theta_t$, with regime boundaries governed primarily by the interfacial tension ratios and contact angles, validated across multiple fluid pairs and surface combinations.

Scope and limitations. The common formulation presented here is valid under quasi-static conditions, chemically homogeneous surfaces, and idealised geometries that can be faithfully represented in simulation. In practical terms, this requires low capillary number ($Ca \ll 1$) and well-defined contact lines between phases. Breakdown occurs when these conditions are violated. These limitations manifest differently across the systems studied; as examples: nanoparticle adhesion (Chapter 3) deviates when surface imperfections such as nanoscale pinning are present and cannot be characterised experimentally, or under dynamic withdrawal at high velocity; capillary bridges on liquid-infused surfaces (Chapter 4) can be affected by lubricant redistribution and viscous dissipation at the oil ridge; capillary lifting (Chapter 5) breaks down when interfacial tensions become composition-dependent due to mass transfer between fluid phases, or when the working liquid is injected rapidly and unevenly. Experimentally, these breakdowns are identified through rate-dependent force–displacement behaviour, variability in apparent contact angles and effective interfacial tension, and the emergence of asymmetric or evolving interface morphologies.

Chapter 3 examined the adhesion of nanoparticles at fluid interfaces. Using atomic force microscopy and numerical modelling, we investigated how tip geometry, surface wettability, and fluid combinations govern the adhesion profile during particle detachment from liquid interfaces. Conical nanoparticles with varying cone angles were used to quantify force–distance behaviour as the tip withdrew from oil–air and oil–water interfaces. While both geometry and wettability influenced the force profile, geometry proved dominant: wide conical tips generated more gradual force transitions and higher detachment barriers. Modelling revealed that this behaviour originates from differences in meniscus dimensions and curvature. By systematically varying contact angle, we observed a transition between monotonic and non-monotonic force behaviour, reflecting changes in how the interface wets the particle, which is an insight directly relevant to stabilisation mechanisms in Pickering emulsions. The computational model accurately reproduced experimental trends and captured the delicate nanoscale capillary interactions. These results confirm that classical thermodynamic principles of capillary adhesion remain valid

at the nanoscale and identify the threshold where line tension and molecular effects emerge. The framework developed here provides a powerful yet accessible tool for understanding nanoscale adhesion and designing particles with tunable attachment and release properties.

The study then advanced from adhesion at single interfaces to bridging between two surfaces, exploring how liquid menisci transmit forces across solid boundaries. Capillary bridges play a central role in many natural and industrial processes, from wet granular cohesion and pigment formulation to lubrication and liquid transport. Their mechanics are highly sensitive to surface chemistry, roughness, and geometry. With the advent of superhydrophobic materials such as liquid-infused surfaces, designed for frictionless and omniphobic behaviour, understanding bridge formation and stability on these surfaces has become essential for controlling liquid motion.

In Chapter 4, capillary bridges formed between hydrophilic, hydrophobic, and liquid-infused surfaces (LIS) were systematically examined under controlled stretching and compression. On hydrophilic glass, contact line pinning dominated, producing the characteristic stick–slip behaviour as the contact lines moved. On hydrophobic surfaces prepared by silanisation, bridge compression-stretching followed the classical advancing and receding behaviour, reflecting energy dissipation through hysteresis. In contrast, on LIS, the contact line moved smoothly and reversibly, demonstrating nearly frictionless motion. Despite these differences, all systems could be consistently described within the same theoretical framework based on surface tension and Laplace pressure, provided that appropriate apparent contact angles were used for the liquid-infused case. Bridges on LIS exhibited a small but measurable geometric asymmetry due to gravity, suggesting that the reduced capillary forces in these systems allow hydrostatic effects to become significant. Additional experiments using asymmetric configurations between hydrophobic solid surfaces and liquid-infused surfaces revealed lubricant transfer from the lubricated to the solid side, confirming that the lubricant introduces an additional dynamic pathway for interfacial evolution. These findings demonstrate how surface chemistry governs bridge mechanics and provide quantitative benchmarks for capillary interactions on modern functional surfaces.

Building on this understanding, the final Chapter 5 of this thesis explored how capillarity can be harnessed not to bind, but to detach. A capillary lifting mechanism was developed to remove droplets from solid surfaces efficiently by exploiting interfacial forces rather than chemical additives or external energy. This approach relies on high interfacial tension to drive liquid motion, eliminating the need for surfactants or high-energy input. Upon contact, the working liquid forms a capillary bridge between the deposited droplet–substrate interface and the droplet–air interface. As additional liquid is introduced, the upper interface rises, causing the bridge to deform and eventually rupture, thereby lifting the droplet through the controlled evolution of interfacial curvature. A theoretical framework based on apparent and receding contact angles was established to predict detachment conditions, supported by experiments and simulations that systematically mapped the governing parameter space. The results show that dewetting and removal behaviours can be accurately described by interfacial properties under quasi-static conditions. This study provides a physical foundation for a new class of cleaning and dewetting strategies that utilise capillary forces for efficient, energy-saving, and environmentally sustainable surface maintenance.

In summary, these studies present a coherent understanding of capillary interactions at interfaces. By linking adhesion, bridge mechanics, and droplet removal, they reveal how the fundamental principles of thermodynamic capillarity govern behaviour across diverse systems and length scales. The integration of experiments, modelling, and theory provides both conceptual and practical insights: conceptually, it elucidates how interfacial geometry and chemistry affect the adhesion strength, the direction and magnitude of capillary forces, and the evolution of liquid morphology; practically, it establishes design principles for tuning adhesion, directing liquid transport, and achieving passive cleaning without chemical additives. Ultimately, this thesis demonstrates that capillarity, though subtle and often hidden from macroscopic view, governs powerful interactions that connect the nanoscale to the macroscopic world. By combining precise experiments with theoretical and computational tools, it shows how the same physical principles that stabilise particles or sustain liquid bridges can, when carefully controlled, be harnessed to remove

contaminants and enable sustainable cleaning. In this way, capillarity emerges not merely as a classical topic of surface science but as a modern and versatile tool for developing efficient, adaptive, and environmentally responsible technologies. Building on this foundation, this thesis opens pathways for future studies that explore more complex physical interactions in multiphase systems and connect molecular interactions to microscale wetting behaviour and macroscopic interfacial function. The following outlook projects build upon these findings to address open questions and new directions arising from this thesis.

6.2 Outlook

6.2.1 Asymmetric particles at interfaces

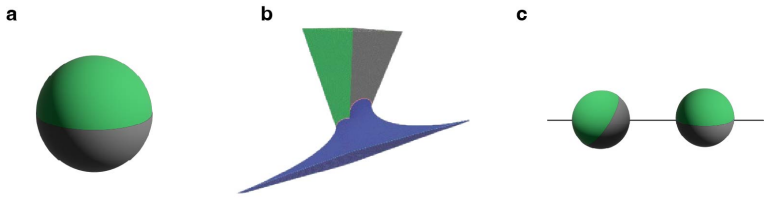

Figure 6.1: **(a)** A spherical Janus particle with different surface chemistries shown in green and grey. **(b)** Simulation of a chemically asymmetric pyramid-shaped particle at a fluid interface (blue). **(c)** Simple sketch of two Janus particles at an interface, representing a dynamic process where one particle is not yet fully stabilised in its orientation.

Modern colloidal physics has predominantly focused on particles with symmetric geometry and uniform surface chemistry, whereas biological systems routinely involve solid or viscoelastic particles that are intrinsically asymmetric in both shape and composition.[1] With the rapid development of functional materials, increasing attention has turned towards asymmetric particles for their unique adhesion, wetting behaviour, and assembly properties.[2–4] Such particles can generate complex structures and emergent functions unattainable with homogeneous or symmetric systems. For example, Janus particles (Fig. 6.1a), possessing two faces of different chemistry or wettability, can direct their orientation and assembly at interfaces, offering new routes for controlled colloidal organisation and responsive materials.[1]

While asymmetric geometry and chemistry provide many promising functionali-

ties, they also introduce new challenges. It remains difficult to dynamically control their stability, interfacial configuration, and preferred orientation, whether they are strongly bound through specific physical or chemical interactions or mobile within the surrounding flow. At the nanoscale, experimental work becomes particularly challenging because of the delicate nature of the systems and the deviations that can arise during fabrication, placement, and characterisation.

The framework established in Chapter 3 of this thesis provides a foundation for addressing these challenges. By inputting relevant physical and chemical properties, we can predict adhesion profiles at specific liquid interfaces. Through numerical modelling, we visualise and analyse meniscus formation and energy, offering direct insight into interfacial energy landscapes at the nanoscale. This approach can be readily extended to Janus particles, where geometry, interfacial chemistry, and wettability can be tuned within the same computational framework towards targeted systems, providing optimised strategies for future smart nanoparticle design (Fig. 6.1b).

The current model can also be expanded to include additional interactions such as line tension, particle–particle coupling (Fig. 6.1c), and viscoelastic interfacial responses through additional energetic terms. Looking ahead, this framework could be coupled with dynamic modelling methods such as computational fluid dynamics to explore how designed asymmetric particles move and interact within flowing fluidic environments. In doing so, the model will serve as a predictive and adaptable tool for material design, connecting nanoscale particles to macroscopic functions and guiding the development of intelligent and responsive interfacial systems.

6.2.2 Probing molecular migration at interfaces using electrochemistry

Adding chemical agents to multiphase fluid systems is common in cleaning, chemical reactions, and manufacturing processes. For instance, in Chapter 5, a low-concentration ether formulation was used as the working liquid to lift droplets from solid surfaces. The migration of molecules such as surfactants or electrolytes is well known to alter interfacial tension, yet quantitative studies remain scarce due to the

complexity of the coupled chemical and physical effects across multiple length scales. From the nano- to microscale, these systems are extremely delicate and sensitive, making direct measurements difficult. Nevertheless, understanding molecular redistribution at these scales is crucial for explaining interfacial properties and dynamic behaviour in many functional and biological systems.

To explore molecular migration and redistribution in multiphase systems at these scales, we propose the use of scanning electrochemical cell microscopy (SECCM).[5] SECCM operates similarly to atomic force microscopy in that it controls the approach and retraction of a probe toward a substrate using feedback signals. The "cell" in SECCM is a microcapillary with an open end typically ranging from 3 to 30 μm in diameter. This cell is filled with liquid (usually an aqueous solution) and brought toward a substrate. Upon contact, a microscale capillary bridge forms between the open end of the cell and the substrate. The approach is regulated by an electrical feedback signal that defines the moment of contact. The probe can then be held in position or withdrawn immediately, while electrochemical signals are recorded throughout the process as the capillary bridge elongates and eventually ruptures.

Coupling SECCM with in situ optical microscopy is a recent advance that allows direct visualisation of the capillary bridge from below the substrate, opening new possibilities for studying microscale interfacial phenomena. The small bridge size gives access to regimes where the surface-to-volume ratio amplifies molecular effects that would otherwise be negligible in macroscopic measurements. We propose to use this microscale capillary configuration to probe electrical signals that may reveal molecular transfer between the liquid in the cell and the surrounding phase, while simultaneous imaging visualises how wetting behaviour and interface shape evolve in real time.

Experimental design begins with a simple reference system in which the SECCM cell, filled with ultrapure water, approaches a clean substrate in air (Fig. 6.2a). The setup can then be extended to oil-immersed systems, introducing a liquid–liquid interface between water and oil [6]. Here we show preliminary experimental data for such a system in Fig. 6.2c. Future studies will involve adding surfactants or

electrolytes to the aqueous phase to examine how molecular migration influences both the electrochemical response and the capillary morphology during approach and retraction (Fig. 6.2b).

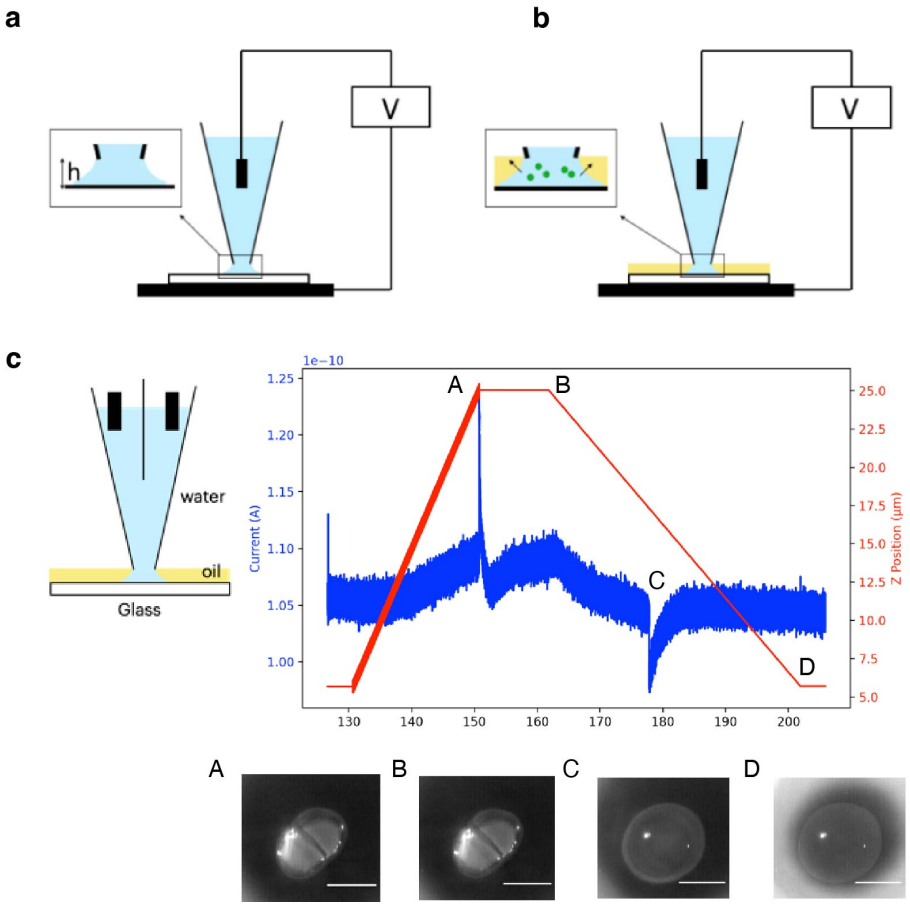

Figure 6.2: **(a–b)** Schematic experimental design using a single-cell scanning electrochemical cell microscopy (SECCM) setup. The electrical signal is measured between the substrate and the electrode (shown as a black rectangle) in the conical cell. The experiment begins with a reference water-air system (a) and can be extended to investigate molecular migration across interfaces when the substrate is immersed in oil and chemical species are added to the liquid in the cell (b). **(c)** Example data for a water–oil system. Note that a double-channel SECCM cell was employed here to optimise signal detection, but the principle remains the same. The plot shows the probe position and corresponding electrochemical response over time. Optical images (A–D) provide a bottom-view sequence of the substrate as the cell approaches and retracts: (A) initial contact, (B) holding at constant height, (C) bridge rupture accompanied by a signal spike, and (D) the cell returning to its original height with residue droplets left on the substrate. Scale bars represent 10 μm.

This approach connects microscale molecular transfer with macroscopic interfacial behaviour, linking local chemical processes to global capillary effects. It enables quantitative investigation of how molecular redistribution modifies interfacial energy

and adhesion at confined scales. In practical terms, SECCM provides a platform for spatial mapping of surface chemistry and chemical activity, offering new insights into how minimal molecular modifications can tune interfacial properties. Such understanding is particularly valuable for microfluidic systems, biological interfaces, and responsive materials, where precise control of wettability and surface chemistry in confined environments is essential for designing efficient and adaptive interfacial phenomena.

6.2.3 Particle-laden droplet removal

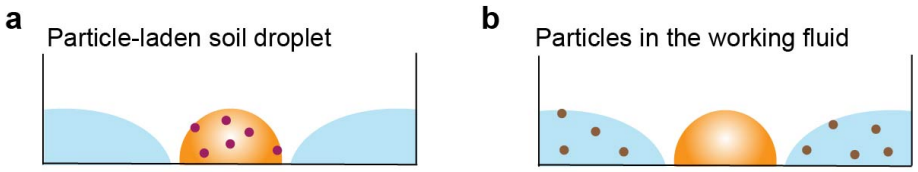

Figure 6.3: **(a)** Capillary lifting applied to remove particle-laden soil droplets. **(b)** Cleaning soil droplets using a particle suspension as the working liquid ("dirty" working liquid).

Chapter 5 demonstrated how capillary interactions can be harnessed to remove droplets effectively with minimal use of energy and materials. The unwanted droplets studied ranged from pure alkanes to complex real-world contaminants such as olive oil, squalane, and used engine oil. However, practical cleaning scenarios are even more complex. Soils and residues often contain solid or viscoelastic particles (*e.g.*, food residues, dust, and mineral deposits) that introduce additional interfacial, rheological, and adhesive complexities. The next step is to extend capillary-driven cleaning towards particle-laden systems, where either the droplet or the working liquid contains suspended particles, which is a common feature in practical environments. This direction aims to translate the fundamental findings from model systems to real-world applications by developing and testing capillary cleaning prototypes under more complex, heterogeneous conditions.

Particles adsorb strongly at interfaces while being transported by fluid flows, introducing dynamics that differ markedly from those of pure liquids. Several critical questions therefore arise when considering particle-laden cleaning systems: if

the soil to be removed is a composite droplet containing solid particles, can the capillary lifting mechanism still detach it effectively? Alternatively, when particles are suspended in the working liquid, as in recycled or contaminated water, can capillary forces drive them toward interfaces and assist in soil removal? In both scenarios, particles may hinder cleaning by increasing viscous resistance and interfacial adhesion, yet they may also promote detachment by stabilising transient fluid interfaces through Pickering-type effects [7]. The overall behaviour depends sensitively on system geometry, fluid properties, and interfacial dynamics. Understanding these competing mechanisms is essential for translating capillary-driven cleaning into practical applications.

The first stage of this work can focus on capillary lifting of particle-laden composite droplets that represent realistic contaminants (Fig. 6.3a). Particles can be synthesised with controlled surface chemistry and geometry, or drawn from natural sources such as dust or sand to capture real-world variability. Using integrated experiments and simulations [8], we would be able to quantify how particle properties (*e.g.*, wettability, size, and shape) affect interfacial dynamics and adhesion. This will involve characterising particle partitioning between bulk fluids and interfaces, evaluating capillary-driven particle transport during droplet removal, and establishing predictive relationships between particle attributes and overall cleaning efficiency. Building on this foundation, the study will then explore particle-laden working liquids as sustainable cleaning media (Fig. 6.3b). This modern approach uses recycled or contaminated liquids as the working phase, aiming to reduce fresh water use without sacrificing performance. We will investigate how particles suspended in the working liquid influence capillary lifting, focusing on how particle concentration and interfacial activity modify bridge formation, rupture, and droplet detachment. Additional questions include whether particles adhere to the substrate during cleaning and how this affects surface recontamination. Together, these studies will establish the fundamental design rules for sustainable, capillarity-based cleaning systems that maintain high efficiency while drastically reducing water and chemical consumption.

References

[1]A. Walther and A. H. E. Müller, "Janus particles: synthesis, self-assembly, physical properties, and applications", Chemical Reviews **113**, 5194–5261 (2013).

[2]T. Zhang, D. Lyu, W. Xu, X. Feng, R. Ni, and Y. Wang, "Janus particles with tunable patch symmetry and their assembly into chiral colloidal clusters", Nature Communications **14**, 8494 (2023).

[3]A. McGlasson, E. Morgenthaler, L. C. Bradley, and T. P. Russell, "On the interfacial assembly of anisotropic amphiphilic janus particles", Advanced Functional Materials **34**, 2306651 (2024).

[4]Q. He, H. Vijayamohanan, J. Li, and T. M. Swager, "Multifunctional photonic janus particles", Journal of the American Chemical Society **144**, 5661–5667 (2022).

[5]S. Amemiya, A. J. Bard, F.-R. F. Fan, M. V. Mirkin, and P. R. Unwin, "Scanning electrochemical microscopy", Annual Review of Analytical Chemistry **1**, 95–131 (2008).

[6]Y. Li, A. Morel, D. Gallant, and J. Mauzeroll, "Oil-immersed scanning micropipette contact method enabling long-term corrosion mapping", Analytical Chemistry **92**, 12415–12422 (2020).

[7]B. P. Binks, "Particles as surfactants—similarities and differences", Current Opinion in Colloid & Interface Science **7**, 21–41 (2002).

[8]A. Naga, X. Zhang, J. Yang, and H. Kusumaatmaja, *Modeling droplet-particle interactions on solid surfaces by coupling the lattice boltzmann and discrete element methods*, May 15, 2025, `https://doi.org/10.48550/arXiv.2505.10171` (visited on 09/02/2025).

Chapter 7

Conclusion

This thesis examined capillary interactions at liquid and solid interfaces across length scales from nanometres to millimetres, focusing on particle adhesion, liquid bridging, and droplet removal. Through an integrated experimental and modelling approach, we demonstrated how geometry, wettability, interfacial properties, and gravity collectively govern capillary forces and liquid morphology in a predictable, scale-dependent manner.

At the nanoscale, particle adhesion at liquid interfaces followed classical thermodynamic principles, with wettability and geometry determining adhesion strength. Line tension emerged as a significant factor below a defined size threshold, establishing quantitative bounds for when nanoscale corrections become necessary. At larger scales, systematic comparisons of capillary bridges between solid and liquid-infused surfaces revealed distinct regimes of contact-line dynamics: from strong pinning and hysteresis on conventional solids to nearly frictionless motion and observable gravity-induced deformation on liquid-infused surfaces. Despite these differences, all systems conformed to a unified thermodynamic framework governed by interfacial tension and Laplace pressure. Building on this foundation, we demonstrated that capillary forces can be harnessed for practical droplet removal. The resulting capillary lifting mechanism enables sustainable detachment of liquids using minimal resources and energy, addressing critical environmental challenges in cleaning technologies.

To conclude, this work establishes capillarity as both a universal physical principle and a versatile engineering tool, bridging nanoscale adhesion and macroscopic function. The insights gained provide not only fundamental advances in interfacial science but also practical pathways toward efficient and sustainable liquid manipulation strategies.